Laser Setup for the ET Phase Camera

Master's Thesis in Physics

Presented by
Timo Neeser
22.10.2024

Erlangen Centre for Astroparticle Physics
Friedrich-Alexander-Universität Erlangen-Nürnberg

Supervisor/Betreuer: Prof. Dr. Stefan Funk

Abstract

The Einstein Telescope (ET) group at ECAP works on building a phase camera that can use 1D and 2D fiber pixel arrays to measure the geometric phase differences between two superimposed laser beams consisting of a carrier signal plus symmetric frequency sidebands, and a reference signal for heterodyne detection. The goal of this master's thesis was to design and construct an optical setup for the phase camera and a framework to allow for the comparison between phase data recorded with the 2D array and expectations according to theory. The finalized laser setup and its limitations and the challenges in designing it will be discussed. The setup achieves the desired functionality and includes an adjustable telescope section through which a broad bandwidth of different laser beam shapes can be created for studying phase configurations. First measurements present a good correlation between simulation and measurements for large laser beams and a poor correlation for small beams, as expected.

Contents

1 Introduction **1**

2 Background and theory **2**
2.1 Gravitational waves . . . 2
2.1.1 Gravitational wave theory . . . 2
2.1.2 Types of gravitational waves . . . 3
2.1.3 Gravitational wave detection . . . 4
2.2 Einstein Telescope . . . 6
2.2.1 Noise sources . . . 7
2.3 2D Phase camera . . . 8
2.4 Geometric optics . . . 9
2.4.1 Gaussian beams . . . 9
2.4.2 2x2 Beam transfer matrix optics . . . 10
2.4.3 3x3 Beam transfer matrix optics . . . 12
2.4.4 Specific beam transfer matrices . . . 13
2.4.5 Geometric considerations . . . 13
2.4.6 Fiber Collimators . . . 17
2.4.7 2D camera coordinate system . . . 18
2.5 Signal demodulation . . . 19

3 Laser Setup **21**
3.1 Technical issues . . . 22
3.1.1 Focal shift of the Faraday isolator . . . 22
3.1.2 Systematic errors of the beam profiler . . . 22
3.1.3 Laser beam quality . . . 24
3.1.4 General statistical errors . . . 24
3.1.5 Inaccuracies in technical specs . . . 25
3.2 Evolution of the laser beam through the optical setup . . . 25
3.2.1 First coordinate system . . . 25
3.2.2 Second coordinate system . . . 27
3.3 Signal detection and processing . . . 34

4 Phase simulations **35**
4.1 Graphical interface . . . 35
4.2 Impacts of beam and camera parameters on phase profiles . . . 35

5 Measurements **40**
5.1 Fundamental measurement aspects . . . 40
5.2 Altering the reference beam . . . 41
5.2.1 Marginal beam difference . . . 41
5.2.2 Smaller and larger reference beam . . . 45
5.2.3 Very large reference beam . . . 48
5.3 Altering the test and reference beam . . . 51
5.3.1 Minimally divergent beams . . . 51
5.3.2 Highly divergent beams . . . 53

6 Conclusion **57**

A Appendix **59**
A.1 Technical stats 59
A.2 Laser power across the optical setup 62
A.3 Erroneous laser setup plots 63
A.4 Graphical interface 69
A.5 Beam trajectory measurements 72

Bibliography **75**

1 Introduction

Astronomy and astrophysics have come a long way over the course of the last centuries. From the first optical telescopes to the expansion of the detectable electromagnetic spectrum ranging from radio [1] to ultra high energy gamma rays [2], to the detection of neutrinos and cosmic rays, our knowledge of the universe has continuously expanded [3]. In 1916, Albert Einstein published his theory of general relativity (GR) and set the stage for the eventual discovery of a fourth astrophysical messenger [4]. It would take almost 100 years until his theory on gravitational waves (GW) would be finally proven correct. On September 14th, 2015 at 09:50:45 UTC, the Laser Interferometer Gravitational-Wave Observatory (LIGO) discovered the first identifiable gravitational wave signature in history through the usage of two gigantic advanced Michelson interferometers located on opposite sides of the United States of America. This was the event GW150914, created by a binary black hole merger [5]. The basis provided by LIGO and other early ground-based GW observatories enabled the conception and design of a next generation of much more sensitive GW observatories that are expected to resolve GW signatures originating from distances so far away that their redshifted signals carry information on the early universe. One of these next gen observatories is the so-called Einstein telescope (ET) [6]. Being based on Michelson interferometers, a GW observatory exploits marginal phase shifts of laser beams created by faint GW signals distorting space-time around them. However, their magnitude is so faint that in order to detect them it requires interferometer arms with lengths of many km that basically act as giant amplifiers of distortable space [4, 5]. This in turn also means that any otherwise negligible noise sources like gravitational gradients created by seismic motion, or quantum noises created by the laser light itself are present in raw signals and must be suppressed to an enormous degree, which requires a precise control of the setup [4]. Therefore, GW observatories incorporate advanced control systems that verify and allow precise settings for optimal resolution of signals [7]. The usage of phase cameras that can demodulate the signal of multiple superimposed laser beams provides a powerful tool for diagnostic purposes [8]. As such they are not only used to simply detect a single main signal, but are also applied in all sorts of control sections. The development of phase cameras is thus of interest for advancing the sensitivity of GW detection apparatuses [4, 6].

The purpose of this thesis is to assists in the development of a new proof of concept phase camera that the ET group at ECAP is working on, by designing and constructing an optical setup that is based on a control loop that is utilized in gravitational wave observatories, and providing detailed characterization through calculations and phase simulations. It will reveal the correlation between theory and measurements for multiple types of different laser beams and how their shapes affect the effectiveness of the first working version of the phase camera in accurately reconstructing laser phase profiles.

The thesis starts with Section 2 delving into the relevant physics regarding gravitational waves, details on ET and the goal of the ET group at ECAP, followed by the extends of geometric optics theory required for this work. Section 3 discusses the optical setup, and the challenges and limitations in its design and construction. In Section 4 the graphical interface for conducting phase simulations is introduces and in Section 5, measurements taken with the first version of the phase camera are compared to simulations. The conclusion follows in Section 6.

2 Background and theory

2.1 Gravitational waves

The detection of gravitational waves (GW) provides a useful addition to multimessenger astronomy and a promising method for acquiring deeper knowledge about the early universe. Not only will the combination of GW detections with electromagnetic, neutrino and cosmic ray observations yield a more detailed picture of various energetic phenomena in general, it also allows for the explorations of events with much higher redshifts than currently possible, and thus to obtain a look much farther back in time. This will allow for the investigation of the properties and evolution of primordial objects, and also provide the basis for the evaluation of cosmological parameters such as the Hubble constant, or the the dark energy equation of state. The next generation GW observatories Einstein Telescope (ET) and Cosmic Explorer (CE) are designed to detect binary neutron star (NS) merger events with redshifts up to $z \sim 5$ for ET, and $z \sim 10$ for CE, which allows for a coverage of the entire epoch at the peak of star formation at $z \sim 2$. In comparison, current generation GW observatories are only expected to be able to resolve events with redshifts up to $z \sim 0.2$. Additionally to NS-NS mergers that have a mass of a few $\mathrm{M}_\odot$, ET and CE are slated to be able to observe mergers of binaries with larger masses, that are typical for mergers involving black holes ($20\,\mathrm{M}_\odot - 100\,\mathrm{M}_\odot$), at redshifts of $z \sim 20$ and higher [9, 6].

2.1.1 Gravitational wave theory

Gravitational waves (GW) are a consequence of Einstein's theory of general relativity (GR). Equation 1 provides a metric that describes the distance between two events in a curved, four dimensional spacetime. The curvature of spacetime is described by a symmetric tensor $g_{\mu\nu}$ with index 0 for time, and indices 1, 2, 3 for each dimension in space [4].

$$ds^2 = g_{\mu\nu} dx^\mu \tag{1}$$

GR postulates that the presence of mass bends the fabric of spacetime. The Einstein tensor $G_{\mu\nu}$ represents the relation between spacetime and matter:

$$G_{\mu\nu} = \frac{8\pi G}{c^4} T_{\mu\nu} = R_{\mu\nu} - \frac{1}{2} R g_{\mu\nu}, \tag{2}$$

with gravitational constant G, vacuum speed of light c, Ricci tensor $R_{\mu\nu}$ and Ricci scalar R, and the stress energy tensor $T_{\mu\nu}$:

$$T_{\mu\nu} = \frac{\partial \Gamma^\lambda_{\mu\lambda}}{\partial x^\nu} + \frac{\partial \Gamma^\lambda_{\mu\nu}}{\partial x^\lambda} + \Gamma^\beta_{\mu\lambda}\Gamma^\lambda_{\nu\beta} - \Gamma^\beta_{\mu\nu}\Gamma^\lambda_{\beta\lambda} \tag{3}$$

with the Christoffel's symbol $\Gamma^\lambda_{\mu\nu}$ that describes the shortest curved distance between two points:

$$\Gamma^\lambda_{\mu\nu} = \frac{1}{2}\left[\frac{\partial g_{\lambda\beta}}{\partial x^\nu} + \frac{\partial g_{\mu\beta}}{\partial x^\mu} - \frac{\partial g_{\mu\nu}}{\partial x^\beta}\right]. \tag{4}$$

In the vacuum case, i.e. in the absence of mass, the stress energy tensor $T_{\mu\nu}$ in Equation 3 and Equation 2 reduces to 0. The same applies to the Ricci tensor $R_{\mu\nu}$. If there is a change in matter distribution, then these tensors change which leads to a perturbation of $g_{\mu\nu}$ by the variation induced spacetime metric $h_{\mu\nu}$:

$$\overline{g}_{\mu\nu} = g_{\mu\nu} + h_{\mu\nu}. \tag{5}$$

In the case of weak fields ($h_{\mu\nu} << 1$), a tensor $\overline{h}_{\mu\nu}$ describing the gravitational field can be formulated:

$$\overline{h}_{\mu\nu} = h_{\mu\nu} - \frac{1}{2}\eta_{\mu\nu}h^{\alpha}_{\alpha}, \tag{6}$$

with a flat metric $\eta_{\mu\nu}$. The gravitational wave equation can then be written as $\Box\overline{h}_{\mu\nu} = 0$ with the D'Alembertian operator $\Box$. The simplest solution to this equation is given by(check the phrasing of this again):

$$\overline{h}_{\mu\nu} = A^{\mu\nu}e^{ik_{\alpha}x^{\alpha}}, \tag{7}$$

where $A^{\mu\nu}$ represents amplitude and polarization of the wave, and k_{α} its direction and frequency. In GW detection, this function is generally what is referred to as strain $h(t)$ [4].

2.1.2 Types of gravitational waves

GW are broadly classified into four different types based on origin. Arguably the most important type of GW and the only signals discovered so far are compact binary inspiral gravitational waves which are created throughout the merger of two objects, most prominently binary neutron stars or black holes. These types of GW increase in amplitude and frequency as both objects spiral closer to each other, followed by a peak at collision, and a ring-down as illustrated in Figure 1 showing the signature of the gravitational wave event GW150914 with a peak strain of $h \approx 10^{-21}$ [4, 5].

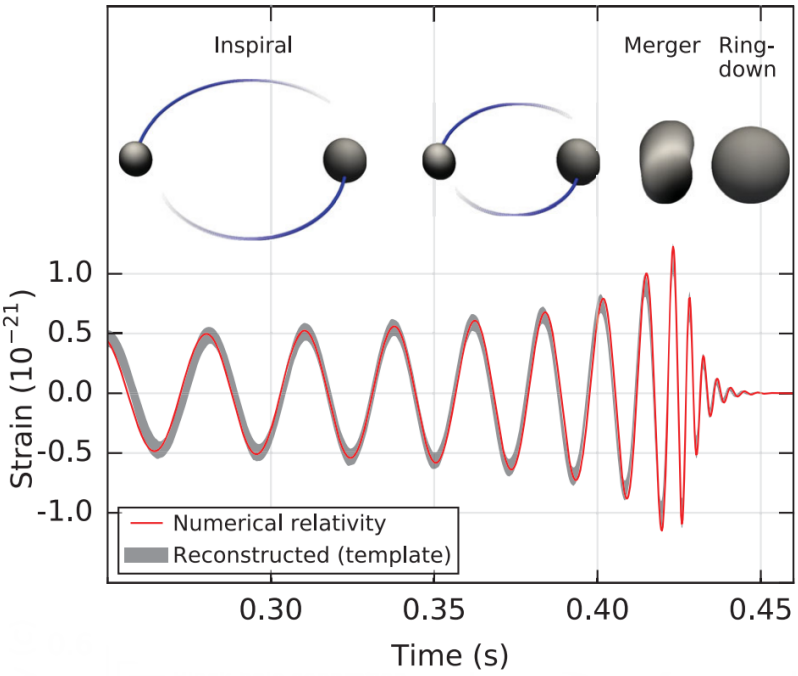

Figure 1: Estimated gravitational-wave strain amplitude from GW150914 detected by LIGO projected onto on of the detectors with illustration of stages of coalescence. Figure adapted from Fig 2. in [5].

The GW are quadrupol waves where the srain amplitude h is proportional to the second derivative of the quadrupol moment Q:

$$h \propto \frac{\ddot{Q}}{r} = \frac{\mu a^2\omega^2}{r}, \tag{8}$$

at a distance r with the reduced mass $\mu = m_1m_2/(m_1 + m_2)$, orbital frequency ω of the system, and elliptical semi-major axis a. The frequency of the GW is directly to the orbital frequency:

$$f_{\mathrm{GW}} = \omega/\pi \tag{9}$$

[4].

Another type of GW, continuous gravitational waves (CW), are assumed to be mainly produced by fast spinning asymmetric neutron stars (NS). There also is a possibility of CW emission by potential Dark matter candidades, boson stars, or so-called Thorne-Żytkow Objects. For NS, the GW induced strain $h \propto I f_{\mathrm{gw}}^2/r$ is proportional to the the moment of inertia I of the star, it's ellipticity ϵ, the frequency of the emitted GW $f_{\mathrm{gw}} \sim f_{\mathrm{spin}}$, and indirectly proportional to the star's radius r. CW are estimated to be in the order of $h \approx 10^{-25}$ or less. So far, no CW signal has been observed. It is proposed that ET could detect signals from near NS and/or NS with high spin frequency [6, 4, 10].

Burst gravitational waves are created in non-spherical core-collapse supernovas of stars. The bursts happen in a very small time frame of a few ms with a strain magnitude of $h \approx 10^{-17}$. These types of GW have also not been observed so far. This could be because the diversity of the emission mechanisms makes it difficult to distinguish the signal out of the noise. As such it is not guaranteed that ET will be able to detect them. Another potential type of burst GW could be the result of magnetar giant flares or pulsar glitches. The theory on them is quite shaky however, due to a lack of a detailed knowledge of these processes [6, 4, 11].

The final category of GW is occupied by stochastic gravitational waves. These denote weak, randomly timed signals from the gravitational wave background (GWB) of the universe. Naturally, these stochastic gravitational waves are devoid of any particular waveform or frequency pattern [4].

2.1.3 Gravitational wave detection

The relevant method to detect GWs is using an advanced Michelson interferometer. The first GW event ever detected is GW150914, a spacetime ripple created by a binary black hole merger which was captured by the ground-based GW observatory LIGO in 2015 [5]. LIGO uses a 1064 nm Nd:YAG laser with a power of $P = 20$ W and a modified two-armed interferometer with orthorgonal arms with lengths of 4 km each. The presence of GW modifies the arm lengths L according to the following relation:

$$\Delta L(t) = \delta L_x - \delta L_y \propto h(t) L, \tag{10}$$

where ΔL is the length change and $h(t)$ the GW strain amplitude in time. As illustrated in Figure 2, the initial laser light is split into two parts at the beamsplitter (BS) and subsequently feeds into the two interferometer arms. Each arm is equipped with an optical cavity for signal amplification. Both beams are reflected back onto the BS, where the differential length variation induced by GW propagating through the setup alters the phase difference between the two light fields. Hence after reconnection, an optical signal proportional to the GW strain is transmitted to the photodetector.
The geometry of the detector design affects certain sensitivities that need to be evaluated against each other. For example, two L-shaped detectors where the arms of the two detectors are parallel to each other when taking earths rotation into account maximizes the sensitivity to stochastic backgrounds but minimizes accuracy on angular localization and reconstruction of the distance of GW sources. If the detectors are at a tilted by 45° to each other, then the setup is blind to stochastic backgrounds but angular localization and distance reconstruction is maximized. Detector geometry is also dependent on other factors [4, 5, 12, 13].

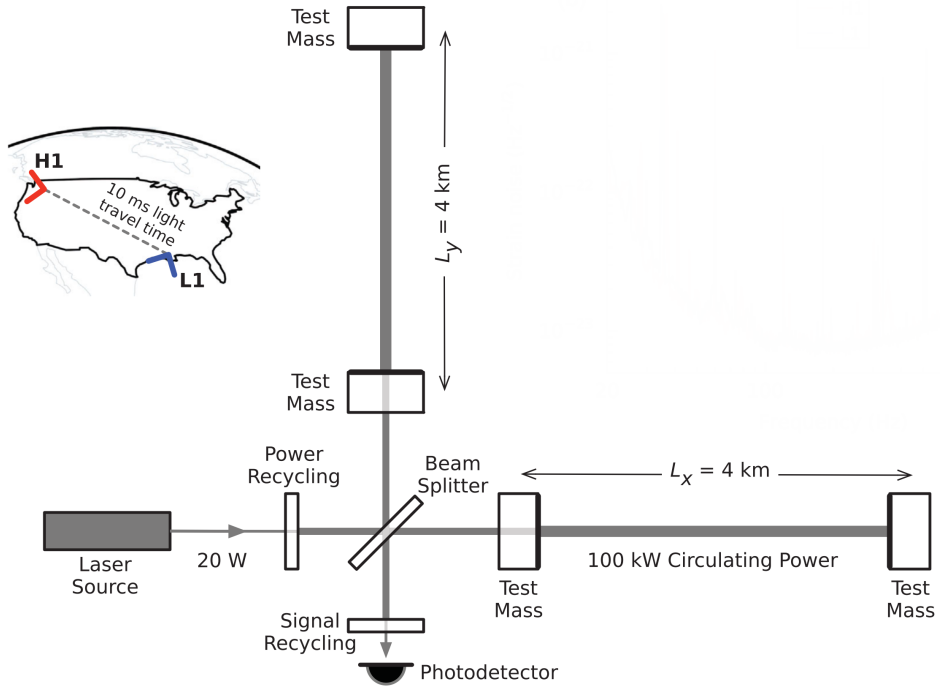

Figure 2: Simplified diagram of an Advanced LIGO detector (not to scale). The interferometer arms are equipped with resonant optical cavities formed by two test mass mirrors each, that multiply the effect of GWs by a factor of 300. LIGO uses two detectors, one at Hanford, WA (H1), and one at Livingston, LA (L1). Figure adapted from Fig 3. in [5].

Given the low order of magnitude of the strain parameter h, GW observatories must be highly resistant to noise. For reference, Figure 3 shows the proposed limitations in sensitivity to frequency dependent strain noise and thus the resolvable redshift limits of the Advanced LIGO upgrade and the future third generation GW observatories ET and Cosmic Explorer (CE) [14].

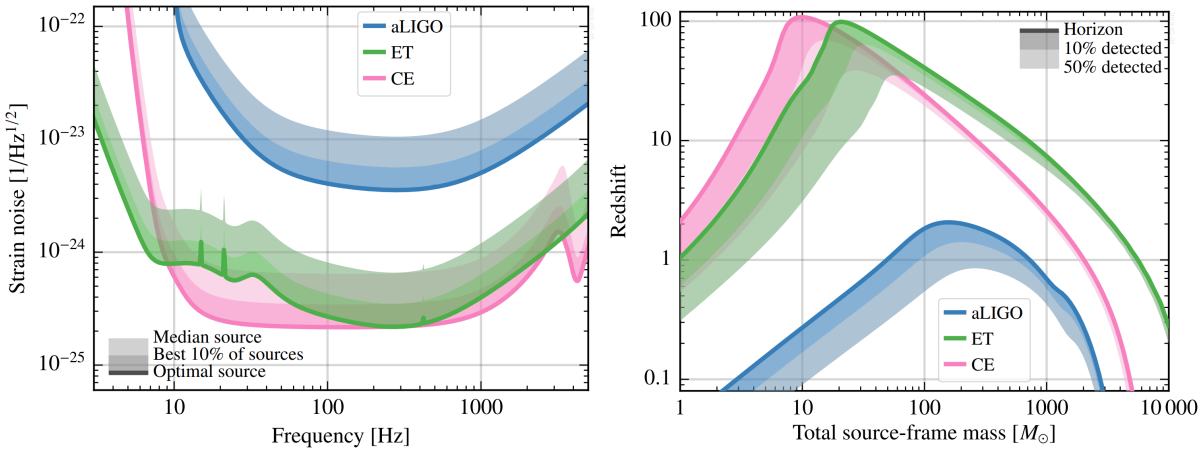

Figure 3: Left: Expected strain noise for monochromatic sources distributed isotropically in sky location and inclination resolvable by aLIGO and the third gen GW observatories ET, and CE. Right: Redshift limits for equal-mass, nonspinning binaries similarly distributed [14].

Considering that the different GW signatures are located within differing frequency ranges, there is a multitude of noise sources with their own frequency ranges to consider [4].

2.2 Einstein Telescope

The Einstein Telescope (ET) is a third generation GW observatory currently in planning. Main goal of the ET is to observe GW signals emitted by events at distances corresponding to redshifts of $z \sim 20$ or higher, especially of merger events of binary black holes and NS. This allows a look into the early universe where the first stars, black holes and galaxies formed which could provide new insights into the most pressing problems in fundamental physics and cosmology [6, 14]. Beside coalescing binary systems, ET may also be able to detect types of GW signals that haven't been observed thus far, such as GW from core collapse supernovae, isolated NS, and may even be able to provide a basis for future studies of the stochastic GW background. As shown in Figure 3, the ET attempts to increase the sensitivity by one order of magnitude compared to the current generation of GW observatories' limits. It is currently planned to be a either a single observatory containing three detectors arranged in a triangle shape as illustrated in Figure 4, or as two L-shaped observatories located in different places. It will located 200-300 meters underground in order to significantly reduce seismic noise [6, 12].

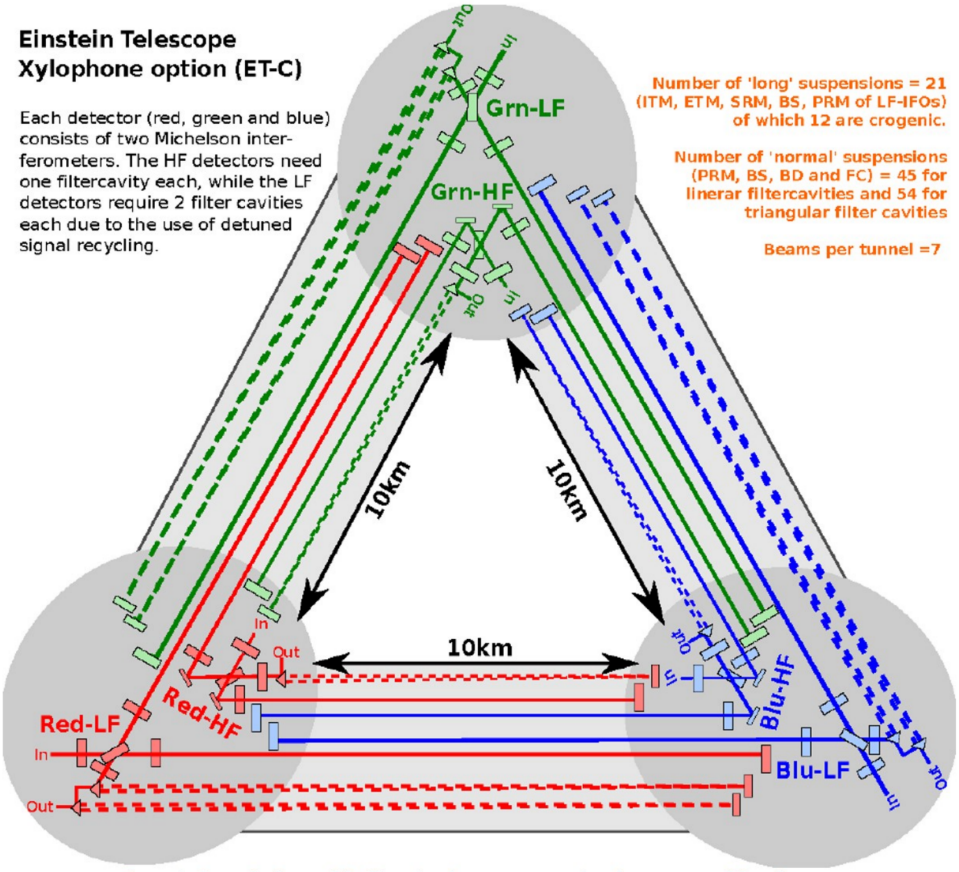

Figure 4: General scheme of the Einstein telescope representing the geometry of the telescope. All three detectors are color coded. The arm lengths are not final [15].

In case of triangular design, the ET will use three detectors. Their purpose is to provide redundancy, resolve GW polarizations, and to provide a veto against disturbances in the form of a null stream, where outputs are combined in a way that results in the GW signal canceling. Each of the detectors will consist of two interferometers, one for high frequencies (HF) at high laser power (high temperatures) and one for low frequencies (LF) at low laser power (low temperatures). The baseline geometry uses arms with lengths of 10 km each, but 15 km are also considered for higher sensitivity. The angles between the arms are 60° which eliminates any directional blind spots due to the polariza-

tion of the GWs. In the case of two L-shaped detectors, lengths of either 15 km or 20 km are considered with an angle between the two detectors of either 0° or 45°. The different possible configurations have a multitude of benefits and drawbacks between each other in regards to sensitivity towards all sorts of parameters such as GW source, individual source parameters, directional sensitivity, signal-to-noise ratio, etc. Overall, the 15 km 2L option with arms at 45° and the triangle with 15 km arms seem to have very similar performances for the reconstruction of all parameters of compact binary coalescences, except for luminosity distance, for which the L-shaped design is significantly better. It also avoids a problem that the triangle configuration would have: correlated noise. Since all optical components for a single location are relatively close to each other compared to two detectors with hundreds of kilometers of distance between them, localized noises could spoil sensitivity. A boon of the triangular design on the other hand is a null stream, where the GW signal cancels. This feature makes it possible to detect and filter out instrumental noise artefacts such as glitches and other systematic errors that may otherwise appear as false positives [6],[12].

2.2.1 Noise sources

Raw strain signals are interlaced with many different types of strain noise. In order to achieve the desired sensitivity, ET needs to be able to significantly limit the effects of different types of noise that distort or conceal GW signals. There are technical noises, such as laser frequency and intensity instability induced noise, and acoustic and seismic noise. Other than that, interferometer sensitivity is also affected by thermal, Newtonian, and quantum noise [14]. The noise levels of these different noise types on ET's high frequency (HF) and low frequency (LF) detectors that ET is slated to achieve are shown in Figure 5. As short description of each noise type follows.

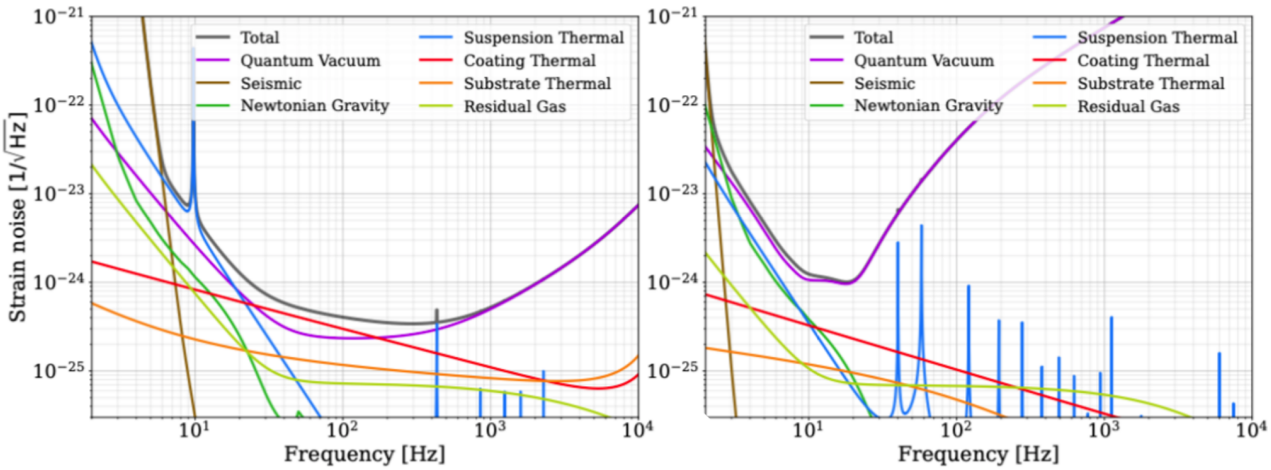

Figure 5: Strain noise budget for the ET HF detectors (left) and LF detectors (right). Figure adapted from Fig. 1 and Fig. 2 [16].

Thermal noise describes signals produced by random displacements of the mirror surfaces in response to thermally fluctuating stresses in the mirror coatings or substrates, and collisions of the optical elements with particles around them that exhibit stochastic random motion. Effects of thermal noise can be avoided when operating optical elements cryogenic temperatures and mitigated to a certain degree by working with large beam sizes [7, 17].

Newtonian noise comes from density fluctuations of the earth due to seismic waves, and from atmospheric density changes. These result in varying gravitational forces enacting on the interferometer elements. This gravity gradient noise can only be reduced, by specifically choosing a detector location

where the surrounding soil is as homogeneous as possible [7].

Seismic noise specifically denotes the effects of vibrations caused by seismic ground motion. Other than choosing a location with minimal seismic vibrations, this type of noise can be mitigated by employing a combination of active and passive vibration isolation techniques such as pendulum suspension, and position and inertial sensors for actuator based active damping [7].

Quantum noise describes both random buffeting of the suspended interferometer mirrors induced by the quantum mechanical amplitude fluctuations of the light field (quantom radiation pressure noise (QRPN)), and the quantum phase uncertainty in determining the phase difference between two light fields (shot noise (SN)). QRPN dominates at low frequencies from ca. 10 to 50 Hz, while SN is dominant at frequencies above ca. 200 Hz. As such, both types of quantum noise scale in opposite ways with light power. Quantum noise can hence best be mitigated by using two interferometers instead of one, where one operates a high laser power and the other one at low power. QRPN can be additionally reduced by using heavy mirrors that provide high resistance against the radiation pressure. An advanced filtering technique using non-classical light can also be used to achieve further quantum noise reduction [7].

Residual gas noise arises from the fact that even though the space between the interferometer mirrors is vacuum, a perfect vacuum containing no particles at all cannot be created. The residual gas particles occupying the space cause fluctuations in the refractive index within the arms the observatory [7].

At this point it is not clear to what degree these noises can be suppressed until "fundamental limitations" are reached. Hence it's important to eradticate technical noises as best as possible [7].

2.3 2D Phase camera

The goal of the ET group at ECAP is to build a phase camera in order to study the effect of certain error sources. Specifically, this encompasses the effects of optical misalignments, errors in the planarity of mirror planes, inhomogenities in the refractive indices of optical element coatings, and thermal lensing, which is an optical effect where laser induced heat causes the refractive index of an optical element to change, leading to a lensing effect [18]. In contrast to current phase cameras in existing GW detectors, this camera is specially designed for the use at a wavelength of 1550 nm, and uses individual multimode fibers as pixels in a pixel array [19]. There are different designs in mind, the version currently in development is a two dimensional camera with 64 pixels. The phase camera makes use of heterodyne detection, which is a method where a primary light signal is superimposed with another light signal which possesses a frequency shift relative to the primary one. The resulting beating pattern of the combined signal can then be captured by a photodetector [20]. Herefore, as illustrated in Figure 6, the initial laser beam is split into two parts. A frequency shift is imposed on one of the two parts by a acousto-optic modulator (AOM). The AOM, in this case an acousto-optic frequency shifter, creates a Doppler shift on the incoming light by imposing a sound wave on an internal optical grating, causing oscillating mechanical strain in the material [21, 22]. This frequency shifted half of the laser signal is provides the reference signal for heterodyne detection. The other part of the initial beam, or test beam, is fed into an electro-optic modulator (EOM), which employs a sinusoidal electric field to modify the refractive index of a nonlinear crystal [23], upon which a symmetric constellation of frequency sidebands is created around the carrier frequency. This is done because the optical cavities of GW observatories apply the Pound-Drever-Hall technique to acquire an error signal that can be used to control the optimal length of the cavity. The signal superimposed with frequency shifted sidebands can be demodulated to obtain a signal that is proportional to the deviation from resonance [7]. AOM and EOM drive signals are synchronized by a GPS-synchronized oscillator to the same frequency to

avoid artificial phase shifts. This also applies to the signal processing unit (see Section 3.3) following the fiber array [19]. After the recombined laser signal is captured by individual photodiodes, the beat frequency created by overlapping carrier and frequency sidebands of the test beam, and the frequency of the reference beam, can then be demodulated and phase and amplitude of all beam parts obtained [24].

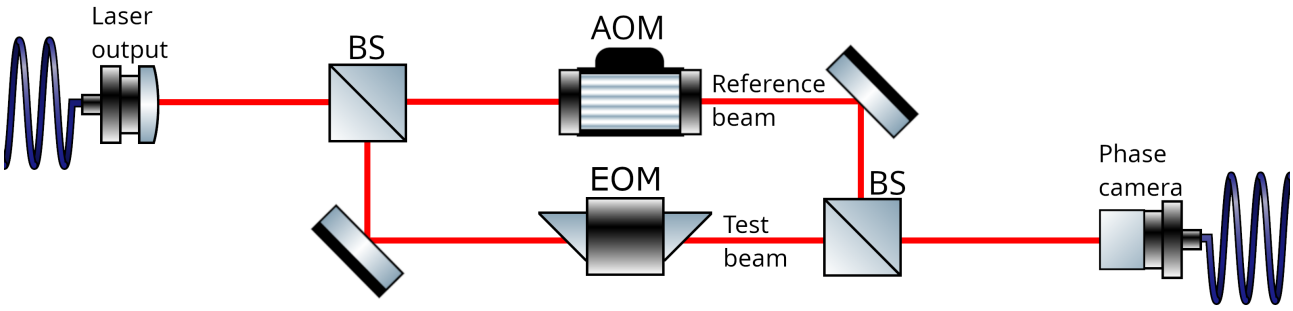

Figure 6: Simplified sketch of the optical setup for the phase camera. Initial laser light coming from the left is split by beamsplitter (BS) into reference and test beam sections, recombined at second BS, and then recorded with the phase camera. For a more detailed sketch see Figure 11. Illustration created with components from [25].

2.4 Geometric optics

In order to study a the phase profile of a laser beam, especially for comparing phase measurements to theory, it is crucial to understand how the beam progresses through the optical setup until it reaches the fiber array. With geometric optics we can track the evolution of a laser beam's shape over propagation distance and how optical elements in its path transform its parameters. This also enables us to design an optical setup in regards to achieving desired beam profiles through calculating optimal positions for optical elements.

2.4.1 Gaussian beams

For calculations with laser beams we can use the Gaussian beam model. Arguably the most important parameters to characterize a Gaussian beam are its radius $w(z)$ and radius of curvature $R(z)$ on an optical axis z which are described by

$$w(z) = w_0 \sqrt{1 + \left(\frac{z}{z_R}\right)^2}, \tag{11}$$

$$R(z) = z \left(1 + \left(\frac{z_R}{z}\right)^2\right). \tag{12}$$

While $w(z)$ is the transversal radius of the laser spot, $R(z)$ describes the longitudinal radius of the curved wavefront of the light [26]. w_0 is the radius at the location on the focus, or waist, and the Rayleigh length z_R describes the distance from the focus, at which the the beam translates from near- to far field. The Rayleigh length is characterized as

$$z_R = \frac{\pi w_0^2 n}{\lambda}, \tag{13}$$

with refractive index n of the medium that the beam propagates through and wavelength λ of the light [26, 27, 28]. The electric field of a laser beam propagating along an optical axis z according to

the Gaussian beam model can be expressed as

$$E(x, y, z, t) = U\hat{e}\Psi_{mn}(x, y, z)e^{i\omega t} \tag{14}$$

with transverse coordinates x and y, amplitude U, unit vector $\hat{e}$ of polarization, and angular frequency ω. The wave function $\Psi_{nm}(x, y, z)$ governs the spacial evolution of the electric field. The indices m and n denote the transverse mode numbers of Hermite-Gaussian modes. Taking only the fundamental Gaussian mode with $m = 0$ and $n = 0$ into account we can express this wave function $\Psi_{00}(x, y, z)$ as

$$\Psi_{00}(x, y, z) = \sqrt{\frac{2}{\pi}}\frac{1}{w(z)}e^{-\frac{kr^2}{2R(z)}}e^{-i\Phi_{00}(x,y,z)}, \tag{15}$$

with $r = \sqrt{x^2 + y^2}$ and the wave number $k = \omega/c$. The first exponential term in Equation 15 dictates the transversal, radial extinction of the electric field strength, while Φ_{00}^j denotes the phase of the light and can be expanded to

$$\Phi_{00} = kz + \frac{kr^2}{2R(z)} - \phi_{00}(z), \tag{16}$$

which includes a transversal, radially symmetric phase term, and two longitudinal phase terms. kz increases linearly with distance, while the term ϕ_{00}, or Gouy phase, is a marginal phase shift that inverts at the focus:

$$\phi_{00} = \arctan\left(\frac{z}{z_R}\right) \tag{17}$$

[8].

For simulations comparing recorded data with theory, we want to both look at expected phase profiles of the test beam, that are described by Equation 16, but also its intensity profile which can be defined as

$$I(\mathbf{r}, t) = E(\mathbf{r}, t)E^*(\mathbf{r}, t) \tag{18}$$

[29].

Working with real laser beams instead of perfect theoretical Gaussian beams means that we need to take the quality factor M^2 into account. M^2 denotes how much the parameters of a real Gaussian beam differ from an ideal beam. Using the model for laser beams with constant beam waists, the Rayleigh length modifies to

$$z_R = \frac{\pi w_0^2 n}{M^2\lambda}. \tag{19}$$

A perfect Gaussian shape has $M^2 = 1$, in contrast to real laser beams with $M^2 > 1$. There is multiple different ways how a beam can differ to an ideal shape depending on waist size and beam divergence. For example, a beam could have an ideal focus, with divergence larger than for $M^2 = 1$, or an ideal divergence but a larger focus for $M^2 = 1$. In this work the latter option was determined to be most accurate when comparing calculations to beam measurements [30].

2.4.2 2x2 Beam transfer matrix optics

The propagation of Gaussian beams with beam radius $w(z)$ (Equation 13) and radius of curvature $1/R(z)$ (Equation 12) on an optical axis z through an optical system can be traced with the usage of a beam transfer matrix:

$$\begin{bmatrix} q_1(z_{\text{in}}) \\ 1 \end{bmatrix} = k \begin{bmatrix} A & B \\ C & D \end{bmatrix} \begin{bmatrix} q_2(z_{\text{out}}) \\ 1 \end{bmatrix}. \tag{20}$$

$q1(z_{\text{in}})$ is the so called complex beam parameter at the location of the beginning of the optical system on the z-axis, while $q_2(z_{\text{out}})$ describes the parameter at it's output position [27],[28]. For some components like thin lenses, this position is the same ($z_{\text{in}} = z_{\text{out}}$), while when working with components like thick lenses, both locations need to be distinguished. The matrix elements A, B, C, and D are dependent on the optical components, with k a scaling factor. For convenience, the complex beam parameter $q(z)$ is usually expressed in reciprocal form:

$$\frac{1}{q(z)} = \frac{1}{R(z)} - \frac{iM^2\lambda}{\pi n w^2(z)} = \frac{1}{z + iz_R}. \tag{21}$$

It is generally useful to substitute z in Equation 12, Equation 13 and Equation 21 with $z = z - z_0$ to separate a lab system from the beam system, otherwise the location $z = 0$ is always defined as the waist location. At latest by the step at Equation 25 and Equation 26 this is absolutely necessary, otherwise the system of the transformed beam will be decoupled from the original beam. Equation 20 can be simplified to

$$\frac{1}{q_2(z_{\text{out}})} = \frac{C + \frac{D}{q_1(z_{\text{in}})}}{A + \frac{B}{q_1(z_{\text{in}})}} \tag{22}$$

to obtain the complex beam parameter of the modified beam at the output position of the optical system described by the 2x2 matrix. Combining Equations 21 and Equation 22, the output parameters, which we will denote as w_2 and R_2, can be obtained through the separation of real and imaginary parts:

$$w_2(z_{\text{out}}) = \pm \sqrt{\frac{-M^2\lambda}{\pi n \Im\left(\frac{1}{q_2(z_{\text{out}})}\right)}}, \tag{23}$$

$$R_2(z_{\text{out}}) = \frac{1}{\Re\left(\frac{1}{q_2(z_{\text{out}})}\right)}. \tag{24}$$

The $\pm$ in front of Equation 23 represents that mathematically, the beam has a radius in both directions with $r = 0$ on the z-axis. We now know the beam radius and radius of curvature of the new modified beam at the location z_{out}. In order to construct new functions $w_2(z)$ and $R_2(z)$, we have to determine the new waist size $w_{0,2}$ and the new waist position $z_{0,2}$. Combining Equation 13 and Equation 12 with Equation 23 and Equation 24 and using the substitution $z = z - z_0$, we find:

$$w_{0,2} = \pm w_2(z_{\text{out}}) \sqrt{\frac{1}{w_2^4(z_{\text{out}}) \left(\frac{\pi n}{M^2\lambda R_2(z_{\text{out}})}\right)^2 + 1}}, \tag{25}$$

$$z_{0,2} = z_{\text{out}} \pm \frac{\pi w_{0,2}^2 n}{M^2\lambda} \sqrt{\frac{w^2(z_{\text{out}})}{w_{0,2}^2} - 1}. \tag{26}$$

In Equation 26, the $\pm$ represents that at z_{out}, the beam can either be reflected back (-), like in the case of a mirror, or propagated through (+), in the case of a converging lens for example. In contrast, a diverging lens reflects the focus, thus (-) has to be used. The sign that needs to be chosen is therefore dependent on the optical components in use. If we let the beam propagate in the minus direction on the optical axis z, the minus in Equation 26 also has to be chosen.
The new $w_{0,2}$, and $z_{0,2}$ can then be inserted into Equations 13 and 12 to finally obtain functions for the modified beam after the optical system [27, 28].

2.4.3 3x3 Beam transfer matrix optics

2x2 beam transfer matrix optics only works together with the paraxial wave approximation. So in order to take possible misalignments into account a different approach is more useful. A method proposed by A. A. Tovar and L. W. Casperson is to use a 3x3 matrix approach, where A_x, B_x, C_x, and D_x are the usual matrix elements of an aligned optical component, and the additional elements G_x and H_x allow the inclusion of angular tilts and linear offsets from the z-axis. The full operation then looks like this:

$$\begin{bmatrix} u_{x2} \\ \frac{1}{q_{x2}} u_{x2} \\ S_{x2} u_{x2} \end{bmatrix} = \begin{bmatrix} A_x & B_x & 0 \\ C_x & D_x & 0 \\ G_x & H_x & 1 \end{bmatrix} \begin{bmatrix} u_{x1} \\ \frac{1}{q_{x1}} u_{x1} \\ S_{x1} u_{x1} \end{bmatrix} \tag{27}$$

[27],[28].

The terms u_x are similar to the scaling factor k in Equation 20 for the 2x2 case, and are not relevant for further calculations. Alongside the complex beam parameter $q(z)$, this model introduces another complex factor to describe the propagation of the laser beam, the complex displacement parameter S(z), which is defined as

$$S(z) = \beta \left(-\frac{d(z)}{q(z)} + m \right), \tag{28}$$

with $\beta = 2\pi n/(M^2\lambda)$ and the displacement function $d(z) = z\cos\epsilon + d_0$ that describes the offset orthogonal to the optical axis z, which is we define as a linear function with the offset d_0 at the position of the focus, and ϵ the angle between z and the beam's actual axis z'. $m = \frac{\mathrm{d}d(z)}{\mathrm{d}z} = \tan\epsilon$ is then the beam's slope. In this model, q transforms similarly to how it's transformed in the 2x2 case (Equation 22). The transformed displacement parameter S is obtained by:

$$S_2(z_{\text{out}}) = \frac{S_1(z_{\text{in}}) + G + \frac{H}{q_1(z_{\text{in}})}}{A + \frac{B}{q_1(z_{\text{in}})}}. \tag{29}$$

Using a similar algebraic approach to how $w_2(z_{\text{out}})$ and $R_2(z_{\text{out}})$ are calculated, we can obtain $d_2(z_{\text{out}})$ and m_2 as follows:

$$d_2(z_{\text{out}}) = \frac{\Im(S_2(z_{\text{out}}))}{\beta \Im\left(\frac{1}{q_2(z_{\text{out}})}\right)}, \tag{30}$$

$$m_2 = \frac{1}{\beta}\left(\Re(S_2(z_{\text{out}})) - \Im(S_2(z_{\text{out}})) \cdot \frac{\Re\left(\frac{1}{q_2(z_{\text{out}})}\right)}{\Im\left(\frac{1}{q_2(z_{\text{out}})}\right)} \right) \tag{31}$$

Equation 23 and Equation 25 for obtaining beam radii w_2 and w_{02}, Equation 24 for radius of curvature R_2 at the output position, as well as Equation 26 for obtaining the waist location on z are the same in the 3x3 case. However, Equation 26 has to be modified slightly to take into account that the optical axis of the beam z' is on a slope relative to z:

$$z_{0,2} = z_{\text{out}} \pm \frac{\pi w_{0,2}^2 n}{M^2\lambda} \sqrt{\frac{w^2(z_{\text{out}})}{w_{0,2}^2} - 1} \cdot \cos\epsilon_2. \tag{32}$$

Together with the location $z_{0,2}$ of the new waist (Equation 26), the displacement at this new waist can be obtained via

$$d_{0,2} = d_2(z_{\text{out}}) - m_2(z_{\text{out}} - z_{0,2}) \tag{33}$$

[27],[28].

2.4.4 Specific beam transfer matrices

We use three different transfer types in the following calculations, thin lens, thick lens and beamsplitter. The ABCDGH matrix for a (lossless) thin lens is given by

$$M_{\text{thin lens}} = \begin{bmatrix} 1 & 0 & 0 \\ -f^{-1}\cos\theta & 1 & 0 \\ -\beta_{air} x_0 f^{-1}\cos\theta & 0 & 1 \end{bmatrix}, \tag{34}$$

where f is the focal length, θ the tilt, and x_0 an offset of the lens on an axis x perpendicular to z. The thin lens model assumes a thickness of $t = 0$, which neglects the fact that the beam is also affected by traveling through a medium with $n \neq n_{\text{air}}$ inside the lens. Thus calculating with thin lenses introduces a margin of error especially regarding positions on z that amplifies with increasing thickness of the actual lens [27, 28]. As such it is useful to use the thick lens approach. To obtain a transfer matrix for a thick lens, we combine two matrices describing spherical boundaries with one for a homogeneous medium:

$$\begin{aligned} M_{\text{thick lens}} &= T_{\text{spherical boundary}} T_{\text{homogeneous medium}} T_{\text{spherical boundary}} \\ &= \begin{bmatrix} 1 & 0 & 0 \\ (1-\frac{k_{02}}{k_{01}})R_{\text{right}}^{-1}\cos\theta & \frac{k_{02}}{k_{01}} & 0 \\ (k_{02}-k_{01})(\tan\theta + x_0 R_{\text{right}}^{-1}\cos\theta) & 0 & 1 \end{bmatrix} \begin{bmatrix} 1 & t & 0 \\ 0 & 1 & 0 \\ 0 & H_{\text{hm}} & 1 \end{bmatrix} \begin{bmatrix} 1 & 0 & 0 \\ (1-\frac{k_{01}}{k_{02}})R_{\text{left}}^{-1}\cos\theta & \frac{k_{01}}{k_{02}} & 0 \\ (k_{01}-k_{02})(\tan\theta + x_0 R_{\text{left}}^{-1}\cos\theta) & 0 & 1 \end{bmatrix} \end{aligned} \tag{35}$$

with $H_{\text{hm}} = t\tan\theta - L\sin\theta = L\sin\theta(1/\cos\theta - 1)$. R_{left} and R_{right} are the radii of curvature of the thick lens on both sides. The terms k_{0i} with $i = 1, 2$ describe the 0th-order terms of a Taylor series expanded squared complex propagation constant $k^2(x, y, z)$ in the transverse directions, where $k^2 = \mu\epsilon'$ with material permeability μ and complex permittivity ϵ'. Assuming both mediums air and lens to be lossless, we can use $k_0 = \beta$. The terms k_{01}/k_{02} then simplify to n_1/n_2. t describes the thickness of the homogeneous medium, while L describes the center length of the optical element. They are hence the same: $t = L$ [27],[28]. Since the thickness of the optical element changes by tilting it, we need to replace t in the center matrix in Equation 35 with a modulated thickness $t_{\text{mod}} = (z_{\text{out}} - z_{\text{in}})/\cos\epsilon_{12}$ where ϵ_{12} is the tilt angle of the beam inside the lens (see Section 2.4.5).

If we want to investigate how a beamsplitter reshapes the transmitted section of the beam, we can use two tilted linear boundary matrices instead of spherical boundary matrices:

$$\begin{aligned} M_{\text{beamsplitter}} &= T_{\text{linear boundary}} T_{\text{homogeneous medium}} T_{\text{linear boundary}} \\ &= \begin{bmatrix} 1 & 0 & 0 \\ 0 & \frac{k_{02}}{k_{01}} & 0 \\ (k_{02}-k_{01})\tan\theta & 0 & 1 \end{bmatrix} \begin{bmatrix} 1 & t & 0 \\ 0 & 1 & 0 \\ 0 & H_{\text{hm}} & 1 \end{bmatrix} \begin{bmatrix} 1 & 0 & 0 \\ 0 & \frac{k_{01}}{k_{02}} & 0 \\ (k_{01}-k_{02})\tan\theta & 0 & 1 \end{bmatrix} \end{aligned} \tag{36}$$

[27].

2.4.5 Geometric considerations

Once we introduce a tilt θ to the lens in the optical system, or a tilt ϵ to the beam, we can no longer assume the input position z_{in} for the transfer matrix to be equal to the position of the optical element responsible for the transformation. This is illustrated in Figure 7, which shows a scheme of a misaligned thin lens system. As can be seen, the position at which the beam interacts with the

element on z does not necessarily correlate with the position z_{lens}. For a thin lens we can assume $z_{\text{in}} = z_{\text{out}}$.

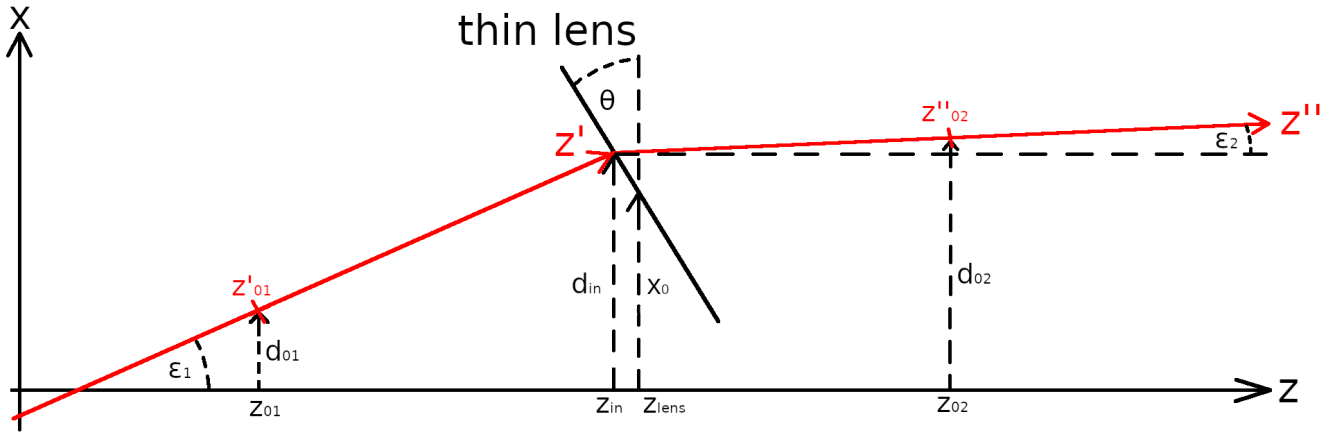

Figure 7: Illustration of beam geometry with thin lens for beam transformation. The beam travels on a misaligned optical axis z' and a separate misaligned axis z'' after it is bent by a misaligned lens.

We can assign a misaligned beam a new optical axis z' different from the referential z-axis by knowing the displacement $d(z)$ of the beam, it's slope $m = \mathrm{d}d(z)/\mathrm{d}z$, and the waist location z_0. We can obtain the angle between z and a beam axis z' with $\epsilon = \arctan(m)$ and subsequently an expression for the beam axis:

$$z' = \frac{z - z_0}{\cos(\epsilon)}. \tag{37}$$

To obtain z_{in} we can use a linear system of equations:

$$\begin{aligned} \tan\theta &= \frac{z_{\text{lens}} - z_{\text{in}}}{d_{\text{in}} - x_0}, \\ \tan\epsilon_1 &= \frac{d_{\text{in}} - d_{01}}{z_{\text{in}} - z_{01}}. \end{aligned} \tag{38}$$

Solving Equation 38 yields the effective lens position $z_{\text{in}} = z_{\text{out}}$:

$$z_{\text{in}} = \frac{z_{\text{lens}} + \tan\theta(x_0 - d_{01} + z_{01}\tan\epsilon_1)}{\tan\theta\tan\epsilon_1 + 1}. \tag{39}$$

Figure 8 shows the geometric scheme for a thick lens system. Contrary to the parameterization a thin lens, which is described as a single object with one location, here we have to take position parameters of two spherical boundaries into account. While the angle θ remains the same for both, we now have two offsets x_1 and x_2 at two separate locations on z-axis z_{x1} and z_{x2}. Additionally, the input and output positions are not the same: $z_{\text{in}} \neq z_{\text{out}}$.

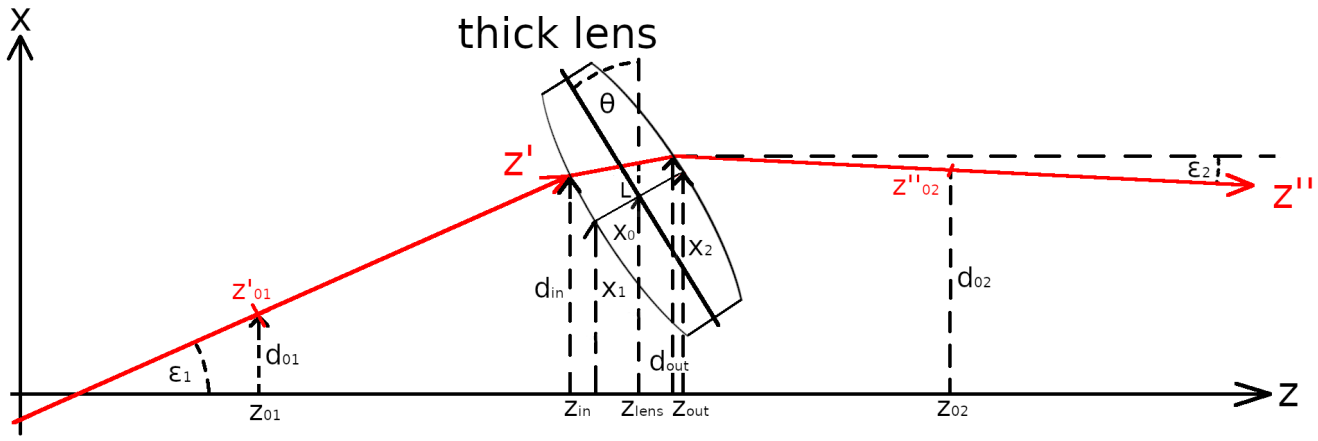

Figure 8: Illustration of beam geometry with thick lens for beam transformation. The thick lens is approximated by a three parts matrix element which' components have different (but linked) position parameters.

We want to describe the thick lens as a single unit at a position z_{lens} with tilt θ and linear offset x_0 from the z-axis, were x_0 describes the offset from the center of an untilted lens at z_{lens} similarly to the thin lens case. We can use simple trigonometry with

$$\begin{aligned} \sin\theta &= \frac{x_0 - x_1}{0.5L}, \qquad \cos\theta = \frac{z_{\text{lens}} - z_{x1}}{0.5L}, \\ \sin\theta &= \frac{x_2 - x_0}{0.5L}, \qquad \cos\theta = \frac{z_{x2} - z_{\text{lens}}}{0.5L}, \end{aligned} \tag{40}$$

to determine the offsets $x_{1,2}$ and positions $z_{x1,x2}$ of the two spherical boundaries:

$$\begin{aligned} x_1 &= x_0 - \frac{L}{2}\sin\theta, \qquad z_{x1} = z_{\text{lens}} - \frac{L}{2}\cos\theta, \\ x_2 &= x_0 + \frac{L}{2}\sin\theta, \qquad z_{x2} = z_{\text{lens}} + \frac{L}{2}\cos\theta. \end{aligned} \tag{41}$$

Next we need to find the input and output position of the matrix system, i.e. the positions where the beam meets with the boundaries. This means that we have to know the slope m_{12} of the beam inside the lens to determine z_{out}. The beam transformation must hence be split into two parts. Additionally to the second function in Equation 38 describing the initial beam path, we need a similar function describing beam path inside the lens. We obtain

$$\begin{aligned} \tan\epsilon_1 &= \frac{d_{\text{in}} - d_{01}}{z_{\text{in}} - z_{01}}, \\ \tan\epsilon_{12} &= \frac{d_{\text{out}} - d_{012}}{z_{\text{out}} - z_{012}}. \end{aligned} \tag{42}$$

To determine $z_{\text{in,out}}$ and $d_{\text{in,out}}$ we need an expression for the spherical surface of the lens intersecting with the linear line describing the beam path. We can calculate the position of the center of the sphere describing the lens surface as follows:

$$\begin{aligned} x_{\text{C1}} &= x_1 + R\sin\theta, \qquad z_{\text{C1}} = z_{x1} + R\cos\theta, \\ x_{\text{C2}} &= x_2 - R\sin\theta, \qquad z_{\text{C2}} = z_{x2} - R\cos\theta. \end{aligned} \tag{43}$$

The intersections (z_{in}, d_{in}) and (z_{out}, d_{out}) are then where the distance to the sphere centers is exactly R with

$$R^2 = (z_{\text{C1,2}} - z_{\text{in,out}})^2 + (x_{\text{C1,2}} - d_{\text{in,out}})^2. \tag{44}$$

Combining Equation 44 with Equations 42 yields a linear system of equations which upon solving lets us arrive at

$$\begin{aligned} z_{\text{in}} &= \frac{-b_{\text{in}} - \sqrt{b_{\text{in}}^2 - 4a_{\text{in}}c_{\text{in}}}}{2a_{\text{in}}}, \\ z_{\text{out}} &= \frac{-b_{\text{out}} + \sqrt{b_{\text{out}}^2 - 4a_{\text{out}}c_{\text{out}}}}{2a_{\text{out}}}, \end{aligned} \tag{45}$$

with

$$\begin{aligned} a_{\text{in}} &= 1 + \tan^2\epsilon_1, \\ b_{\text{in}} &= -2(z_{\text{C1}} + \tan\epsilon_1(x_{\text{C1}} - d_{01} + z_{01}\tan\epsilon_1)), \\ c_{\text{in}} &= z_{\text{C1}}^2 + x_{\text{C1}}^2 - R^2 + (z_{01}\tan\epsilon_1 - d_{01})^2 + 2x_{\text{C1}}(z_{01}\tan\epsilon_1 - d_{01}), \end{aligned} \tag{46}$$

and

$$\begin{aligned} a_{\text{out}} &= 1 + \tan^2\epsilon_{12}, \\ b_{\text{out}} &= -2(z_{\text{C2}} + \tan\epsilon_{12}(x_{\text{C2}} - d_{012} + z_{012}\tan\epsilon_{12})), \\ c_{\text{out}} &= z_{\text{C2}}^2 + x_{\text{C2}}^2 - R^2 + (z_{012}\tan\epsilon_{12} - d_{012})^2 + 2x_{\text{C2}}(z_{012}\tan\epsilon_{12} - d_{012}). \end{aligned} \tag{47}$$

d_{in} and d_{out} can then be obtained from Equation 42:

$$\begin{aligned} d_{\text{in}} &= (z_{\text{in}} - z_{01})\tan\epsilon_1, \\ d_{\text{out}} &= (z_{\text{out}} - z_{012})\tan\epsilon_{12}. \end{aligned} \tag{48}$$

Geometry for a beamsplitter is similar to thick lens geometry but with linear instead of spherical surfaces (see Figure 9). This means that we can use Equation 39 for the input position z_{in} by replacing the parameters z_{lens} with z_{x1} to obtain Equation 49.

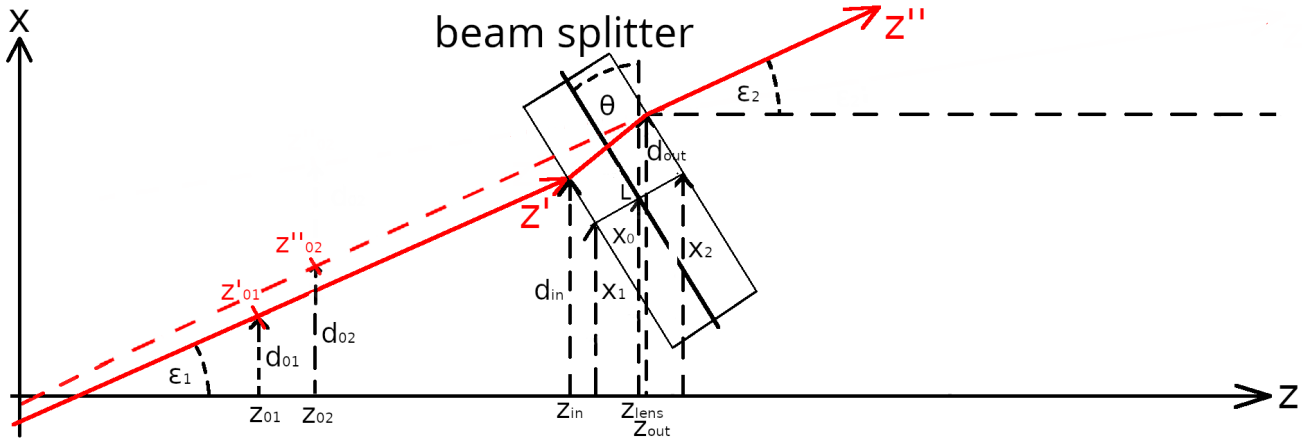

Figure 9: Illustration of beam geometry with beamsplitter for beam transformation. The beamsplitter is approximated by a three parts matrix element which' components have different (but linked) position parameters.

$$z_{\text{in}} = \frac{z_{\text{x1}} + \tan\theta(x_1 - d_{01} + z_{01}\tan\epsilon_1)}{\tan\theta\tan\epsilon_1 + 1} \tag{49}$$

To calculate the output position z_{out} we follow the same principle, but similarly to the thick lens case we need parameters of the beam inside of the optical element. With the tilt ϵ_{12}, offset d_{12} at waist position, and waist position z_{012} of the beam inside the beamsplitter, this yields

$$z_{\text{out}} = \frac{z_{\text{x2}} + \tan\theta(x_2 - d_{012} + z_{012}\tan\epsilon_{12})}{\tan\theta\tan\epsilon_{12} + 1}. \tag{50}$$

Obtaining x_1, z_{x1}, and x_2, z_{x2} follows the same exact approach as for a thick lens. We arrive at:

$$\begin{aligned} x_1 &= x_0 - \frac{L}{2}\sin\theta, \qquad & z_{x1} &= z_{\text{bs}} - \frac{L}{2}\cos\theta, \\ x_2 &= x_0 + \frac{L}{2}\sin\theta, \qquad & z_{x2} &= z_{\text{bs}} + \frac{L}{2}\cos\theta, \end{aligned} \tag{51}$$

with z_{bs} the center location of the beamsplitter and x_0 the corresponding offset from the optical axis z at z_{bs}.

2.4.6 Fiber Collimators

Often the first step in a laser setup is to collimate the laser output. In our case, we are using a fiber-coupled laser [31], and thus a fiber collimator. Like illustrated in Figure 10, the laser beam which is diverging after exiting the fiber is reshaped by a lens system, that is about one focal effective focal length f' away from the fiber end, into a approximately flat wavefront. If the distance is smaller, then the beam will diverge, and if it's larger than f' it will converge to a focus at some distance [32].

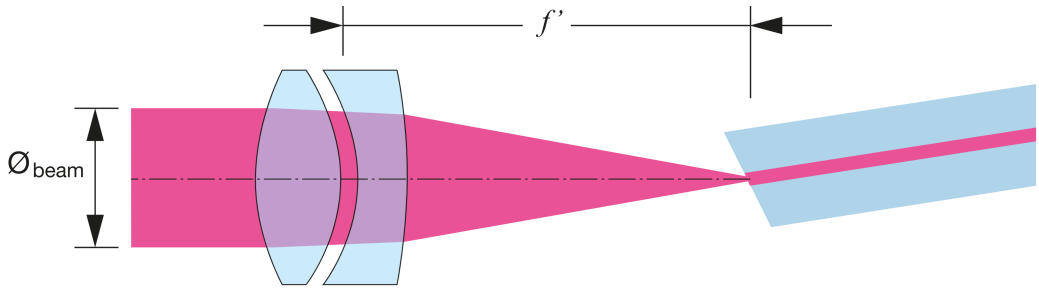

Figure 10: Sketch of the function of a fiber collimator for single-mode fibers [33].

One method to approximate the diameter of the collimated beam is to use the wavelength dependent mode field diameter MFD of the fiber as a waist diameter with $w_0 = 0.5 \cdot MFD$ and the fiber end as the position of the waist from which the beam diverges. Beam radius $w(z)$ (Equation 13) and Rayleigh length z_R (Equation 19) thus become:

$$w(z) = \frac{MFD}{2}\sqrt{1 + \left(\frac{z}{z_R}\right)^2}, , \tag{52}$$

$$z_R = \frac{\pi n}{M^2 \lambda}\left(\frac{MFD}{2}\right)^2. \tag{53}$$

Placing the effective collimator lens with f' at $z_0 + f'$ then allows to calculate the parameters of the beam produced by the collimator with the beam transfer matrices in Section 2.4.2 and Section 2.4.3 [34].

2.4.7 2D camera coordinate system

After mathematically tracking the shape of the laser beam through the entire optical setup, we can then simulate how it's final shape is perceived by the perspective of the phase camera. This allows us to compare measurements with theory. Starting from a lab system with coordinates $\vec{r} = (x, y, z)^\intercal$, we can translate over into the coordinate system of a 2D camera $\vec{r_C} = (x_C, y_C, z_C)^\intercal$ via two 3x3 rotational matrices R_x and R_y that describe rotation around the x and y axis:

$$\vec{r_C} = R_x(\alpha_y)R_y(\alpha_x)(\vec{r} - \vec{d_C}) = \begin{pmatrix} 1 & 0 & 0 \\ 0 & \cos\alpha_y & -\sin\alpha_y \\ 0 & \sin\alpha_y & \cos\alpha_y \end{pmatrix} \begin{pmatrix} \cos\alpha_x & 0 & \sin\alpha_x \\ 0 & 1 & 0 \\ -\sin\alpha_x & 0 & \cos\alpha_x \end{pmatrix} \begin{pmatrix} x - d_{Cx} \\ y - d_{Cx} \\ z - z_{\text{cam}} \end{pmatrix} \tag{54}$$

[35].

with the offset vector $\vec{d_C} = (d_{Cx}, d_{Cy}, z_{\text{cam}})$ that includes the camera offsets in x- and y-direction, as well as the camera position z_{cam} on the optical axis z. The rotational angles α_x and α_y are the tilt angles of the camera relative to the lab system. α_x describes the angle between x and x_C, which equates to a rotation around the y-axis, and α_y denotes the angle between y and y_C, and a thus a rotation around the x-axis.

To simulate the transverse profile of a Gaussian beam's intensity and phase on the camera surface however, we need to use the camera axes as input parameters. Hence we perform a rotation in the opposite direction:

$$
\begin{aligned}
\vec{r} - \vec{d_C} &= R_x(-\alpha_y) R_y(-\alpha_x) \vec{r_C} \\
&= \begin{pmatrix} 1 & 0 & 0 \\ 0 & \cos(-\alpha_y) & -\sin(-\alpha_y) \\ 0 & \sin(-\alpha_y) & \cos(-\alpha_y) \end{pmatrix} \begin{pmatrix} \cos(-\alpha_x) & 0 & \sin(-\alpha_x) \\ 0 & 1 & 0 \\ -\sin(-\alpha_x) & 0 & \cos(-\alpha_x) \end{pmatrix} \begin{pmatrix} x_C \\ y_C \\ z_C \end{pmatrix} \\
&= \begin{pmatrix} \cos(-\alpha_x) x_C + \sin(-\alpha_x) z_C \\ \sin(-\alpha_y)\sin(-\alpha_x) x_C + \cos(-\alpha_y) y_c - \sin(-\alpha_y)\cos(-\alpha_x) z_C \\ -\sin(-\alpha_x)\cos(-\alpha_y) x_C + \sin(-\alpha_y) y_C + \cos(-\alpha_x)\cos(-\alpha_y) z_C \end{pmatrix}.
\end{aligned} \tag{55}
$$

The camera surface is always located at $z_C = 0$, thus all factors in Equation 55 multiplied with z_C can be discarded. Moving the offset vector $\vec{d_C}$ to the other side, we obtain

$$
\begin{pmatrix} x(x_C) \\ y(x_C, y_C) \\ z(x_C, y_C) \end{pmatrix} = \begin{pmatrix} x_C \cos(\alpha_x) + d_{Cx} \\ x_C \sin(\alpha_y)\sin(\alpha_x) + y_C \cos(\alpha_y) + d_{Cy} \\ x_C \sin(\alpha_x)\cos(\alpha_y) - y_C \sin(\alpha_y) y_C + z_{\text{cam}} \end{pmatrix} \tag{56}
$$

as the lab coordinates. Next, we perform another rotation from the lab coordinate system $\vec{r} = (x, y, z)^\intercal$ into the coordinate system of the laser beam $\vec{r_b} = (x_b, y_b, z_b)^\intercal$ via

$$
\begin{aligned}
\vec{r_b} = R_x(\epsilon_y) R_y(\epsilon_x)(\vec{r} - \vec{d_0}) &= \begin{pmatrix} 1 & 0 & 0 \\ 0 & \cos\epsilon_y & -\sin\epsilon_y \\ 0 & \sin\epsilon_y & \cos\epsilon_y \end{pmatrix} \begin{pmatrix} \cos\epsilon_x & 0 & \sin\epsilon_x \\ 0 & 1 & 0 \\ -\sin\epsilon_x & 0 & \cos\epsilon_x \end{pmatrix} \begin{pmatrix} x - d_{0x} \\ y - d_{0x} \\ z - z_0 \end{pmatrix} \\
= \begin{pmatrix} x_b(x, z) \\ y_b(x, y, z) \\ z_b(x, y, z) \end{pmatrix} &= \begin{pmatrix} \cos\epsilon_x (x - d_{0x}) + \sin\epsilon_x (z - z_0) \\ \sin\epsilon_y \sin\epsilon_x (x - d_{0x}) + \cos\epsilon_y (y - d_{0C}) - \sin\epsilon_y \cos\epsilon_x (z - z_0) \\ -\sin\epsilon_x \cos\epsilon_y (x - d_{0C}) + \sin\epsilon_y (y - d_{0C}) + \cos\epsilon_x \cos\epsilon_y (z - z_0) \end{pmatrix}.
\end{aligned} \tag{57}
$$

[write this part again in own words, that leaves out overly technical values, also explain the importance of the low pass filter]

Similar to the camera parameters, ϵ_x and ϵ_y represent the tilt angles of the beam trajectory relative to the z-axis of the lab system. d_{0x} and d_{0y} are the offsets of the optical axis z_b of the beam from z at the position z_0 of the waist w_0 on z. Combining Equation 56 and Equation 57 let's us directly access the shape of a laser beam from the perspective of a 2D camera.

2.5 Signal demodulation

After the modulated laser beam is recorded, it can be demodulated. Superimposing the electric fields E_c and E_h of two laser beams, we can express the resulting electric field of the recombined beam as

$$
\begin{aligned}
E(x, y, z, t) &= E_c(x, y, z, t) + E_h(x, y, z, t) \\
&= U_c \hat{e}_c \Psi_c(x, y, z) e^{i\omega_c t} + U_r \hat{e}_r \Psi_r(x, y, z) e^{i\omega_r t} \\
&= \overline{U}_c(x, y, z) \hat{e}_c \cdot e^{i(\omega_c t - \Phi_c)} + \overline{U}_r(x, y, z) \hat{e}_r \cdot e^{i(\omega_r t - \Phi_r)}
\end{aligned} \tag{58}
$$

[8].

The indices are c for carrier, which denotes the test beam, and r for reference, which denotes the reference beam. Equation 58 includes the carrier frequency ω_c and the frequency of the reference beam $\omega_r = \omega_c + \omega_h$, where ω_h is the linear offset from ω_c for heterodyne detection and the beat frequency of the combined signal. With Equation 18 and the identity $\cos(x) = \exp(ix) + \exp(-ix)$ we can calculate the intensity recorded by a photodiode if $\hat{e}_c \hat{e}_r = 1$:

$$
\begin{aligned}
I(t) &= \overline{U}_c^2 + \overline{U}_r^2 + \overline{U}_c\overline{U}_r \left(e^{i((\omega_c-\omega_r)t-\delta\Phi)} + e^{-i((\omega_c-\omega_r)t-\delta\Phi)}\right) \\
&= \overline{U}_c^2 + \overline{U}_r^2 + \overline{U}_c\overline{U}_r \cos(\omega_h t - \delta\Phi)
\end{aligned}
\tag{59}
$$

with $\delta\Phi = \Phi_c - \Phi_r$. Equation 59 includes a DC offset and a AC term that oscillates with time t. To demodulate the recorded signal, we can split the signal into DC and AC terms and use an additional oscillatory component

$$
V_h(t) = e^{-i(\omega_h t)} = \cos(\omega_h t) - i\sin(\omega_h t) \tag{60}
$$

that is multiplied to the AC component of Equation 59 to obtain the complex mixing signal

$$
\begin{aligned}
Z(t) &= \overline{U}_c\overline{U}_r \cos(\omega_h t - \delta\Phi)\cos(\omega_h t) \\
&= \overline{U}_c\overline{U}_r (e^{-i(2\omega_h t-\delta\Phi)} + e^{i(\delta\Phi)}) \\
&= \overline{U}_c\overline{U}_r (\cos(2\omega_h t - \delta\Phi) - i\sin(2\omega_h t - \delta\Phi) \\
&+ \overline{U}_c\overline{U}_r (\cos(\delta\Phi) + i\sin(\delta\Phi).
\end{aligned}
\tag{61}
$$

The signal in Equation 61 now includes an oscillating term at $2\omega_h$ and a term that only contains the geometric phase offset $\delta\Phi$ between test and reference beam. We can apply an effective low-pass filter, by summing up a multitude of data samples over time which average out oscillating term. The complex mixing sginal then becomes

$$
\begin{aligned}
Z(t) &= \overline{U}_c\overline{U}_r e^{i(\delta\Phi)} \\
&= \overline{U}_c\overline{U}_r (\cos(\delta\Phi) + i\sin(\delta\Phi).
\end{aligned}
\tag{62}
$$

Since 62 is complex, we can separate it into its real and imaginary parts:

$$
I_p = \Re(Z(t)) = \overline{U}_c\overline{U}_r \cos(\delta\Phi), \tag{63}
$$

$$
Q_p = \Im(Z(t)) = \overline{U}_c\overline{U}_r \sin(\delta\Phi). \tag{64}
$$

In the complex plane, Equation 63 and Equation 64 describe the part of the signal I_p, where the test beam is in-phase with the reference signal, and the part Q_p where it's 90° out of phase. Amplitude $\overline{U_c U_r}$ and phase Φ can then be reconstructed by:

$$
\overline{U}_c\overline{U}_r = \sqrt{I_p^2 + Q_p^2}, \tag{65}
$$

$$
\delta\Phi = \arctan\left(\frac{Q_p}{I_p}\right). \tag{66}
$$

In our case we are using a test beam that includes the carrier signal, but also two sideband signals created by the EOM with $\omega_s = \omega_c \pm \omega_{\mathrm{EOM}}$. The demodulation is essentially the same. By adjusting the demodulation frequency ω_h to $\omega_h - \omega_{\mathrm{EOM}}$ or $\omega_h + \omega_{\mathrm{EOM}}$, which are the beat frequencies created by the upper and lower sidebands in combination with the heterodyne frequency, phase and amplitude information on all three wavefronts in the test beam can be obtained [8],[36].

3 Laser Setup

The laser setup constructed in this work is inspired by a design by K. Agatsuma et. al. at Nikhef [8] and is illustrated in Figure 11. The laser in use is a CoSF-D-ER-B-LP Narrow Linewidth Single Frequency Fiber Laser that produces linearly polarized, single mode radiation at a wavelength of 1550.141 nm with narrow spectral bandwidth. The output power is adjustable between 10 mW and 200 mW [31]. The parameters of this specific laser were tested by Connet Laser Systems and are listed in more intricate detail in Table 2 with the test conditions in Table 1.

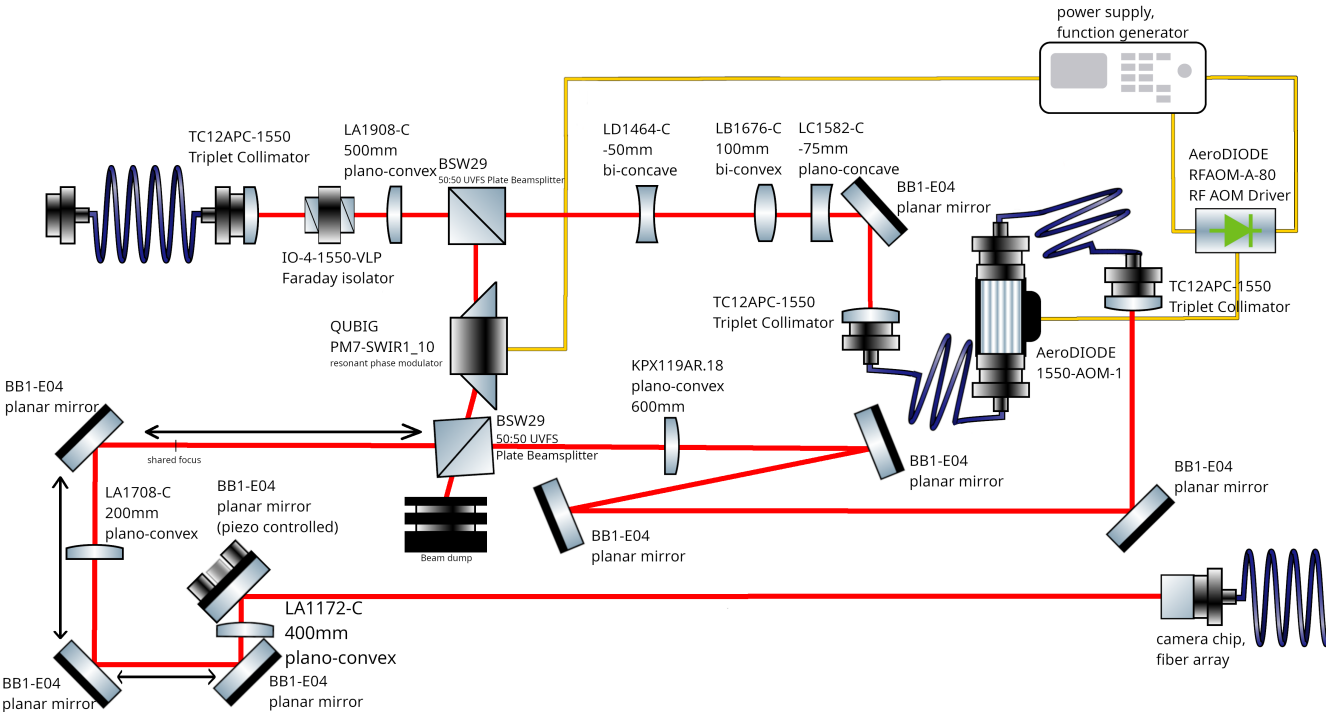

Figure 11: Sketch of optical setup for the ET phase camera. All components used are listed in Table 5. Simplified explanation: Laser beam is split at a beamsplitter (BSW29) into two sections. The section propagating to right is coupled into the AOM (AeroDIODE 1550-AOM-1) and the section going downwards into the EOM (QUBIG PM7-SWIR1_10). Both are recombined at a second beamsplitter (BSW29) and subsequently captured by a 2D camera chip with 64 pixels that connect to individual fibers and photodiodes. A more detailed explanation can be found in Section 3.2 and Section 3.3. Illustration created with components from [25].

The radiation produced by the laser itself is fed into a built-in output pigtail fiber [37] with a length of 50 cm [38]. To not have to frequently touch and potentially damage it, it is connected to a ADAFCPMB4 Dual L-Bracket Mating Sleeve by Thorlabs that is connected to another fiber, specifically a 1 m long Thorlabs P3-1550PM-FC-1 - PM Patch Cable [39]. The end of this fiber is then connected to a Thorlabs TC12APC-1550 Triplet collimator with a focal length of $f = 12.56$ mm, that can be seen in the top left of Figure 11 and marks the effective starting point of the setup on the optical table.

3.1 Technical issues

This section serves to address several technical issues that arose during design and construction of the optical setup, and the compromises resulting from them.

3.1.1 Focal shift of the Faraday isolator

The second optical component in the optical setup show in in Figure 11, is a IO-4-1550-VLP - Free-Space Isolator [40]. This element's purpose is to prevent reflection back into the laser itself which might cause lasing instabilities [41]. It was discovered that propagation through this Faraday isolator results in a small change in waist size w_0 and location z_0 of the focus created by the following lens LA1908-C. According to Thorlabs support, it is not possible to calculate exactly how the isolator affects the shape of the transmitted beam. Hence all simulations in the beam paths behind this component had to be based around measurements of the shifted focus. This is the first focus of the EOM beam.

3.1.2 Systematic errors of the beam profiler

For measuring beam sizes and trajectories in the optical setup, we use a WinCamD-LCM-TEL, a beam profiler by DataRay [42]. This tool proved to possess issues that often make it difficult or impossible to obtain accurate measurements regarding beam size. These issues were discussed with DataRay support. Unfortunately, WinCamD-LCM has some problems measuring light at 1.5 µm accurately in some cases. The camera cannot measure infrared light directly and instead uses phosphor coating to convert the infrared to visible light. Due to the grain size of the detector's coating ($\approx 25\,\mu m$), which is used to create a response at 1550 nm, measurements with small beams sizes are inaccurate. It is thus recommended to only use the camera for beam sizes of $w > 250\,\mu m$. The gamma correction, combined with the point spread function of the phosphor also means that ISO11146 compliant algorithms are not usable for determining beam diameter accurately. Instead, the clip width method has to be used. These factors result in measurements with high error as compared to measurements that can be done with beam profilers specifically designed for 1550 nm. This issue results in inaccurate beam quality measurements as detailed in Section 3.1.3 and makes it difficult to measure exact beam size and location of laser foci.
A second, more severe systematical error was discovered that unveiled that the beam sizes measured with WinCamD-LCM-TEL are dependent on the power of the laser light. Later sections contain plots that show the radial evolution of the laser beam through the optical setup (see Figure 14 and Figure 21). Next to simulations, they show the result of beam size measurements with the beam profiler that were conducted with 10 mW, 50 mW, 100 mW, 150 mW, and 200 mW laser output power for each measurement point. Most of the time during these measurements, $2w \sim P$ applies, but in a few instances, the spot size captured by the beam profiler didn't change with increasing P, or even decreased. Figure 12 shows a plot of the percentage change in w over the percentage change in P for every measurement point with corrected power values, since all optical elements in the beam path attenuate the light (see Figure 59 and Figure 60). Thus the actual power reaching the beam profiler is different at individual measurement points. It's difficult to draw a qualitative conclusion from points in Figure 12 other than that radius increases with power. While it seems like it could correlate to a linear curve, the shape is too chaotic to make this conclusion.

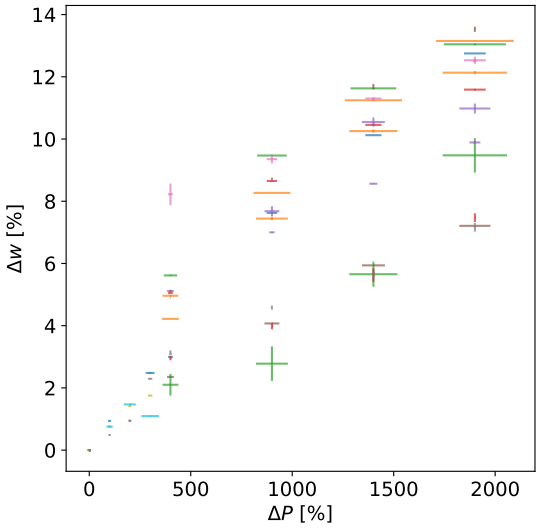

Figure 12: Percentual radial change over percentual power change for all measurement points with standard derivations in ΔP-direction coming from uncertainties in power measurements (see Figure 59 and Figure 60), and standard derivations in Δw-direction from the measurements regarding beam profiler power dependence itself.

The first possible potential source for this issue could be thermal lensing in the Neutral Density (ND) filters. The WinCamD-LCM-TEL includes several magnetically mountable ND filters that attenuate the laser light for signal processing. According to the WinCamD User Manual, the refractive index of the ND filters is slightly temperature dependent. Thus it is advised to not exceed an intensity of $1\,\mathrm{W/cm^2}$ i.e. transfer enough energy from the laser to the ND filter glass to cause a change in temperature [42]. While in some of the measurements the intensity is higher than the recommended threshold, other measurements that are in the order of down to 0.1 times the threshold also exhibit the change in measured spot size. A recommendation from DataRay support to try filters with lower ND values and thus lower energy absorption not only did not mitigate the problem but yielded the opposite of what was expected. The ND filter with all measurements in this work were conducted, has a attenuation factor of 10^4. At the location of the first measurement point from the left in Figure 14 and Figure 61, the beam diameter with this exact filter is $d \approx 2330\,\mu\mathrm{m}$. At the same location, using a filter with an attenuation factor of 10 yields a beam diameter of $d \approx 2530\,\mu\mathrm{m}$. Using no ND filter at all results in an even larger size with $d \approx 2750\,\mu\mathrm{m}$. Hence negative thermal lensing can be excluded as at least a main contributor of this effect. Placing the beam profiler directly behind the laser output fiber also yields a power dependent beam size in measurements. The elements between laser and optical table, namely the ADAFCPMB4 Dual L-Bracket Mating Sleeve, P3-1550PM-FC-1 - PM Patch Cable, and TC12APC-1550 Triplet collimator can thus be exluded as possible error sources.
In coordination with DataRay support, this effect could not be explained. Thus the measurements points themselves carry an unreliability, especially in magnitude. Their resulting curve however should be accurate, but it should be noted that even that includes some uncertainty, because of the aforementioned thermal lensing effect that may be occuring in some of the settings with higher irradiance (larger measured beam size). The optical setup was designed at and is operated at minimum laser power (10 mW). In case that the origin of this systematic error does not lie with the beam profiler after all and is the result of improper functionality in the Connet CoSF-D, then the lower ends of the y-error bars in Figure 14, and Figure 21 are slightly more likely to be correct.

3.1.3 Laser beam quality

A laser beam's quality affects its Rayleigh length and thus its phase front and beam radius. Hence it is a important factor, for calculations of the effects of optical elements on the beam and the shape of its intensity and phase profile. The quality factor of the CoSF-D-ER-B-LP Narrow Linewidth Single Frequency Fiber Laser according to Connets test report is $M^2 < 1.1$. In an attempt to verify this, a beam quality measurement was conducted with the WinCamD-LCM-TEL. For this, the initially collimated beam is focused with a lens. The beam profiler is then set to different positions along the optical axis both in front and behind the focus, where it records the size of the beam. The WinCam software then applies a fit (Equation 13) to the recorded data to determine the quality factor M^2 [42]. The result of one of these measurements is shown in Figure 13.

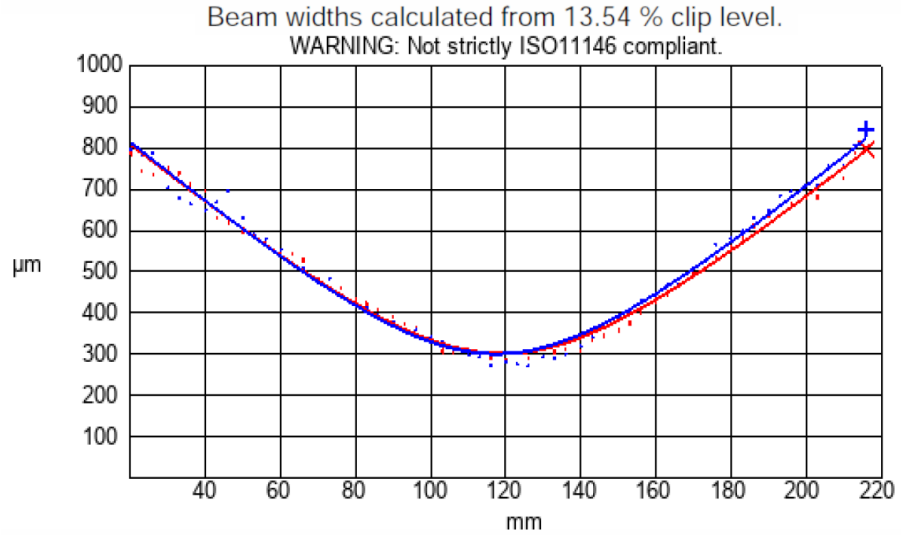

	X	Y	Units
M^2	1.16+/-0.12	1.18+/-0.12	N/A

Figure 13: Result of one of the M^2 measurements taken with the WinCamD-LCM-TEL. The camera is moved across the optical axis (x-axis in the plot) with the beam being captured at specific locations ($w(z)$ is the y-axis in the plot). The resulting curve's divergence in x- and y-direction in the lab system (blue and red) is then compared to the divergence of an ideal Gaussian beam ($M^2 = 1$) with the same waist size w_0. $M^2 = 1$ means minimal divergence.

Due to the first problem described in Section 3.1.2, the result is measurements with high error as illustrated in Figure 13. The fit function by the DataRay software does not correlate well with the data points around the waist. With quality factors of $M^2 = 1.16 \pm 0.12$ in x and $M^2 = 1.18 \pm 0.12$ in y-direction, it was not possible to obtain a result more accurate than the one given in the Test Report by Connet with $M^2 < 1.1$ (see Table 2).

3.1.4 General statistical errors

The systematic error of the beam profiler explained in Section 3.1.2 was discovered after the optical setup was already constructed. As such it was found that the beam profiler measurements of the beam radius w did not correlate well with simulations, as can be seen in Figure 61 and Figure 62, which show the simulations for beam radius $w(z)$ across the entire setup according to parameters that were initially believed to be correct. Contrary to initial assumption, the collimator specs that

were used to design this initial setup, specifically regarding the theoretical waist diameter and its location are only valid when using the exact same fiber that Thorlabs used to determine these values, namely a SMF-28e+ [43]. The two fibers used together with output collimators in the laser setup however are a Thorlabs P3-1550PM-FC-1 - PM Patch Cable, and a PM1550 fiber that is built into the AOM. The P3-1550PM-FC-1 has a *MFD* of $(10.1 \pm 0.4)\,\mu m$ at $\lambda = 1550\,nm$ [39], leading to a waist size of $w_0 = (1290 \pm 80)\,\mu m$ at a distance of $z_0 = 12.56)\,mm$ from the first collimator, instead of $w_0 = (1.135 \pm 0.005)\,\mu m$ with $z_0 = -10.2 \pm 1.0)\,mm$. The specs of the AOM fiber were provided by AeroDIODE support and are listed in Table 4. With $MFD = (10.5 \pm 0.5)\,\mu m$, this leads to an output waist of $w_0 = (1240 \pm 80)\,\mu m$ at $z_0 = (-1.527 \pm 0.007)\,m$ instead of $w_0 = 1.135 \pm 0.005)\,\mu m$ at $z_0 = (-1.550 \pm 0.007)\,m$. These values were calculated with the method described in Section 2.4.6. The new calculations also take the quality factor $M^2 = (1.05 \pm 0.05)$ into account which was neglected before.
With the knowledge gained from the issues discovered in Section 3.1.2 regarding the systematic error of the beam profiler, a new more accurate measurement of the size and position of the first EOM beam focus, that is used as the baseline for many of the simulations, as already mentioned in Section 3.1.1, was conducted. It turned out that the focus is not located at $z = (0.1980 \pm 0.0020)\,m$, but at $z = (0.210 \pm 0.004)\,m$, with a beam radius of $w_0 = (249 \pm 3)\,\mu m$ instead of $w_0 = (258 \pm 3)\,\mu m$.
The position of the lens KPX119AR.18 was also incorrect. A new measurement of optical element positions revealed that it is located at $z = (-0.4470 \pm 0.0015)\,m$, not at $z = (-0.4270 \pm 0.0028)$. The reason for this discrepancy could be that the lens was at one point put onto a rail in order to make it movable for some of the phase measurements below.

3.1.5 Inaccuracies in technical specs

Remedying and consolidating the errors and systematic errors from the Sections above led to the simulation of the beam radius $w(z)$ shown in Figure 14 and Figure 63 in the appendix. The adjusted simulation for the AOM beam still does not fit to the measurement points, even less than in Figure 62. There is also a large offset between $z_{0,\mathrm{AOM}}$ and $z_{0,\mathrm{EOM}}$ which can't be correct since the overlap of the two beams was specifically aligned by hand. Hence this simulation must also be false. Taking a look at the far left side in Figure 63, we can see that the measured values show a stronger divergence and smaller theoretical focus, that by this shape, must be located at $z_0 < z_{\mathrm{collimator}}$. By manually adjusting the theoretical parameters of the beam produced by the AOM collimator, a shape could be found that aligns well with the measurements along the whole beam path with $w_0 = (1100 \pm 50)\,\mu m$ and $z_0 = (-2.027 \pm 0.007)\,m$. This is the best setting that could be found manually. The simulation with these parameters can be seen in Figure 21 and provides the parameters that the phase simulations in later sections are based on.

3.2 Evolution of the laser beam through the optical setup

As the laser setup has two splitting beam paths that recombine back into one, it is useful to characterize it with two separate coordinate systems. The first coordinate system (CS 1) is for describing the beam paths in front of EOM and AOM and the second coordinate system (CS 2) for the paths behind them. As such, CS 1 places the location of the initial laser output collimator as $z = 0$, while CS 2 is centered around the location of the second BS in Figure 11 as $z = 0$. Evolution of the laser power P through CS 1 and CS 2 with a laser output power of 10 mW are shown in Figure 59 and Figure 60.

3.2.1 First coordinate system

As seen in Figure 11, the initial beam is first fed into the IO-4-1550-VLP - Free-Space Isolator. At 1550 nm this component allows for a maximum transmission of 95 % of the laser light with an isolation

of $38-42$ dB with a maximum beam diameter of $2w_{\max} = 3.6$ mm. To achieve maximum transmission, the TC12APC-1550 Triplet collimator is rotated to produce laser light polarized in a 45° angle. The input polarizer plate of the isolator is also set to 45° meaning that ideally, all of the incoming radiation is transmitted. The internal Faraday rotator then rotates the polarization by another 45° through the usage of a magnetic field, leading to the subsequent laser light being linearly polarized horizontally, i.e. parallel to the optical table's surface [41]. From before to behind the Faraday isolator, P decreases from (9.530 ± 0.028) mW to (9.20 ± 0.10) mW, which equates to a transmission of (96.5 ± 1.1) %, slightly above the official maximum value. Next, at the position $z = (0.110 \pm 0.004)$ m, with is a Thorlabs LA1908-C plano-convex lens with a focal length of $f = 500$ mm [44] with the primary function to focus the beam to avoid clipping at the EOM further down the beam path. To limit optical aberrations, the spherical side is facing the collimator. As statistical errors, a tilt $\theta_1 = (0.00 \pm 0.10)°$ and displacement $x_1 = (0 \pm 1)$ mm were assumed. The statistical error of location parameters is based on positional measurements.

The beam is then split at $z = (0.277 \pm 0.004)$ m by the first beamsplitter in the setup, a Thorlabs BSW29, into the reference and test beam sections. These are the reference and test beam which we will denote as AOM and EOM beam. The BS has a thickness of (5.0 ± 0.4) mm, where instead of both surfaces being perfectly parallel, one is tilted by an angle of 30 arcmin in order to prevent ghosting, i.e. the overlap of backscattered of light. The BS is optimized to achieve a near 50:50 split in power for unpolarized light. For polarized light at 1550 nm, the power split is around 65:35 [45]. The total beam in front of the BS has a power of (9.13 ± 0.08) mW and the split AOM and EOM beams (6.020 ± 0.0028) mW and (3.040 ± 0.014) mW. The actual power split is thus (65.9 ± 0.07):(33.30 ± 0.33) which is accurate.

Following BS 1, the EOM beam travels through the PM7-SWIR1_10 by QUBIG, where sidebands at ± 10 MHz are created.

The AOM beam propagates through a lens system before arriving at another TC12APC-1550 Triplet Collimator at $z = (0.973 \pm 0.01)$ m that is attached to a P3-1550PM-FC-1 - PM Patch Cable connecting to another ADAFCPMB4 Dual L-Bracket Mating Sleeve that then connects to the fiber-coupled 1550-AOM-1 by AeoroDIODE shifts the frequency of the laser light by $+80$ MHz. The purpose of the lens system is mode-matching, i.e. to equalize the input beam as close as possible to the beam parameters produced by the collimator mentioned above, as to maximize power transmittance through the optical fiber [46]. The lens system is comprised of three lenses, a Thorlabs LD1464-C [47] at $z = (0.517 \pm 0.006)$ m with $f = -50$ mm, a LB1676-C [48] at $z = (0.723 \pm 0.007)$ m with $f = 100$ mm, and a LC1582-C at $z = (0.810 \pm 0.008)$ m with $f = -75$ mm. With this configuration, at minimum laser power (10 mW), measurements show that the power decreases from (5.850 ± 0.028) mW in front of the collimator to (2.640 ± 0.028) mW behind the fiber, which equates to a power transmittance of (45.1 ± 0.05) %. The AOM itself has an additional insertion loss of 1.7 dB according to its factory test report (see Table 3), thus the power behind it should be (1.785 ± 0.014) mW. The measured power behind the AOM output collimator is (1.885 ± 0.005) mW which is slightly above the theoretical value. The result was deemed sufficient for later recombination with the EOM beam, because both beams possess power with similar magnitude.

The evolution of the beam radius $w(z)$ through the first coordinate system with can be seen Figure 14.

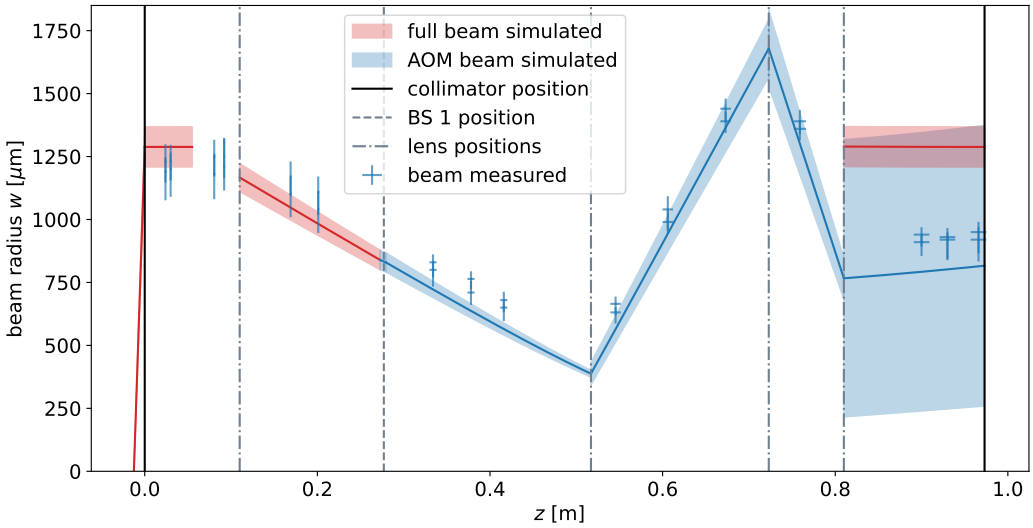

Figure 14: Beam radius $w(z)$ in the first coordinate system after adjusting for statitical errors. The measured values contain the mean and range (lowest to highest measured value) of both major and minor beam axes because of the unresolved systematic error with the beam profiler (see Section 3.1.2). This plot does not contain the EOM beam, which has the same shape past the BS as the AOM beam has up until the subsequent lens in it's path. The gap on the left side in the full beam simulation represents the space between the O-4-1550-VLP - Free-Space Isolator and the first lens, where the radius can not be simulated. The shape of the segment between this lens and the BS is based on measurements of this beam segment's waist as described in Section 3.1.1. The red segment on the right represents the shape that the beam would need to have for perfect mode matching, which is the exact same shape as produced by the output collimator on the right.

3.2.2 Second coordinate system

CS 2 is centered around the position of BS 2 at $z = 0$. The AOM output collimator at the end of its output fiber, another TC12APC-1550 Triplet Collimator, is located at $z = (-1.540 \pm 0.007)\,\mathrm{m}$. A KPX119AR.18 plano-convex lens by Newport [49] with a focal length of $f = 600\,\mathrm{mm}$ is positioned at $z = (-0.4470 \pm 0.0015)\,\mathrm{m}$ in order to match the AOM beam to the EOM beam as best as possible. This position was experimentally set, the simulated effects of the position of this lens are shown in Figure 15. In the second coordinate system, this lens is referred to as lens 1. Since the AOM beam is large and well collimated, i.e. it's radius $w(z)$ and radius of curvature $R(z)$ do not change drastically over z, the position of lens 1 only has marginal effects on the resulting new waist, and the waist position is directly proportional to it: $z_0 \propto z_{\mathrm{lens1}}$. This means that statistical errors regarding the lens position and the AOM beam parameters only have marginal impacts, which is visualized in Figure 15, which shows the effect of the positioning of lens 1 on the resulting waist radius w_0 and its position z_0 of the AOM beam compared to the EOM beam focus.

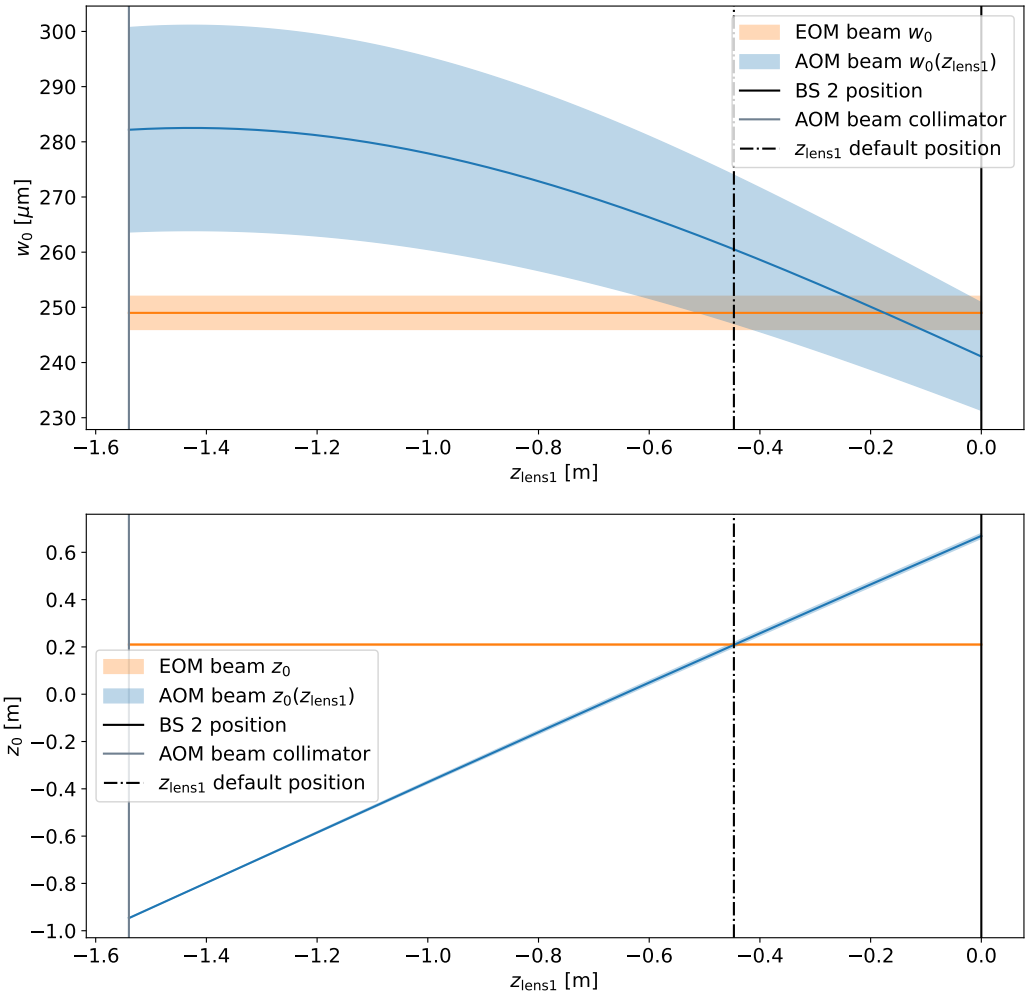

Figure 15: Waist w_0 (top) and waist position z_0 (bottom) of the AOM beam created by lens 1 depending on its position on the optical axis z. Initial parameters are from the simulation depicted in Figure 21. The best position indicates where EOM and AOM beam perfectly overlap in both plots. The EOM beam parameters in these plots are static, as lens 1 is located in the AOM beam path. Note that the initial design provided an even overlap in w_0 but a worse overlap in z_0 (see Figure 64).

As shown in Figure 11, both beam paths are then recombined at the position of BS 2, which is set to $z = (0 \pm 0.005)\,\text{m}$. A shared focus is created with $z_{0,\text{AOM}} = (0.210 \pm 0.010)\,\text{m}$, $w_{0,\text{AOM}} = (261 \pm 13)\,\mu\text{m}$, and $z_{0,\text{EOM}} = (0.210 \pm 0.004)\,\text{m}$, $w_{0,\text{EOM}} = (249 \pm 3)\,\mu\text{m}$. The beamsplitter changes the laser powers P of the two beams from $(2.97 \pm 0.01)\,\text{mW}$ to $(0.93 \pm 0.01)\,\text{mW}$ for the EOM beam and from $(1.82 \pm 0.01)\,\text{mW}$ to $(1.27 \pm 0.08)\,\text{mW}$ (see Figure 60). Note that the accuracy of the power meter is limited to two decimal places. The reason why the EOM beam power decreases this drastically, is that most of the light is transmitted by BS 2, while the beam that is recombined with the AOM beam, is the reflected part of the initial EOM beam. The fact that this narrows the gap between the two laser beams' power is beneficial because it provides better mode-matching between

the beams. Following the second beamsplitter are two lenses, a Thorlabs LA1708-C with $f = 200\,\text{mm}$ and LA1172-C with $f = 400\,\text{mm}$. These are denoted as lens 2 and lens 3. While lens 3 is stationary, with $z_{\text{lens3}} = (0.722 \pm 0.066)$, the purpose of lens 2 is to be movable between BS 2 and lens 3. In combination with lens 3, this makes it possible to create a multitude of possible waist sizes in the camera range later on the path and makes it possible to study many types of wavefronts with the phase camera. Note that some areas between BS 2 and lens 3 are occupied with planar mirrors and their post holders. As such, the areas $z = (0.317 \pm 0.004)\,\text{m} \pm 1.5\,\text{cm}$, and $z = (0.622 \pm 0.005)\,\text{m} \pm 1.5\,\text{cm}$ are obstructed and cannot be chosen for lens 2. The same applies for the 1.5 cm directly behind BS 2 and 5 cm in front of lens 3. Simulations of the achievable beam waists and their positions on the optical axis can be seen in Figure 16 and Figure 17 shows a small number of beams and their radii that can be created with different positions of lens 2.

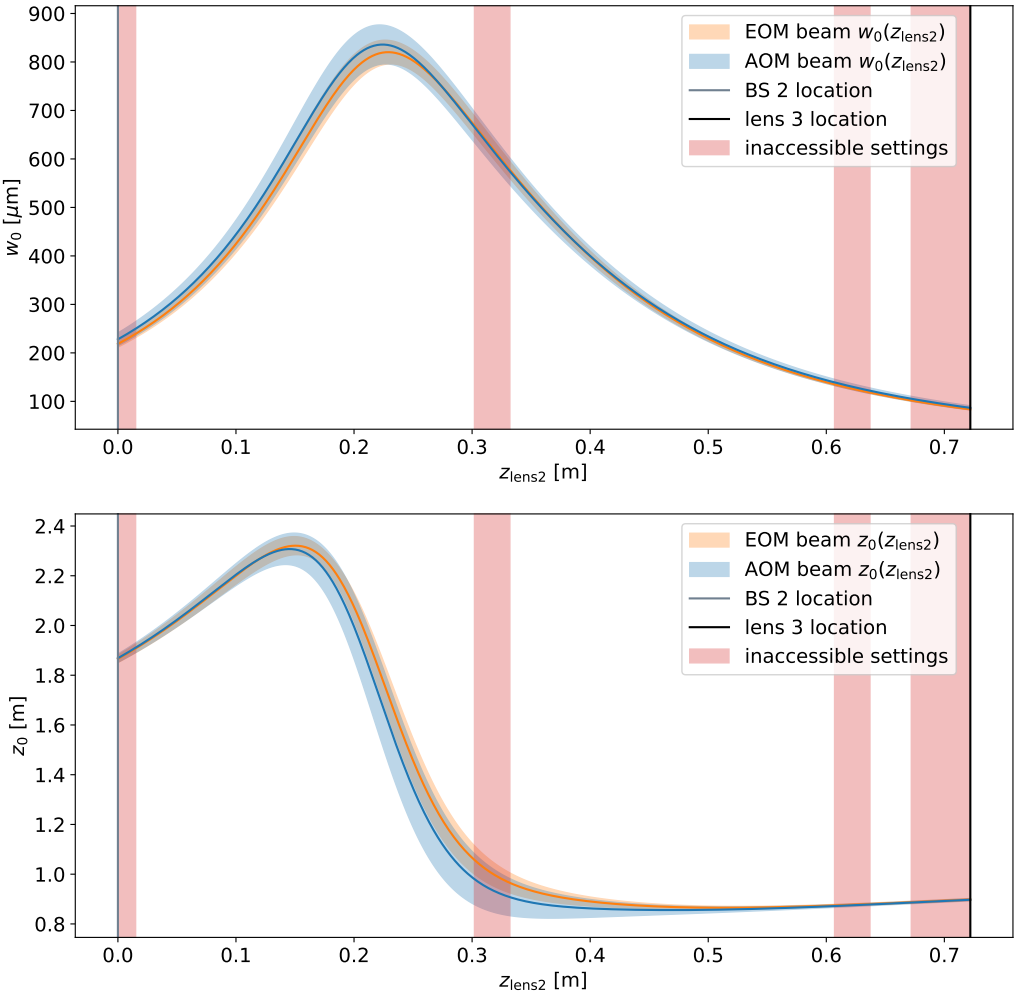

Figure 16: Achievable waist sizes w_0 dependent on the position of lens 2 on the optical axis. Initial parameters are from the simulation depicted in Figure 21. Top: Waist sizes w_0. Bottom: Related waist positions z_0. The areas in this range marked in red are obstructed by the posts of optical elements and can not be chosen as z_{lens2}. These are $z_{\text{BS2}} \pm 1.5\,\text{cm}$, $z_{\text{mirror1}} \pm 1.5\,\text{cm}$, $z_{\text{mirror1}} \pm 1.5\,\text{cm}$, and $z_{\text{lens3}} - 5\,\text{cm}$. Note that the overlap between AOM and EOM beam of the initial design is better (see Figure 65).

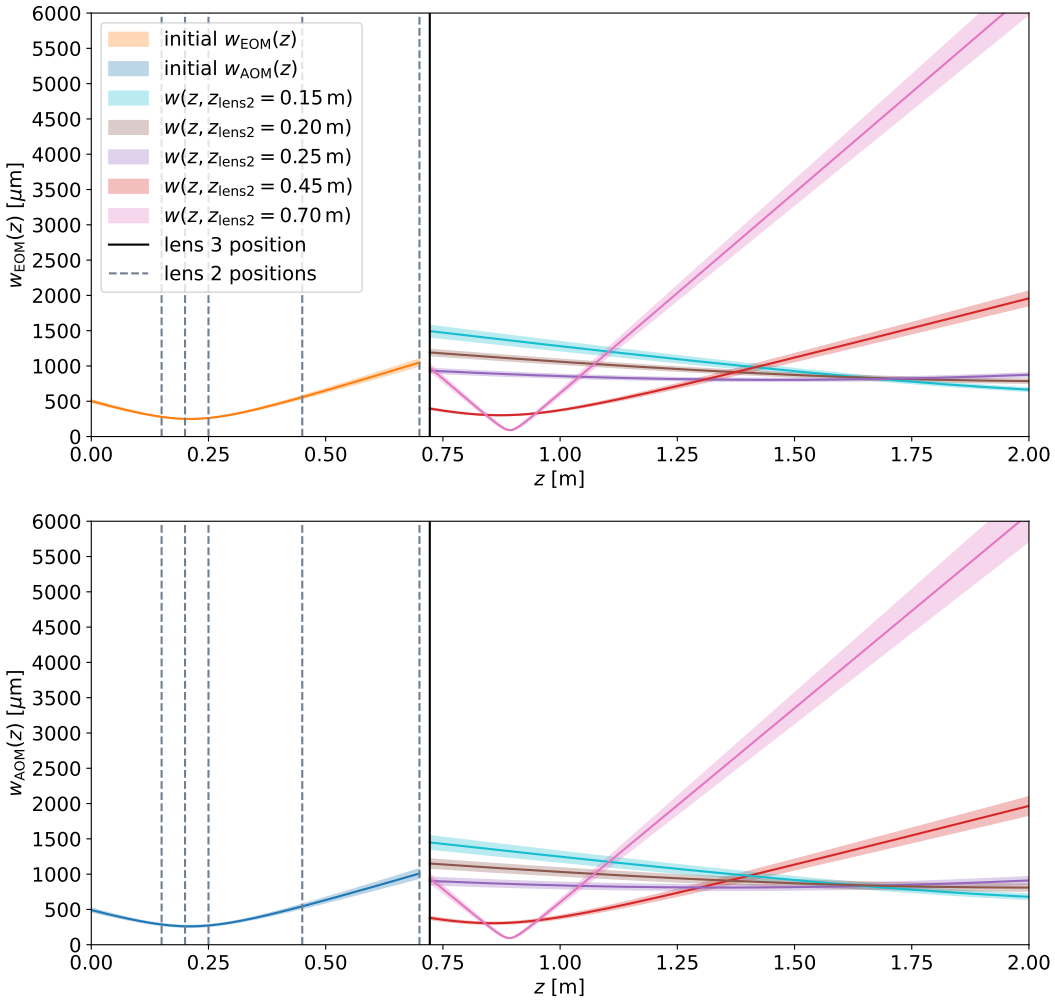

Figure 17: Beam radii in the camera range for five different positions of lens 2. Top: EOM beam. Bottom: AOM beam. In comparison to the initial design (see Figure 66), the std bands are much broader as a consequence of including the quality factor M^2 in the simulations.

As can be seen in Figure 15 and Figure 17, a wide spectrum of beam types can be created with this lens setup ranging from large, well collimated beams with flat wavefronts, to beams with very small foci and large divergence. Though the shapes of the AOM and EOM beams in Figure 17 are similar, it is useful to know the exact difference between the top and bottom plot in Figure 17. Figure 18 shows the difference $w_{\mathrm{AOM}} - w_{\mathrm{EOM}}$ of the two beams for all the different configuration examples.

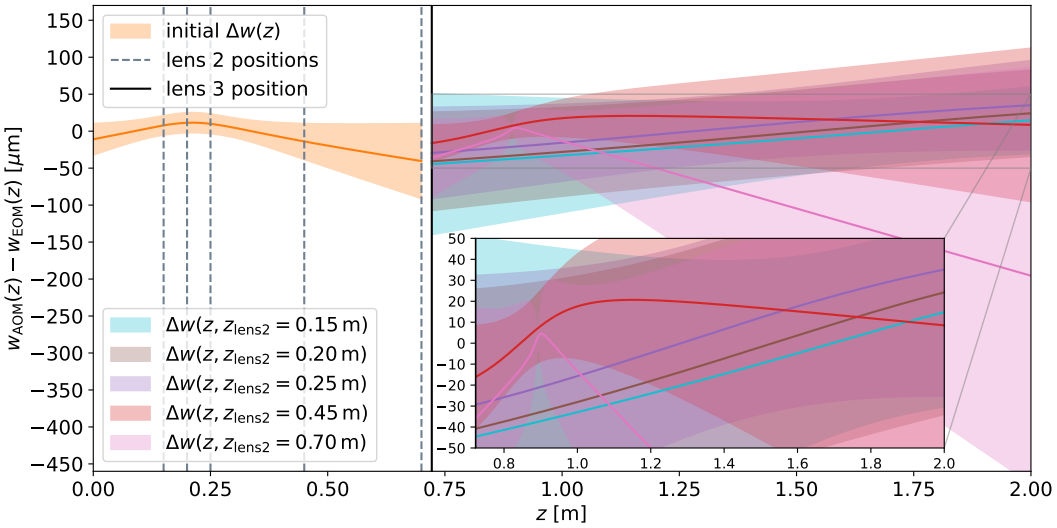

Figure 18: Difference between the beam radius of the AOM and EOM beam in the settings shown in Figure 17.

The most important parameters for phase analysis of a Gaussian beam according to Equation 16 next to the position z_0 of the waist is the inverse of the radius of curvature $R(z)$, the so-called wavefront $1/R(z)$ that is responsible for the transverse, radial phase profile of a laser beam. We can use the example configurations from Figure 17 and construct a similar plot for beam wavefronts. Figure 19 then shows a small sample of wavefront profiles dependent on the position of lens 2.

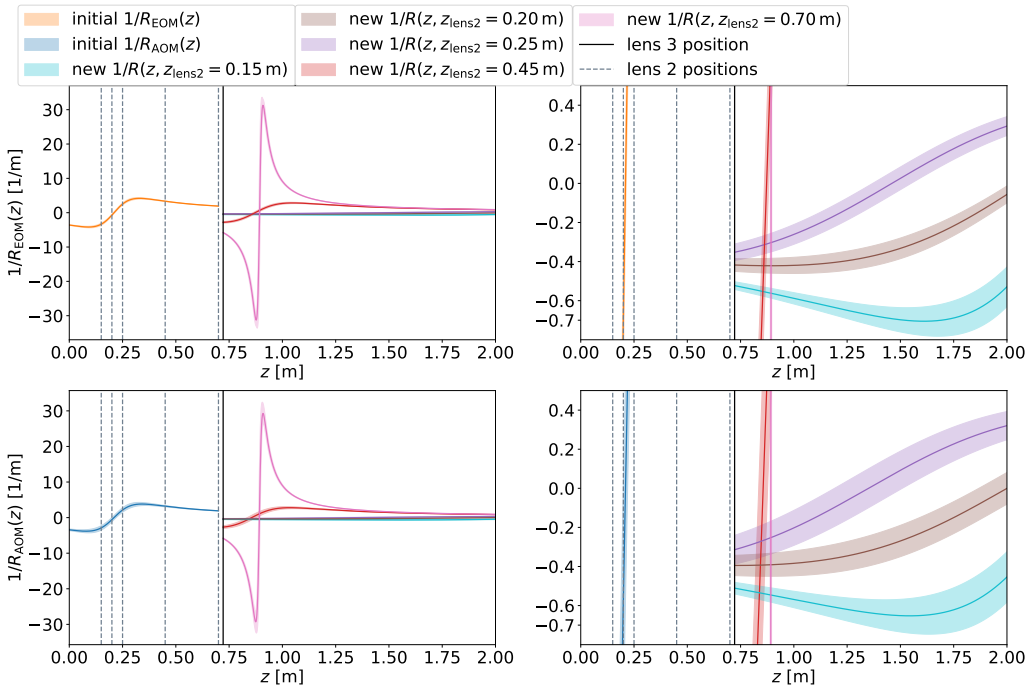

Figure 19: Wavefronts $1/R(z)$ in the camera range for five different positions of lens 2. Top: EOM beam. Bottom: AOM beam. The plots on the right are the same as on the left but zoomed in.

Comparing Figure 19 to Figure 17, we can see that the better collimated a beam is, the closer the wavefront $1/R(z)$ remains to 0 away from the waist. In contrast, the heavily curved example for $z_{\text{lens2}} = 0.70\,\text{m}$, rapidly expands to a peak of much higher magnitude that is located at the distance of of $z = z_0 \pm z_R$, after which the wavefront curvature starts to decrease again as the beam has reached its far-field region. Similarly to Figure 18 which shows the difference between the AOM and EOM beam samples in Figure 17, it is useful to also display the wavefront difference $1/R_{\text{AOM}} - 1/R_{\text{EOM}}$ for all the settings. This can be seen in Figure 20.

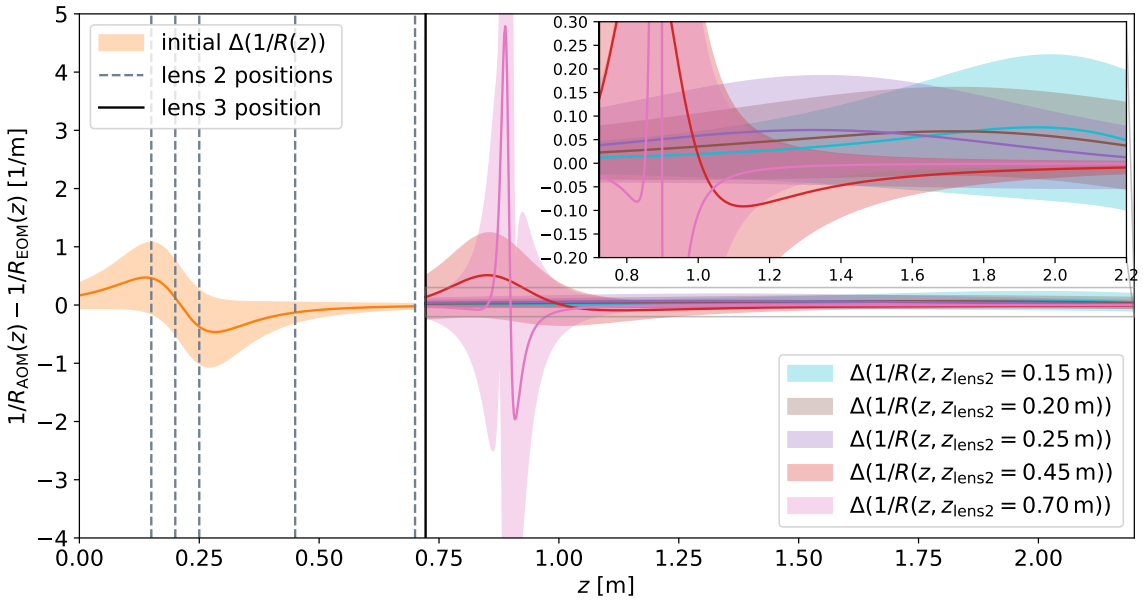

Figure 20: Wavefront difference between the beam radius of the AOM and EOM beam in the settings shown in Figure 19. The pink uncertainty range extends to $-17.4\,\text{m}^{-1}$ and $24.6\,\text{m}^{-1}$.

The first position for lens 2 to conduct phase measurements with is at $z = (0.372 \pm 0.004)\,\text{m}$. This is the basic position chosen for the arbitrary reason to simply construct a working version of the setup. It provides a medium sized beam with $w_{0,\text{AOM}} = (470 \pm 30)\,\mu\text{m}$ and $w_{0,\text{EOM}} = 466 \pm 25\,\mu\text{m}$ that is does neither have a very flat, nor very curved wavefront. The beam radius $w(z)$ across the optical setup for this configuration is shown in Figure 21 and provides a baseline for the many measurements in Section 5, especially for the ones where the effect of changing only the shape of the reference beam is investigated.

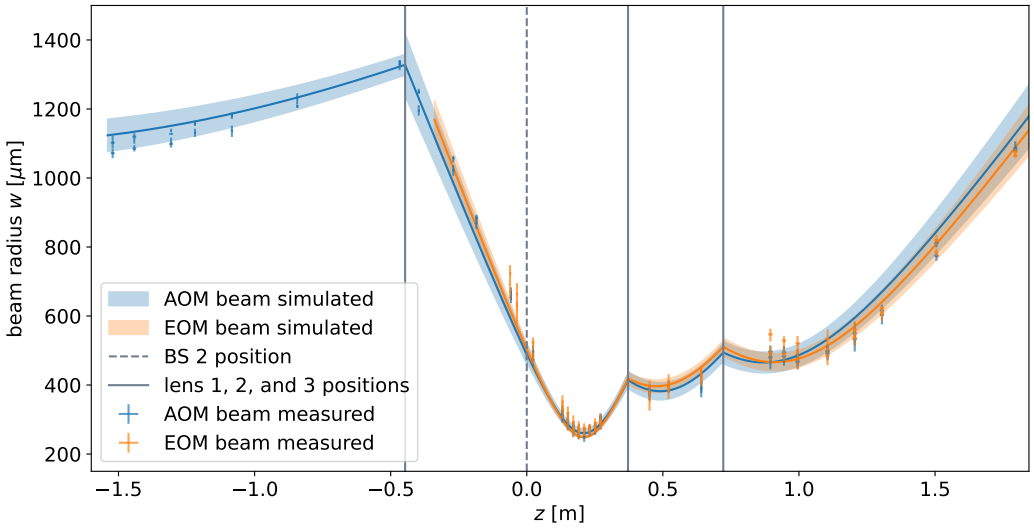

Figure 21: Beam radius $w(z)$ in the second coordinate system after adjusting for statistical errors, and manually finding the best AOM beam parameters for overlap with the measurements. With $z_{\text{lens2}} = (0.372 \pm 0.004)\,\text{m}$. The measured values contain the mean and range (lowest to highest measured value) of both major and minor beam axes because of the unresolved systematic error with the beam profiler (see Section 3.1).

The last optical component in front of the camera range is a Thorlabs BB1-E04 [50] planar mirror at $z = (0.845 \pm 0.008)\,\text{m}$, that is slated to be Piezo-controlled in the future for scanning across the surface of the phase camera. For this work, this feature was not implemented yet. Following this mirror, the 64-pixeled camera with optical fibers coupled to each pixel is located. These fibers connect to individual photodiodes that detect the laser light and convert it to digital signals which are subsequently electronically processed.

3.3 Signal detection and processing

The fiber array used to detect the laser light is shown on the left side in Figure 22. The pixels are arranged in a hexagonal grid with a distance of 0.127 mm between their centers in horizontal direction, and a vertical spacing of 0.108 mm. Thus with 64 pixels in total, the array covers an area of $A = (7.5 \cdot 0.127) \cdot (7 \cdot 0.108)\,\mathrm{mm}^2 = 0.720\,\mathrm{mm}^2$. The right side in Figure 22 shows an example phase reconstruction with the 22 pixels that are currently in use.

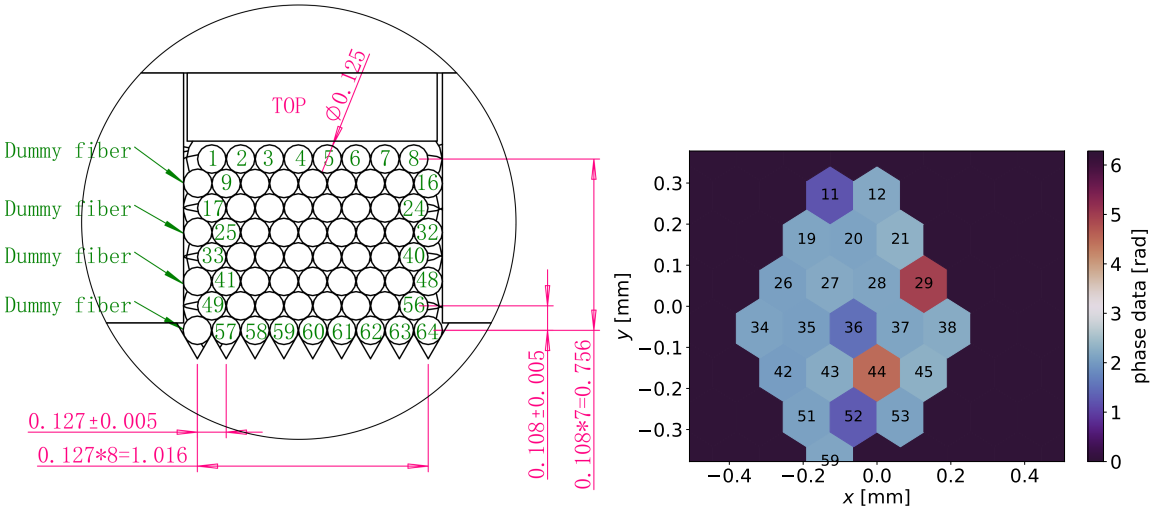

Figure 22: Left: Geometry and pixel numbering of the phase camera fiber array. Right: 22 pixels currently in use.

Each pixel is a PTIU105/125/250AA22BK multi-mode fiber that guides the signal to individual FCI-InGaAs-120-FC photodiodes that are optimized for infrared light. A in-house designed amplifier board then reads the PD current by first using a LMH33440 transimpedance amplifier to amplify and convert the current to voltage, then applying a crossover network that splits the signal into a DC signal used to monitor intensity, and a signal that is to be used for analysis. On the board, the latter signal is also transmitted through a inverting amplifier, that is based on the LMH6629 ultra-low Noise, high-speed Operational Amplifier, and finally through a 250 MHz anti-aliasing filter. Software coordinates and protocols factors like dynamic voltage range or input impedance.
The digitizer is comprised of six 14 bit M4i.4451-x8 4-channel PCIe-digitization cards with 500 MSamples/s, that are internally synchronized with each other. The analog DC signal is converted with a specifically built 24-channel digitizer box based on Arduino Duos. Data is recorded continuously over a set amount of integration time.
After recording, the raw data can then be demodulated into a phase and amplitude signal for each pixel with the I-Q method explained in Section 2.5 with a resolution of at least 0.03 rad with an integration time of 8 μs at the laser output power of 10 mW that translates to AOM and EOM beam powers of $P_{\mathrm{AOM}} = 1.17\,\mathrm{mW}$ and $P_{\mathrm{EOM}} = (0.88 \pm 0.01)\,\mathrm{mW}$ in front of the fiber array. Recording and demodulating is done via a in-house written software framework. Also included is a liveplotter function that continuously displays the intensity recorded by the fiber array, and can be used to center the laser beam onto the array [19].

4 Phase simulations

4.1 Graphical interface

Phase simulations of the AOM and EOM beam are done with a self-written python script that creates a graphical interface that is shown in Figure 70. The code is fed with waist radius w_0 and position z_0 parameters that are obtained with the calculations explained in Section 2.4 tracking the theoretical evolution of the laser beam through the optical setup (see Section 3.2.1 and Section 3.2.2), and offsets d_{0x}, d_{0y} and beam angles ϵ_x, ϵ_y are obtained by performing beam trajectory measurements with a beam profiler in front of the pixel array for all different configurations of the optical setup that are used for phase measurements. Also imported are recorded phase and intensity data for direct comparison with simulations. A more in-depth explanation of the graphical interface can be found in Section A.4.

4.2 Impacts of beam and camera parameters on phase profiles

This section attempts to provide an overview of the scale of the effects of all the parameters w_0, z_0, ϵ_x, ϵ_y, α_x, α_y, $d_{0,x}$, $d_{0,y}$, d_{Cx}, d_{Cy}, and the distance $z - z_0$ between camera and waist position on the resulting phase profile on the camera surface. Due to the three-dimensionality of Gaussian beam phase profiles and the amount of beam parameters, it is difficult to quantify every possible scenario. As such, to limit scale, this overview only uses the calculated mean values of the waist radii of all three carrier beam settings used for measurements in Section 5 as a basis to perform a few demonstrative calculations. These radii are $w_1 = 142\,\mu\text{m}$, $w_2 = 466\,\mu\text{m}$, and $w_3 = 803\,\mu\text{m}$.
First we take a look at the longitudinal phase terms kz and Φ_{Gouy}. These are shown in Figure 23. As can be seen on the left, the linear phase kz changes rapidly between 0 and 2π and is thus not experimentally resolvable in this work. In measurements it provides a phase offset in the 2D images between both beams but does not alter the the shape of the profile due being strictly longitudinal. kz is not dependant on beam size and is thus the same for all three example sizes, provided that $z_{01} = z_{02} = z_{03}$.
The plot on the right of Figure 23 shows the Gouy phase (see Equation 17). As can be seen it inverts at z_0 and changes the most for the beam with the smallest waist and thus biggest divergence. At this wavelength (1550 nm) all three curves tend toward the same value at approximately ± 1.5 rad. The Gouy phase is also purely longitudinal and does not affect the shape of the phase profile on the camera surface.

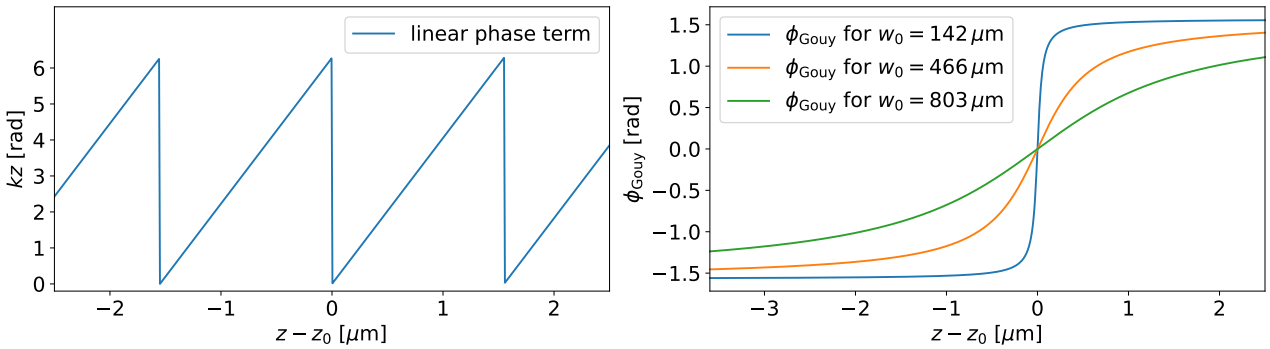

Figure 23: Linear phase term kz (left) and Gouy phase term (right) for all three carrier waist sizes (see Section 5).

Next we take a look at the transversal shape of the phase profile, i.e. the phase from the perspective of the fiber array. The left side of Figure 24 shows a plot of the radially symmetric term $\Phi_{\text{rad}} = kr^2/(2R(z))$ in Equation 16 on one of the camera axes with any offsets removed: $\Phi_{\text{trans}} = \Phi - kz +$

$\Phi_{\text{Gouy}} = \Phi_{\text{rad}}$. To illustrate the effect of the distance from z_0 two positions are shown, $z - z_0 = 0.001\,\text{m}$ (dotted line) and $z - z_0 = 0.01\,\text{m}$ (dashed line). As can be seen, the phase of the beam with the smallest waist increases with much higher magnitude than the other two (≈ 100 to orange, ≈ 1000 to green). The right side of Figure 24 shows the difference $\Phi_{\text{max}} - \Phi_{\text{min}}$ between the highest and the lowest phase value on the 2D surface of the camera dependent on $z - z_0$. As seen, the blue curve quickly maxes out, reaching values from 0 to 2π around the location $z_R - z_0$, where the beam's wavefront $1/R(z)$ has a maximum (see Figure 19 for example). The other two curves display a much smaller range. While a maximum can still be spotted in the orange curve, the beam corresponding to the green curve has a Rayleigh length that is longer than the displayed $z - z_0$ range.

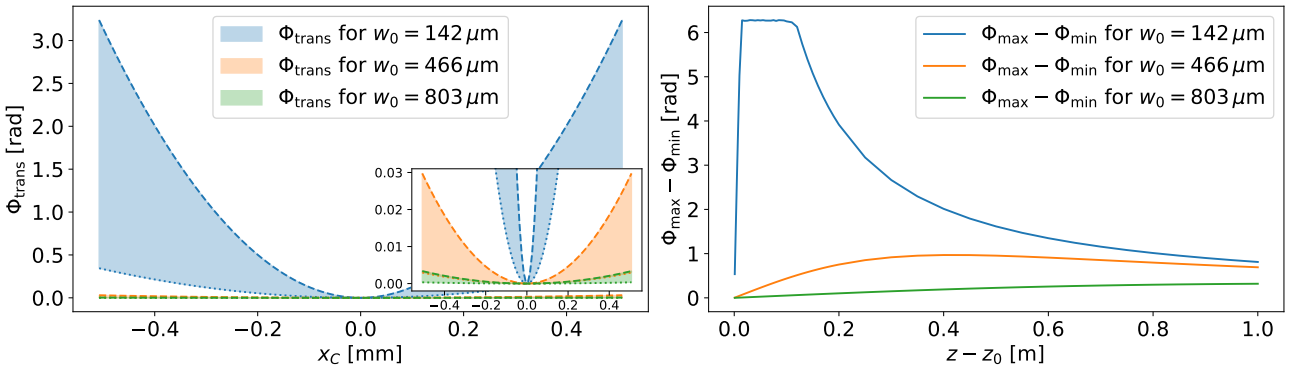

Figure 24: Left: Transverse phase term without any offsets: $\Phi_{\text{trans}} = \Phi_{\text{rad}}$ for $z - z_0 = 0.001\,\text{m}$ (dotted line) and $z - z_0 = 0.01\,\text{m}$ (dashed line) for all three carrier waist sizes (see Section 5). Right: Corresponding phase range on the camera plane.

Linear offsets on x_C and y_C do not change the recorded shape but may displace them from the surface center as shown in Figure 25. This means that the phase range on the camera increases, but the overall shape of the phase profile remains the same.

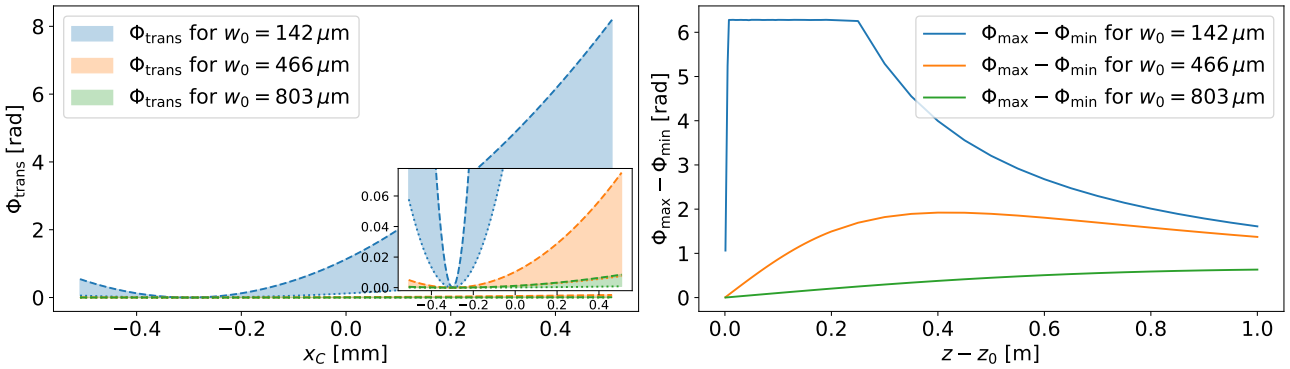

Figure 25: Left: Transverse phase term $\Phi_{\text{trans}} = \Phi_{\text{rad}}$ without any (phase) offsets, and $d_{Cx} = 0.3\,\text{mm}$ for $z - z_0 = 0.001\,\text{m}$ (dotted line) and $z - z_0 = 0.01\,\text{m}$ (dashed line) for all three carrier waist sizes (see Section 5). Right: Corresponding phase range on the camera plane.

Once we take tilt angles $\epsilon_{x,y}$ and $\alpha_{x,y}$ introduced with the 2D camera coordinate system parametrization (see Section 2.4.7) into account, then the transversal phase profile of a laser beam is not only comprised of the radial phase term plus offset anymore. The presence of tilt angles between beam and camera surface means that the longitudinal optical axis z' of a beam is not orthogonal to x_C and y_C, and thus the longitudinal phase terms kz and Φ_{Gouy} become dependent on x_C and y_C and hence part of Φ_{trans}. Φ_{rad} additionally gets distorted because there is now a multitude of

different wavefronts $1/R(z)$ present of the camera surface. Figure 26 and Figure 27 show the effects of tilt angles $\alpha_x = 0.01°$ and $\alpha_x = 0.1°$ on the shape of the transversal phase on the camera axis x_C and the phase range $\Phi_{\max} - \Phi_{\min}$ on the camera surface dependent on $z - z_0$. Note that linear offsets in the transversal phase on the left of both figures are still removed for clarity: $\Phi_{\text{trans}}(x_C, y_C, z) = \Phi(x_C, y_C, z) - \Phi_{\text{linear}}(0, 0, z) + \Phi_{\text{Gouy}}(0, 0, z)$.

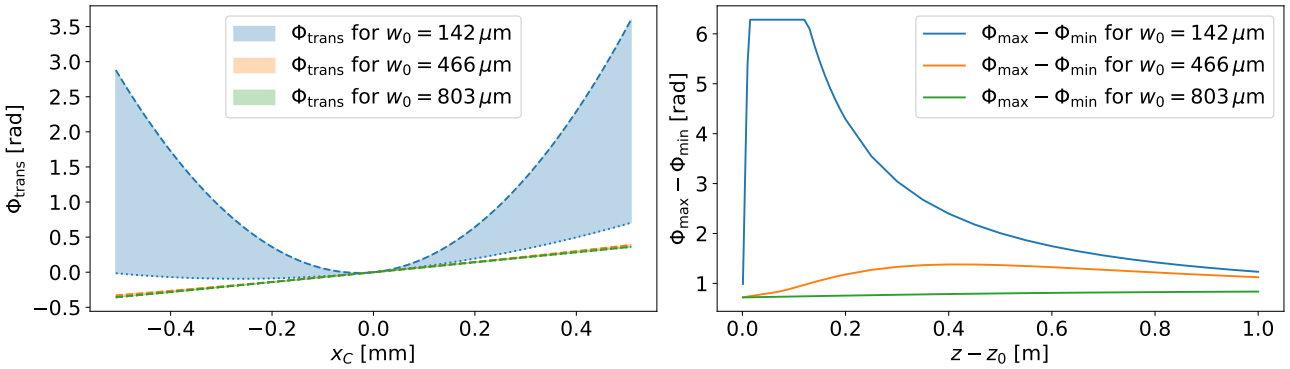

Figure 26: Left: Transverse phase term $\Phi_{\text{trans}} = \Phi_{\text{rad}}$ without any offsets, and $\alpha_x = 0.001°$ for $z - z_0 = 0.001\,\text{m}$ (dotted line) and $z - z_0 = 0.01\,\text{m}$ (dashed line) for all three carrier waist sizes (see Section 5). Right: Corresponding phase range on the camera plane.

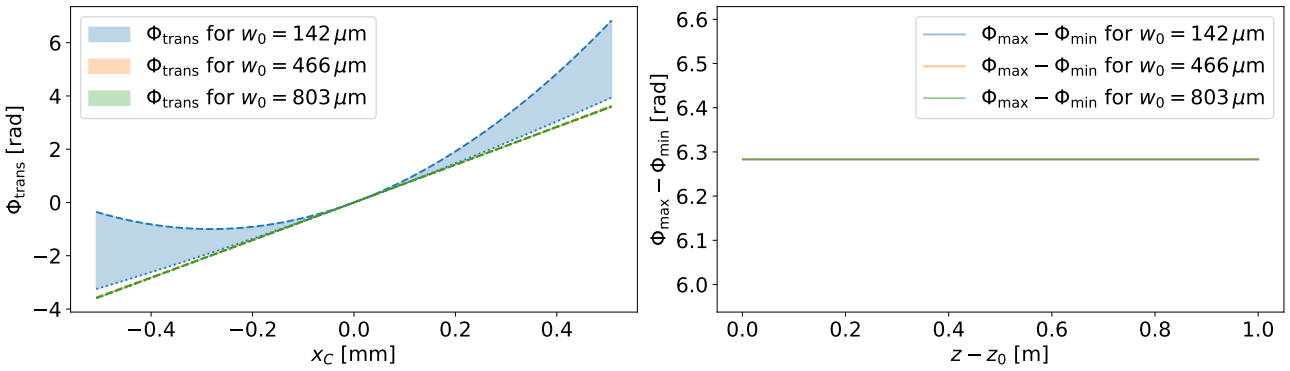

Figure 27: Left: Transverse phase term $\Phi_{\text{trans}} = \Phi_{\text{rad}}$ without any offsets, and $\alpha_x = 0.001°$ for $z - z_0 = 0.01\,\text{m}$ (dotted line) and $z - z_0 = 0.01\,\text{m}$ (dashed line) for all three carrier waist sizes (see Section 5). Right: Corresponding phase range on the camera plane.

While both curves on the left side of Figure 26 and Figure 27 show that the phase distribution on x_C simply tilts proportional to α_x, the curves in the plots on the right are vastly different between both figures. This is because the angle in Figure 27 is large enough that the phase jumps between 0 and 2π at least once over the entire $z - z_0$ range for all three beams which is underlined by the plot on the left, where all curves stretch from around -4 to 4 rad or -0.5 to 6.5 rad. Higher tilt angles result in multiple phase jumps between 0 and 2π and can thus lead to phase images that are difficult to resolve with a limited spacial resolution.

For phase differences, linear offsets d_{Cx}, d_{Cy} have the exact same effect as before in Figure 25. This can be seen in Figure 28, which shows the phase difference $\Phi_{\text{trans},1} - \Phi_{\text{trans},2}$ between all three example beams with an offset of $d_{Cx} = 0.3\,\text{mm}$ on the right, compared to the phase differences without any offsets on the left. The phase difference retains the radially symmetric shape of the transversal phase. Note that similar to beam phases, the phase difference with linear phase offsets

$\Phi_{\text{lin}}(0,0,z)+\Phi_{\text{Gouy}}(0,0,z)$ present results in the curves in Figure 28 simply shifting up/down without any change in shape.

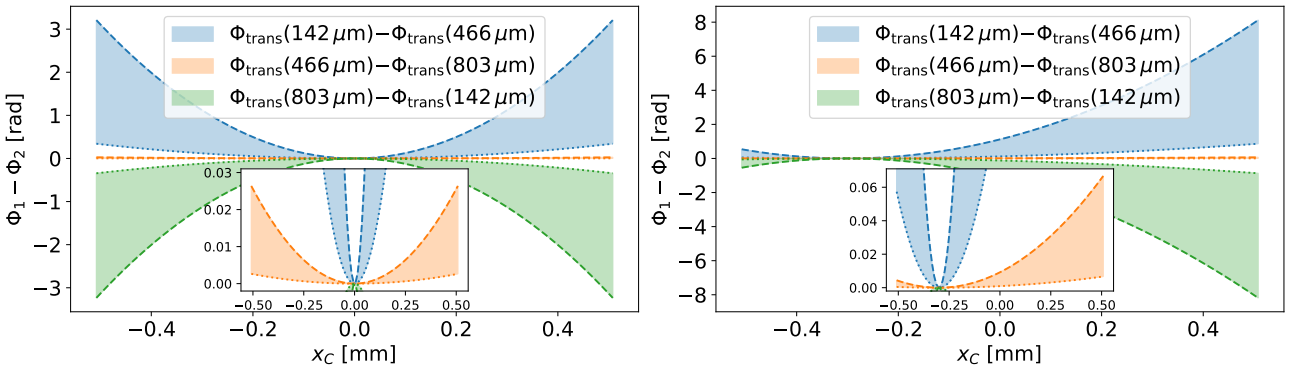

Figure 28: Left: Transverse phase difference $\Phi_{\text{trans},1}-\Phi_{\text{trans},2}$ without any (phase) offsets, and $d_{Cx}=0\,\text{mm}$ for $z-z_0=0.001\,\text{m}$ (dotted line) and $z-z_0=0.01\,\text{m}$ (dashed line) for all three carrier waist sizes (see Section 5). Right: Same plot for $d_{Cx}=0.3\,\text{mm}$.

Fortunately for relative phase measurements, tilt angles between beam and camera surface don't affect the shape of the phase difference $\Phi_{\text{trans},1}-\Phi_{\text{trans},2}$ as illustrated in Figure 29 that shows the effect of $\alpha_x=0.001°$ on the left, and the effect of $\alpha_x=0.01°$ on the right. Both curves shown here and the curve on the left side of Figure 28 for $\alpha_x=0°$ are the same. As such, only the angle between both beams matters. This is beneficial, because ensuring an angle of $\approx 0°$ between both beams and camera is difficult to accomplish.

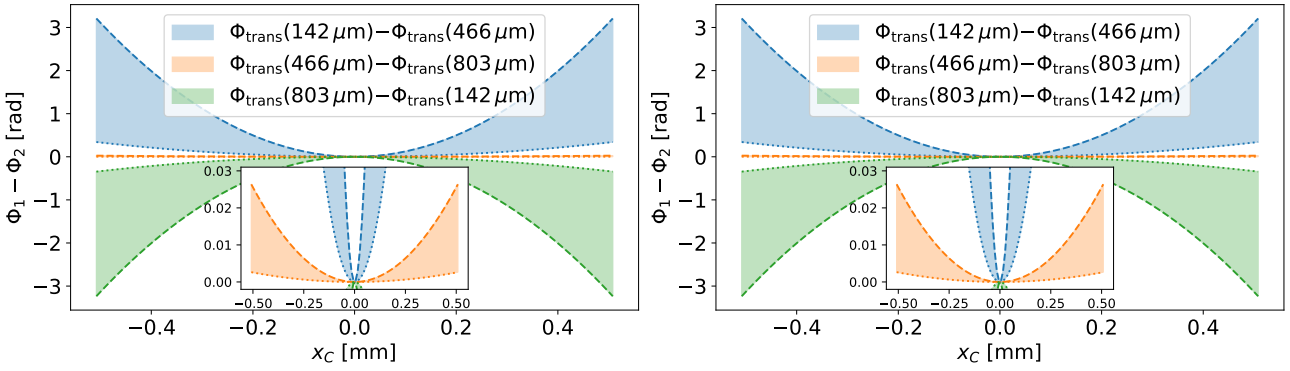

Figure 29: Left: Transverse phase difference $\Phi_{\text{trans},1}-\Phi_{\text{trans},2}$ without any (phase) offsets, and $\alpha_x=0.01°$ for $z-z_0=0.001\,\text{m}$ (dotted line) and $z-z_0=0.01\,\text{m}$ (dashed line) for all three carrier waist sizes (see Section 5). Right: Same plot for $\alpha_x=0.01°$.

The result of tilting one the beams with an angle of $\epsilon_x=0.01°$ is shown in Figure 30. As seen, the effect is similar to the effect of camera tilt on pure beam phase in Figure 29 where the transversal phase profile tilts proportional to ϵ_x resulting in a (in this case only slightly) larger phase range on the camera plane as shown in the plot ont the right of Figure 30.

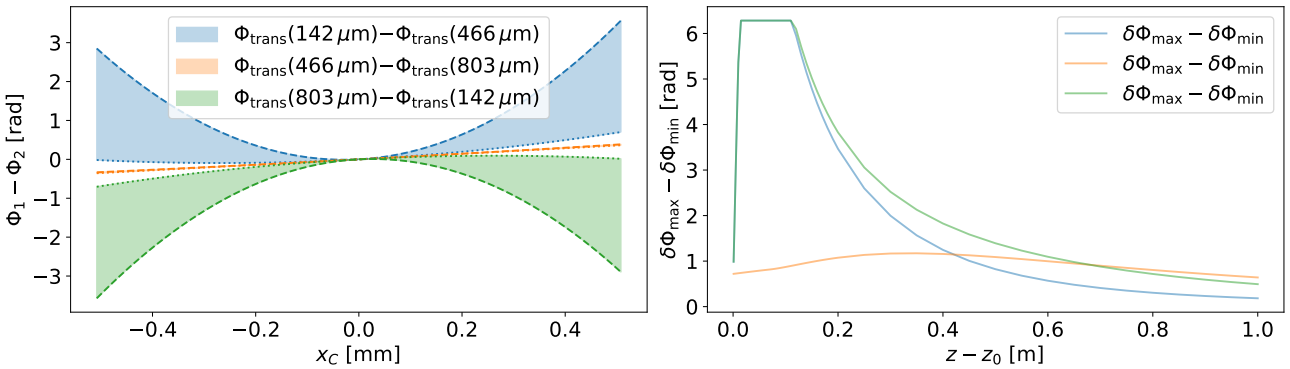

Figure 30: Left: Transverse phase difference $\Phi_{\text{trans},1} - \Phi_{\text{trans},2}$ without any (phase) offsets, and $\epsilon_{x,2} = 0.01°$ for $z - z_0 = 0.001\,\text{m}$ (dotted line) and $z - z_0 = 0.01\,\text{m}$ (dashed line) for all three carrier waist sizes (see Section 5). Right: Corresponding phase range on the camera plane.

The most asymmetric shape between different beam constellations is obtained when offsetting one of the beams relative to the other. This can be seen in Figure 31 for an offset of $d_{x0,2} = 0.3\,\text{mm}$. The blue and orange configurations are barely displaced compared to the green one which has a new phase center at $> 0.3\,\text{mm}$.

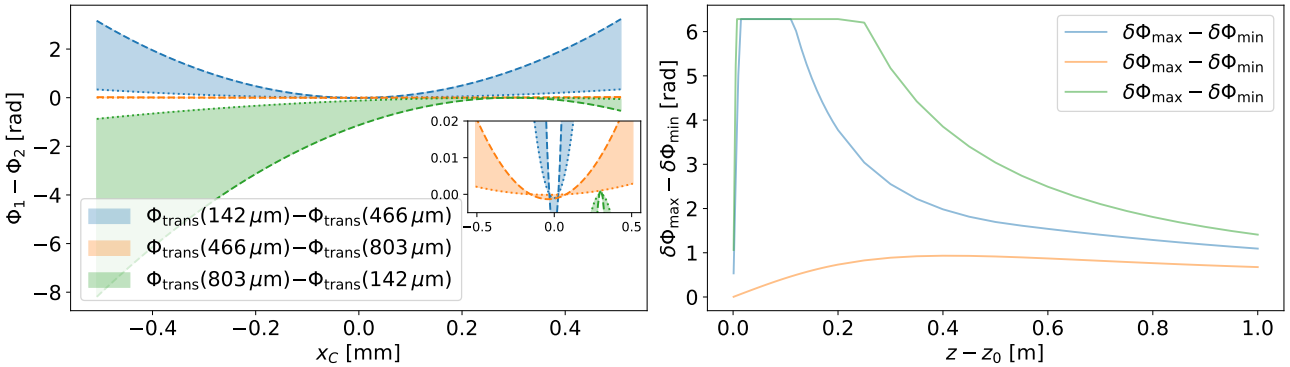

Figure 31: Left: Transverse phase difference $\Phi_{\text{trans},1} - \Phi_{\text{trans},2}$ without any (phase) offsets, and $d_{0x,2} = 0.3\,\text{mm}$ for $z - z_0 = 0.001\,\text{m}$ (dotted line) and $z - z_0 = 0.01\,\text{m}$ (dashed line) for all three carrier waist sizes (see Section 5). Right: Corresponding phase range on the camera plane.

5 Measurements

5.1 Fundamental measurement aspects

The phase camera captures two superimposed laser beams with the methods outlined in Section 2.3 and Section 3.3 with 22 pixels currently and can then demodulate the signals for each pixel into phase difference and intensity data for the EOM beam carrier frequency and both of its sidebands. Figure 32 shows the recorded data of a single measurement for the first setting with $z_{\text{lens2}} = (-0.4470 \pm 0.0028)\,\text{m}$. First thing to note is that the intensity data for all frequency bands is not perfectly Gaussian. The reason for this is that by the time of this work, the camera is not calibrated yet. Intensity detected per pixel might differ depending on factors such as different attenuation factors of cables or pixel fiber tilts resulting in varying mode matching efficiencies for coupling light into the fibers. Hence for this low spacial resolution, intensity profiles may appear non-Gaussian, but higher resolutions should be able to mitigate this issue. In principle it is irrelevant for phase demodulation however, as the absence of calibration between the pixels does not affect the ratio between AOM and EOM beam intensity detected by individual pixels. It could negatively affect signal-to-noise ratio however. As can be seen in Figure 32, the phase profiles of the three frequency bands match each other in shape, while having a linear offset between each other. This is what is expected. A $\pm 10\,\text{MHz}$ offset changes 1550.141 nm light ($f \approx 193\,\text{THz}$) only marginally, which means that the radial phase profile stays effectively the same while it's still enough to cause a noticeable linear phase shift. From here on, only the carrier frequency is used for phase analysis.

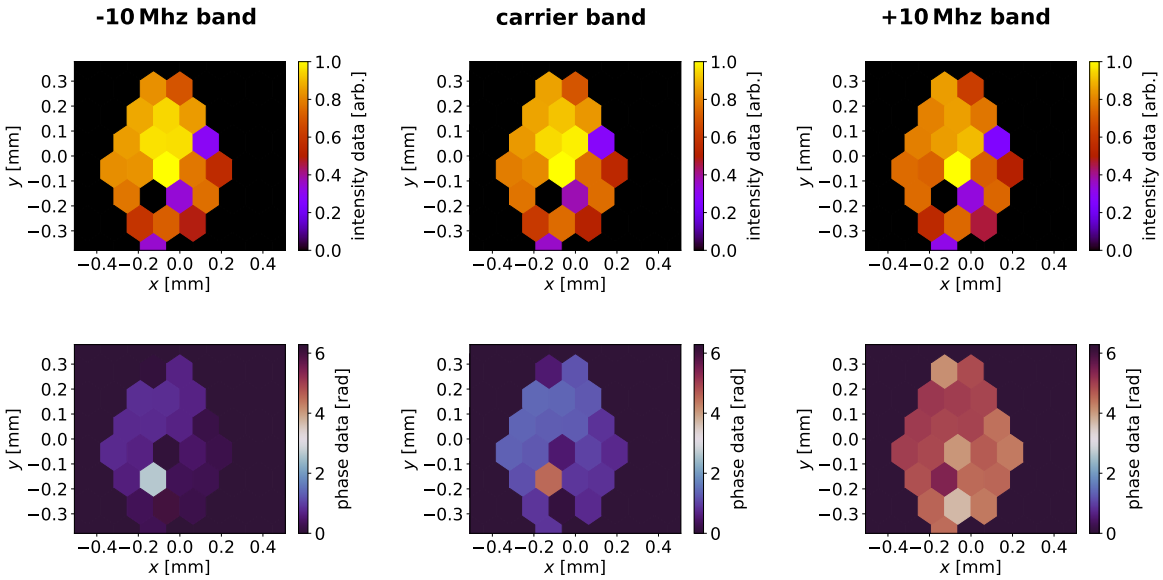

Figure 32: Intensity (top) and phase data (bottom) for all three EOM beam frequency bands of a measurement with the phase camera.

To determine the accuracy of the phase camera, We can take two successive measurements with the exact same settings, which should yield the same transversal phase profile for both measurements. As can be seen in Figure 33, as expected, the shape of both arrays are effectively the same plus a linear offset that is a result of the linear temporal phase change of the laser light. With the exception of pixel 43, there seems to be only a small error in the consistency of the phase data sets. Calculating the standard derivation of the phase difference points, which can be seen at the bottom of Figure 33, we get 0.04 rad in total, and 0.005 rad if we exclude pixel 43, which could differ this much because for example its power cable was slightly dislodged during measurements. This is likely, because both in

Figure 32 and Figure 33 its value seems to be always the same ($\Phi_{p43} \approx 4.51\,\mathrm{rad}$), while its intensity in Figure 32 is not exactly, but close to zero with a magnitude that is 10^3 lower than the intensities in the other pixels.

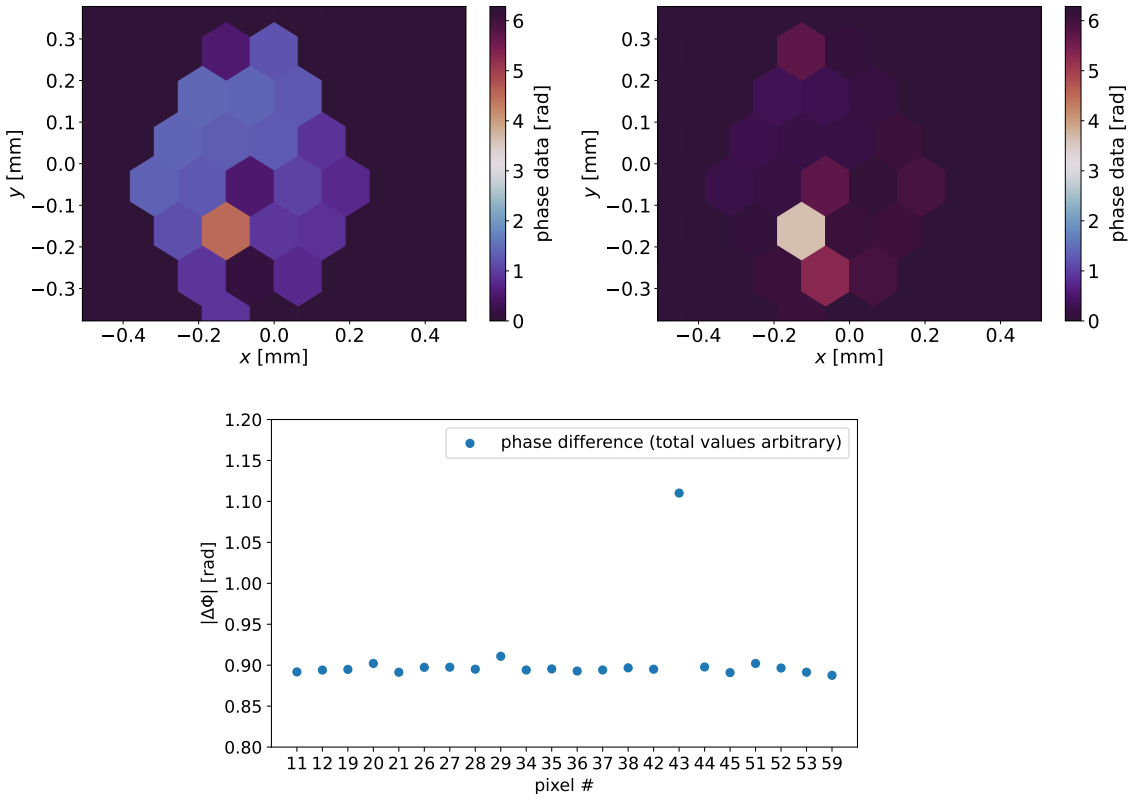

Figure 33: Phase data of two measurements taken in quick succession (top) and phase differences between both measurements for each pixel (bottom). Only the difference between the points is relevant. The total value is arbitrary.

Aside from pixel 43, which was nonfunctional during many of the measurements, other pixels seem to have spontaneously seized working properly during some successive measurements but then resumed functionality later during the same set of measurements. Three specific pixels, namely pixel 11, 36, and 52 were permanently defective. The reason for this is yet unclear. Malfunctioning pixels may stand out as they display phase values that are not coherent to the surrounding phase profile, or create shapes that are not possible to replicate with Gaussian beam theory. An example for the latter can be seen on the left in Figure 41 in the shape of a half ring.

5.2 Altering the reference beam

Multiple minor setup alterations were made to test the dependence of the test beam reconstruction on the wavefront of the reference beam. These were the inclusion of an additional lens at different positions, and in the first case, the movement of lens 1 in CS 2 by $\pm 7\,\mathrm{mm}$.

5.2.1 Marginal beam difference

Changing the position of lens 1 changes the beam radius $w(z)$ and wavefront $1/R(z)$ of the AOM beam marginally, which can be seen in Figure 34 and Figure 35. The waist and it's position changes from

$w_{0,\mathrm{AOM}} = (470 \pm 30)\,\mu\mathrm{m}$ at $z_{0,\mathrm{AOM}} = (0.87 \pm 0.06)\,\mathrm{m}$ to $w_{0,\mathrm{AOM,plus}} = (480 \pm 30)\,\mu\mathrm{m}$ at $z_{0,\mathrm{AOM,plus}} = (0.87 \pm 0.06)\,\mathrm{m}$, and $w_{0,\mathrm{AOM,minus}} = (453 \pm 29)\,\mu\mathrm{m}$ at $z_{0,\mathrm{AOM,plus}} = 0.87 \pm 0.05)\,\mathrm{m}$.

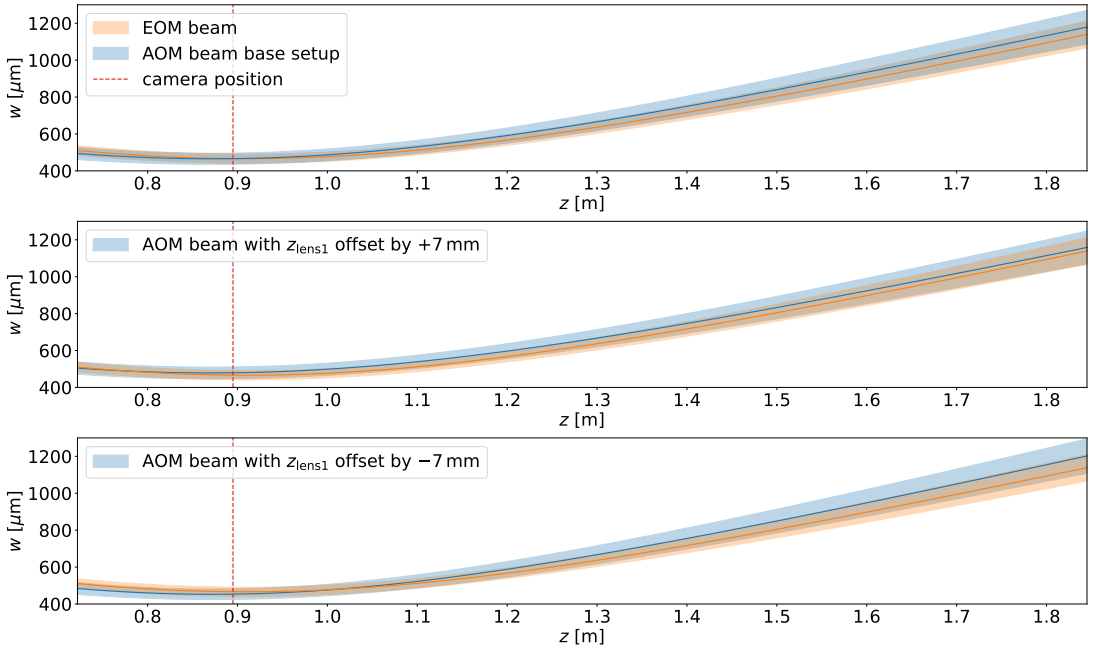

Figure 34: Beam radius $w(z)$ of the EOM and AOM beam for the base setup (top), for shifting the position of lens 1 by +7 mm (middle), and by −7 mm (bottom). The red line indicates the location where the camera was placed for recording ($z = z_{\mathrm{Piezo}} + 5\,\mathrm{cm} = (0.895 \pm 0.008)\,\mathrm{m}$).

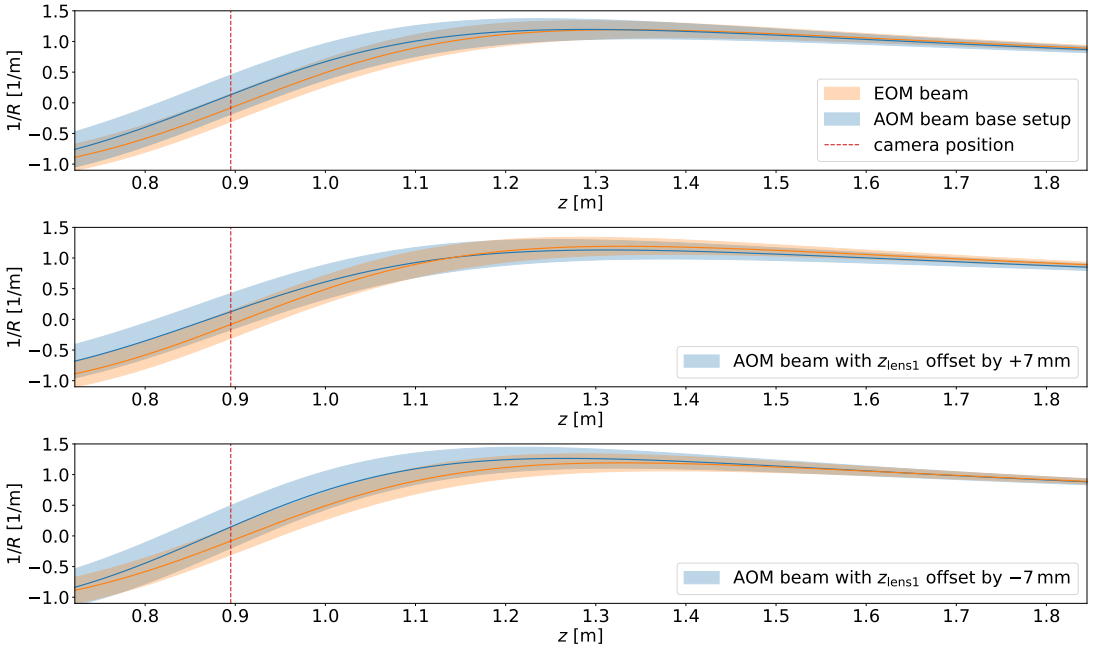

Figure 35: Wavefront $1/R(z)$ of the EOM and AOM beam for the base setup (top), for shifting the position of lens 1 by +7 mm (middle), and by −7 mm (bottom). The red line indicates the location where the camera was placed for recording ($z = z_{\mathrm{Piezo}} + 5\,\mathrm{cm} = (0.895 \pm 0.008)\,\mathrm{m}$).

Figure 40 and Figure 45 show that at the position where the camera was placed for recording, which is close to the focus, the base setup displays marginally better mode matching than the other two settings. Figure 36 shows the recorded phase data of all three lens 1 positions together with simulations of the expected shapes and the difference between both.

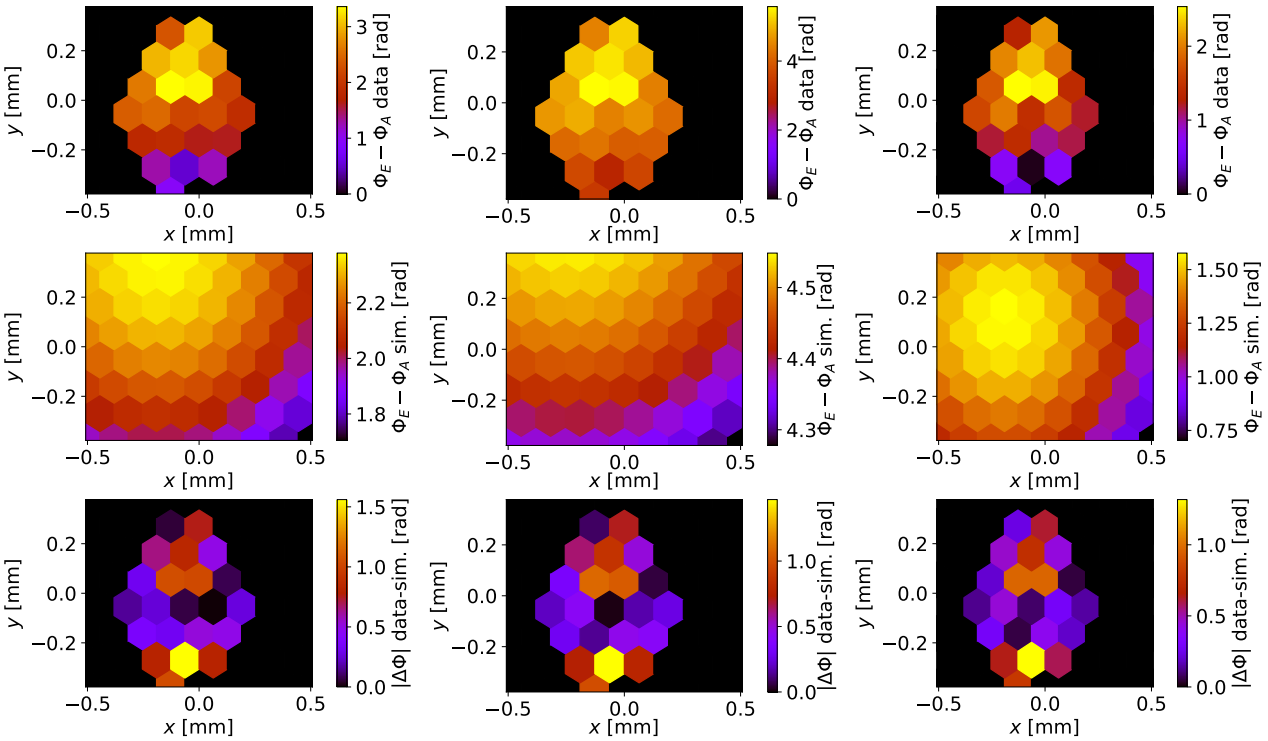

Figure 36: Recorded phase data (top) for $z_{\text{lens1}} - 7\,\text{mm}$ (left), base setup (middle), and $z_{\text{lens1}} + 7\,\text{mm}$ (right), as well as simulations (middle row), and difference $|\Delta\Phi| = |\delta\Phi_{\text{data}} - \delta\Phi_{\text{sim}}|$.

As can be seen in Figure 36, the shapes of the phase profiles all look similar, which is not surprising because the camera was not moved between recordings. However, due to the movement of lens 1 between the measurements in order to change the AOM beam, its trajectory is slightly different in each setting. Since the AOM beam passes seven optical elements behind lens 1, moving it by hand will inevitably result in some change in the angle between the trajectory of the beam and the optical lab axis z and thus also between the trajectories between AOM and EOM beam. Beam trajectories were measured for all three lens configurations and can be seen in Figure 75. Overall we would expect phase differences $\Phi_e - \Phi_A$ that are either the same across all three measurements or slightly different. However, it seems that this particular set of measurements does not yield much correlation to simulations. We can quantify the discrepancy between data and simulation and arrive at a total difference of $(0.5 \pm 0.3)\,\text{rad}$, $(0.5 \pm 0.3)\,\text{rad}$, $(0.5 \pm 0.4)\,\text{rad}$ for the three configurations from left to right. If we exclude the three broken pixels 11, 36, and 52, we get $(0.44 \pm 0.28)\,\text{rad}$ for $z_{\text{lens1}} - 7\,\text{mm}$, $(0.5 \pm 0.3)\,\text{rad}$ for the base setup, and $(0.5 \pm 0.3)\,\text{rad}$ for $z_{\text{lens1}} + 7\,\text{mm}$. By the signature of the phase profiles in Figure 36, and the corresponding intensity, it also seems that pixels 27 and 28 did not function properly during this recording. If we exclude them too, then we arrive at a total difference between recorded data and simulations of $(0.38 \pm 0.28)\,\text{rad}$, $(0.47 \pm 0.26)\,\text{rad}$, and $(0.48 \pm 0.28)\,\text{rad}$. This is not a good result, and much worse than for later measurements in the Sections below. The overall shapes of the recorded data, especially in the plot on the right, look very chaotic and non-Gaussian. Since this set was taken quite early after the principle functionality of the phase camera was achieved, it is possible that there was still some kink in data acquisition and processing that was

later ironed out before the other measurements were taken. We can still take a look at Figure 37, Figure 38, and Figure 39, which show the simulated 64-pixel scale phase profiles of both AOM and EOM beam for each of the three configurations, as well as the phase difference $\Phi_A - \Phi_E$ according to the reconstruction in Figure 36.

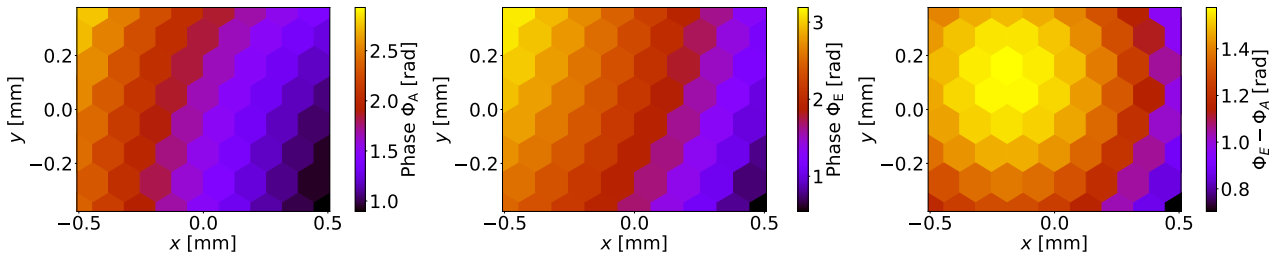

Figure 37: Phase simulations for EOM and AOM beam for $z_{\text{lens1}} - 7\,\text{mm}$. Left: Phase of the AOM beam. Middle: Phase of the EOM beam. Right: Phase difference $\Phi_A - \Phi_E + lpo$ with $lpo = 1.056\,\text{rad}$.

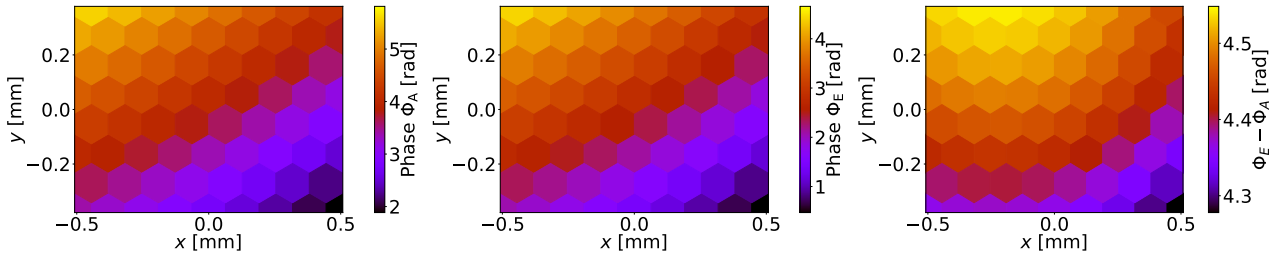

Figure 38: Phase simulations for EOM and AOM beam for the base setup. Left: Phase of the AOM beam. Middle: Phase of the EOM beam. Right: Phase difference $\Phi_A - \Phi_E + lpo$ with $lpo = 5.692\,\text{rad}$.

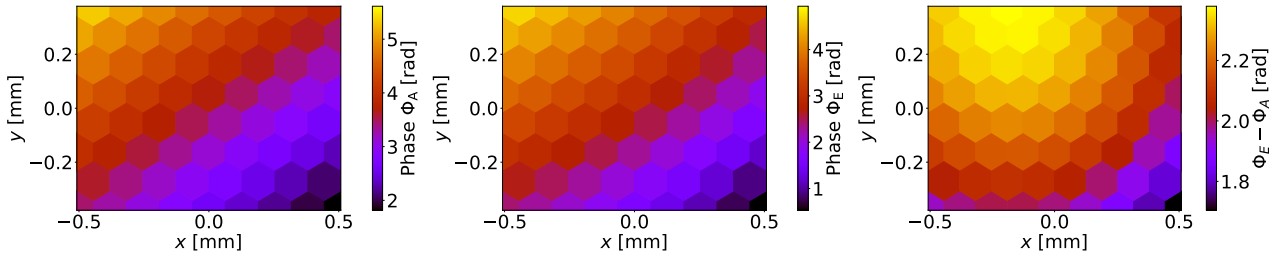

Figure 39: Phase simulations for EOM and AOM beam for $z_{\text{lens1}} + 7\,\text{mm}$. Left: Phase of the AOM beam. Middle: Phase of the EOM beam. Right: Phase difference $\Phi_A - \Phi_E + lpo$ with $lpo = 2.989\,\text{rad}$.

What can be seen when comparing the phase difference in Figure 37, Figure 38, and Figure 39 is that the phase difference in all configurations is similar, but shifted in position. The reason for this is mostly the effect of varying AOM and EOM beam trajectories between the three setups. Unfortunately the exact settings cannot be determined/verified due to the poor quality of the measurement.

5.2.2 Smaller and larger reference beam

After examining marginal wavefront differences, the next step was to investigate more pronounced variations. By adding an additional lens to the optical setup at $z = (-0.100 \pm 0.003)\,\mathrm{m}$ with a focal length of $f = 1\,\mathrm{m}$, we can create a beam configuration in front of the camera, where the AOM beam is both smaller and larger than the EOM beam dependent on different camera positions. This setup can be seen in Figure 40. The AOM here has a waist radius of $w_{0,\mathrm{AOM}} = (313 \pm 19)\,\mu\mathrm{m}$ at $z_{0,\mathrm{AOM}} = (0.950 \pm 0.027)\,\mathrm{m}$.

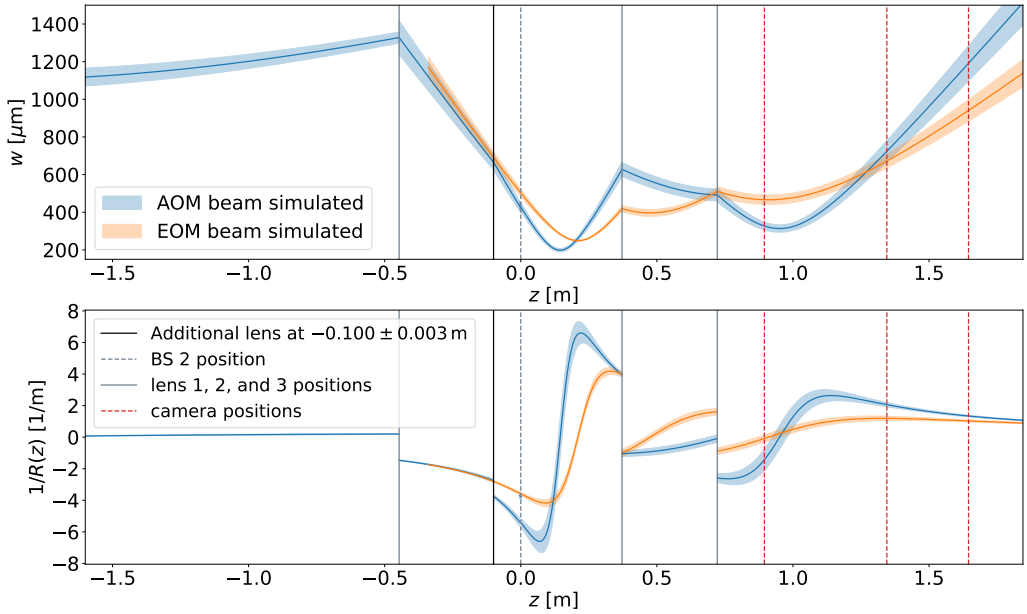

Figure 40: Beam radius $w(z)$ (top) and wavefront $1/R(z)$ (bottom) in the second coordinate system. With $z_{\mathrm{lens2}} = (0.372 \pm 0.004)\,\mathrm{m}$ and an additional lens at $z = (-0.100 \pm 0.003)\,\mathrm{m}$. The red lines indicate camera positions for measurements.

As can be seen in Figure 40, the three camera positions for measurements are at a location where both w and $1/R$ of the AOM beam are smaller than those of the EOM beam (left), a location where it is the other way around (right), and a position where both beams have approximately the same size but the AOM beam wavefront is larger. These positions are $z = z_{\mathrm{Piezo}} + 5\,\mathrm{cm} = (0.895 \pm 0.008)\,\mathrm{m}$, $z = z_{\mathrm{Piezo}} + 50\,\mathrm{cm} = (1.345 \pm 0.008)\,\mathrm{m}$, and $z = z_{\mathrm{Piezo}} + 80\,\mathrm{cm} = (1.645 \pm 0.008)\,m$. Figure 41 shows the recorded phase data of all three camera positions together with simulations of the expected shapes and the difference between both. Measured beam trajectories can be found in Figure 73.

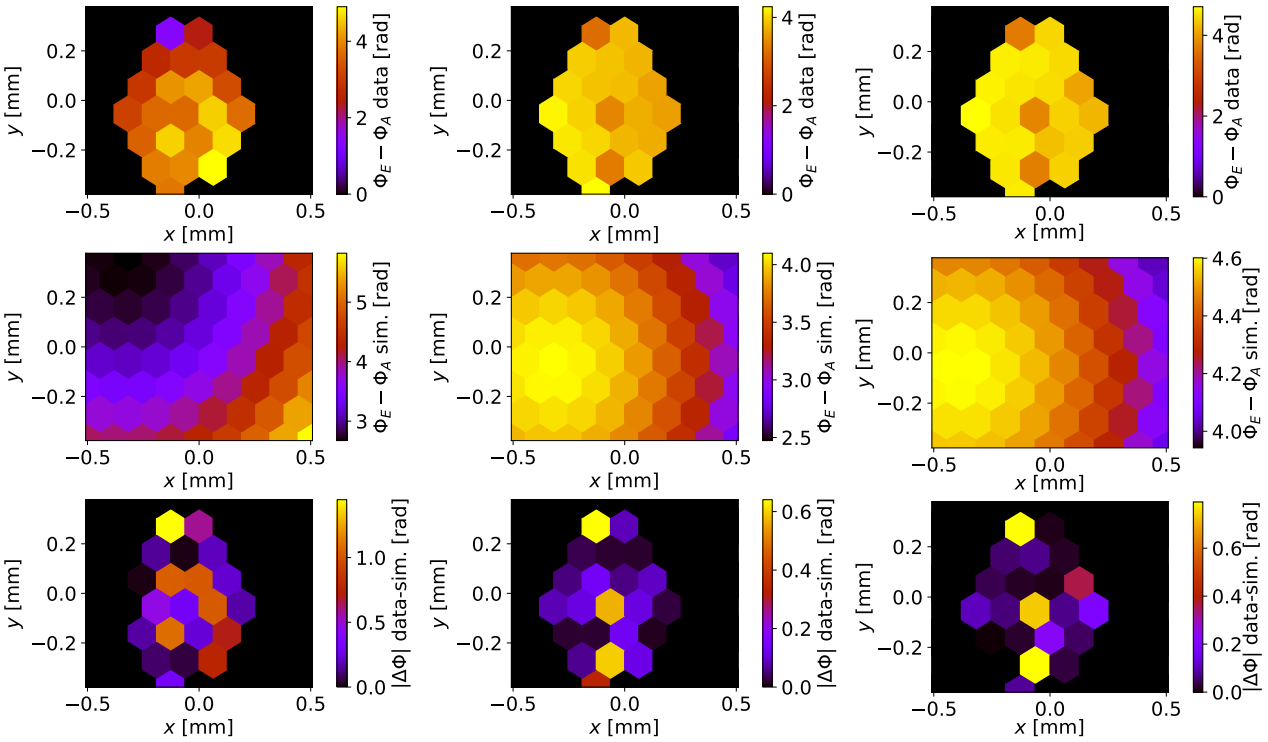

Figure 41: Recorded phase data (top) for $z_{\text{cam}} = z_{\text{Piezo}} + 5\,\text{cm}$ (left), $z_{\text{cam}} = z_{\text{Piezo}} + 50\,\text{cm}$ (middle), and $z_{\text{cam}} = z_{\text{Piezo}} + 80\,\text{cm}$ (right), as well as simulations (middle row), and difference $|\Delta\Phi| = |\delta\Phi_{\text{data}} - \delta\Phi_{\text{sim}}|$ for setup with additional lens at $z = (-1.000 \pm 0.003)\,\text{m}$.

The phase profiles in Figure 41 look similar for the plots in the middle and right side. It seems that for the measurement on the left, some of the pixels (11, 27, 28, 37, 43, 45, and 53) are not working correctly. Interestingly, two of the three fundamentally broken pixels 11, 36, and 52 that all show values that don't fit a coherent phase profile in the middle and on the right, don't display a noticeable difference on the left. The total difference between the data values and simulation for $z_{\text{cam}} = z_{\text{Piezo}} + 5\,\text{cm}$ on the left is $(0.5 \pm 0.4)\,\text{rad}$, unmodified, $(0.4 \pm 0.4)\,\text{rad}$ without pixels 11, 36, 52, and $(0.20 \pm 0.17)\,\text{rad}$ additionally without pixels 27, 28, 37, 43, 45, and 53. For the middle with $z_{\text{cam}} = z_{\text{Piezo}} + 50\,\text{cm}$ and the right with $z_{\text{cam}} = z_{\text{Piezo}} + 80\,\text{cm}$, the differences between data and simulation are $(0.15 \pm 0.19)\,\text{rad}$ and $(0.17 \pm 0.25)\,\text{rad}$ unmodified, and $(0.08 \pm 0.07)\,\text{rad}$ and $(0.08 \pm 0.09)\,\text{rad}$ without pixels 11, 36, 52. These two values are much better than the differences between data and simulations obtained for the first measurements in Section 5.2.1 above. The only measurement here, where data and simulation does not correlate as well is the one on the right in Figure 41. This could indicate that larger beams are more easily resolved than smaller beams, but it might also be a consequence of the diminished resolution due to so many pixels malfunctioning, that obscures the analysis of the data. The phase difference between AOM and EOM beam is simulated in Figure 42, Figure 43, and Figure 44.

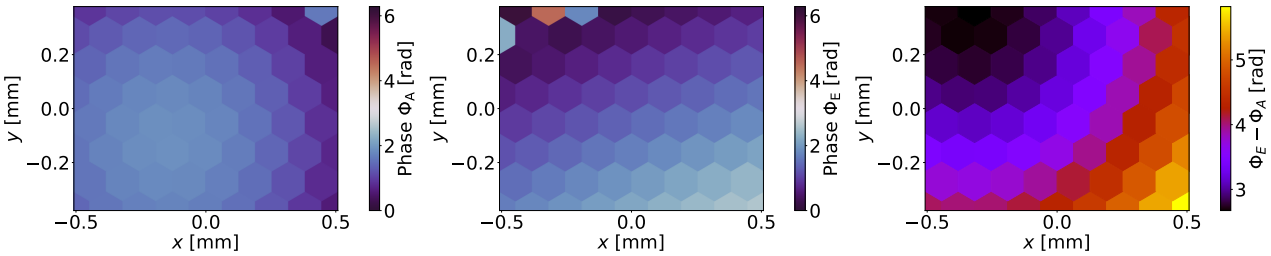

Figure 42: Phase simulations for EOM and AOM beam for and additional lens at $z = (-0.100 \pm 0.003)\,\mathrm{m}$ at the measurement position $z_{\mathrm{cam}} = z_{\mathrm{Piezo}} + 5\,\mathrm{cm}$. Left: Phase of the AOM beam. Middle: Phase of the EOM beam. Right: Phase difference $\Phi_A - \Phi_E + lpo$ with $lpo = 3.813$.

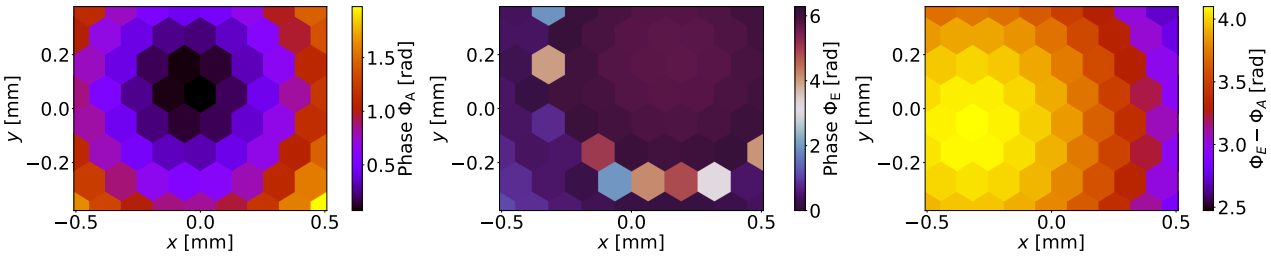

Figure 43: Phase simulations for EOM and AOM beam for and additional lens at $z = (-0.100 \pm 0.003)\,\mathrm{m}$ at the measurement position $z_{\mathrm{cam}} = z_{\mathrm{Piezo}} + 50\,\mathrm{cm}$. Left: Phase of the AOM beam. Middle: Phase of the EOM beam. Right: Phase difference $\Phi_A - \Phi_E + lpo$ with $lpo = 4.439$.

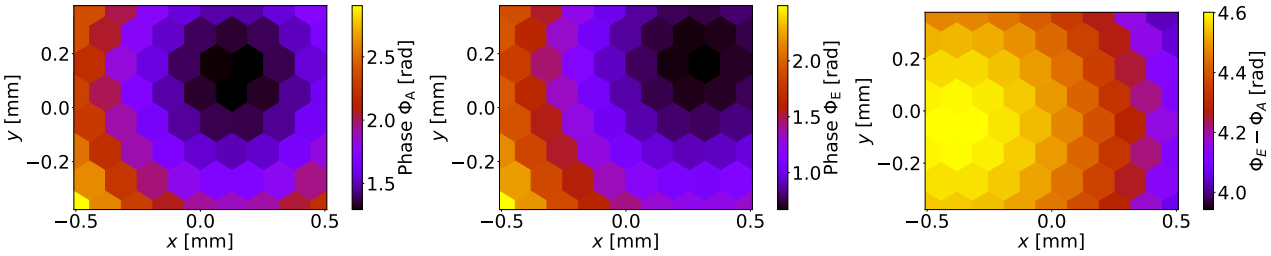

Figure 44: Phase simulations for EOM and AOM beam for and additional lens at $z = (-0.100 \pm 0.003)\,\mathrm{m}$ at the measurement position $z_{\mathrm{cam}} = z_{\mathrm{Piezo}} + 80\,\mathrm{cm}$. Left: Phase of the AOM beam. Middle: Phase of the EOM beam. Right: Phase difference $\Phi_A - \Phi_E + lpo$ with $lpo = 4.959$.

As seen in Figure 42, Figure 43, and Figure 44 the range of the phase differences $\Phi_E - \Phi_A$ decreases with beam size, showing a range of $\approx 3\,\mathrm{rad}$ in Figure 42, $\approx 1.5\,\mathrm{rad}$ in Figure 43, and $\approx 0.6\,\mathrm{rad}$ in Figure 44. While this scenario doesn't exactly match the examples shown in Figure 30 and Figure 31, where the phase difference range on the camera surface is shown for different beam combinations, with small, medium and large waist, it still shows that the progression away from the focal position is either a continuous decrease in the range of the phase difference, or a small brief increase followed by a decrease. Given that the decrease shown for the example with a small and medium sized waist is a continuous, drastic decrease, it is feasible that in the case of these three measurements here, the progression of the phase difference range over distance is also a continuous but with less drastic decrease. For individual measurements it is in principle possible to create a setting with the best overlap with recorded data through different beam parameter configurations. That is why it is important to take measurements at different beam positions, as it allows to filter out settings that look correct at one position, but don't match at others. Even though the data-simulation match in the case of the measurement in

Figure 42 is not nearly as good as for the other two, a better setting at this location could not be found within the range of the standard derivations of the beam parameters. Additional points of interests in Figure 42 and Figure 43 are the hexbin artefacts on the left and middle of Figure 42 and in the middle of 43 at the location on x_C and y_C where $\Phi = 2\pi$. The circular colorbar in the three plots is meant to erase the hard cut between 2π and 0, but it seems that matplotlib gets confused at the transition, instead displaying values in the middle between 0 and 2π.

5.2.3 Very large reference beam

By placing the additional lens to $z = (-1.000 \pm 0.003)\,\mathrm{m}$ instead of $z = (-0.100 \pm 0.003)\,\mathrm{m}$ a beam configuration was created where the wavefront of AOM and EOM beam are inversed at the position of BS 2. With this, the waist of the AOM beam assumes the radius $w_{0,\mathrm{AOM}} = (163 \pm 9)\,\mu\mathrm{m}$ at $z_{0,\mathrm{AOM}} = (0.758 \pm 0.015)\,\mathrm{m}$. The beam radii $w(z)$ and wavefronts $1/R(z)$ for this setup are shown in Figure 45.

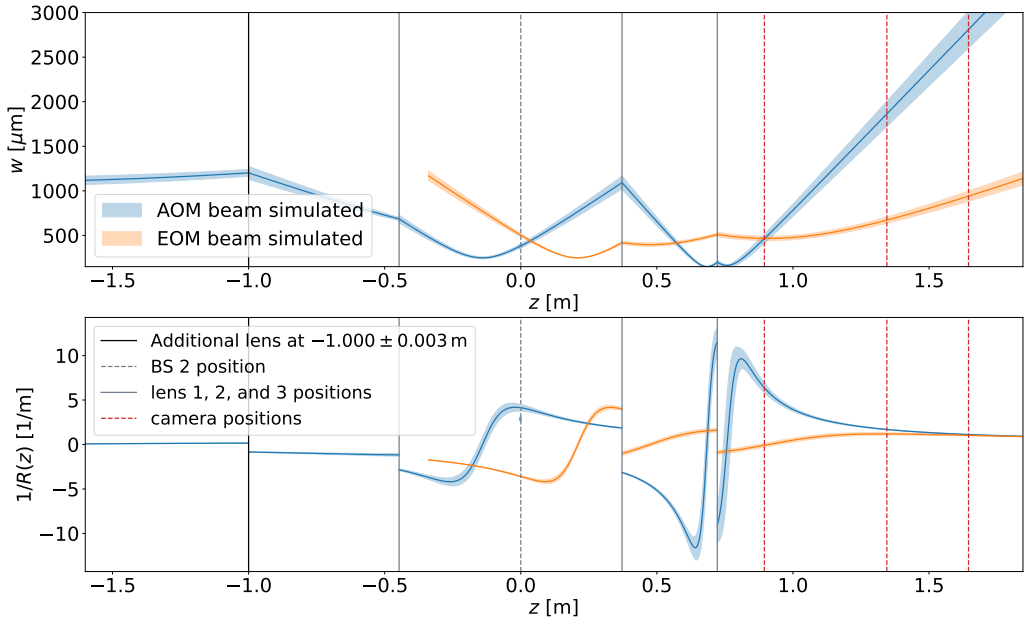

Figure 45: Beam radius $w(z)$ (top) and wavefront $1/R(z)$ (bottom) in the second coordinate system. With $z_{\mathrm{lens2}} = (0.372 \pm 0.004)\,\mathrm{m}$ and an additional lens at $z = (-1.000 \pm 0.003)\,\mathrm{m}$. The red lines indicate camera positions for measurements.

The configuration in Figure 45 creates an AOM beam with a small focus close to lens 3, which allows for a measurement, where both beams have the same radius, with a positive wavefront for the AOM beam and negative wavefront for the EOM beam ($z = z_{\mathrm{Piezo}} + 5\,\mathrm{cm}$, left). Another measurement is located where the wavefronts are inversed in reference to the first position, and the AOM beam is much larger ($z = z_{\mathrm{Piezo}} + 50\,\mathrm{cm}$, middle). For the third measurement position ($z = z_{\mathrm{Piezo}} + 80\,\mathrm{cm}$, right), similar applies to the radial difference, but the wavefront between both beams is approximately equal. For this setup, the recorded phase data of all three measurements, corresponding phase simulations, and the difference between both can be seen in Figure 46.

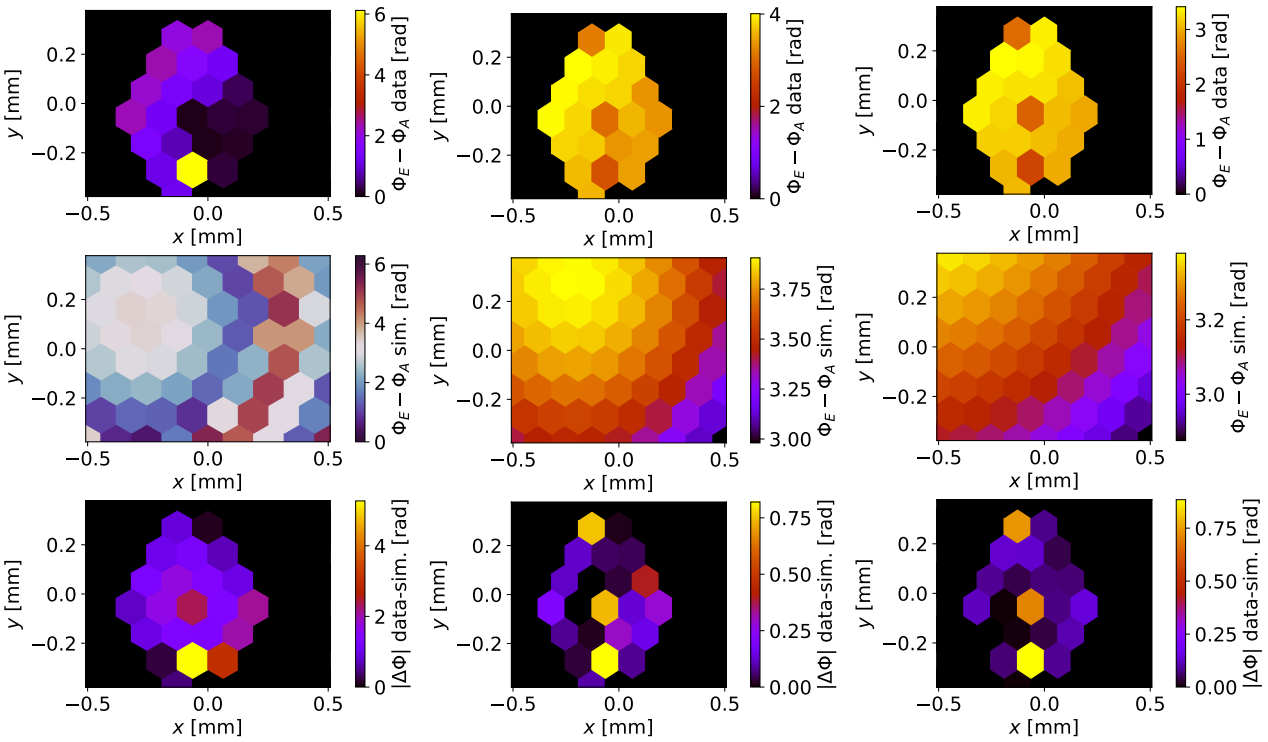

Figure 46: Recorded phase data (top) for $z_{\text{cam}} = z_{\text{Piezo}}+5\,\text{cm}$ (left), $z_{\text{cam}} = z_{\text{Piezo}}+50\,\text{cm}$ (middle), and $z_{\text{cam}} = z_{\text{Piezo}}+80\,\text{cm}$ (right), as well as simulations (middle row), and difference $|\Delta\Phi| = |\delta\Phi_{\text{data}} - \delta\Phi_{\text{sim}}|$ for setup with additional lens at $z = (-1.000 \pm 0.003)\,\text{m}$.

Like previously in Section 5.2.2, the reconstructions of the phase differences $\Phi_E - \Phi_A$ in Figure 46 shows a good correlation between simulation and recorded data for the measurement with the largest beam, but in this case the accuracy diminishes with decreasing beam size. Extracting the total phase difference in recorded data and simulations from the plots at the bottom, for $z_{\text{cam}} = z_{\text{Piezo}} + 5\,\text{cm}$ (left), $z_{\text{cam}} = z_{\text{Piezo}} + 50\,\text{cm}$ (middle), and $z_{\text{cam}} = z_{\text{Piezo}} + 80\,\text{cm}$ (right), we obtain $(1.4 \pm 1.1)\,\text{rad}$, $(0.20 \pm 0.25)\,\text{rad}$, and $(0.17 \pm 0.25)\,\text{rad}$ in total, and $(1.2 \pm 0.7)\,\text{rad}$, $(0.11 \pm 0.11)\,\text{rad}$, and $(0.07 \pm 0.05)\,\text{rad}$ without the faulty pixels 11, 36, and 52. While the correlation for the measurements in the middle and right side are satisfactory, it seems that the measurement on the left is very poor. This measurement point combines an EOM beam at approximately its focal position with a small, highly curved AOM beam of approximately equal size. The result is a beam with a highly unspherical intensity profile (see Figure 72) with a quickly accelerating phase ring. The recorded phase data does not match this shape at all. After Section 5.2.1 and Section 5.2.2 this is the third measurement at this EOM beam's focus, of which none yielded accurate results. If we exclude Section 5.2.1 for potential problems in the signal processing chain and compare only the latter two sets of measurements, then it seems that there might be a correlation between beam wavefront $1/R$ and accuracy between recorded data and simulations. The smaller and closer together the wavefronts of the two beams are, the higher the accuracy. However, the available data is insufficient to confirm this. Similarly to before, Figure 47, Figure 48, and Figure 49 show the phase difference between AOM and EOM beam, and Figure 74 shows the measured trajectories of both beams.

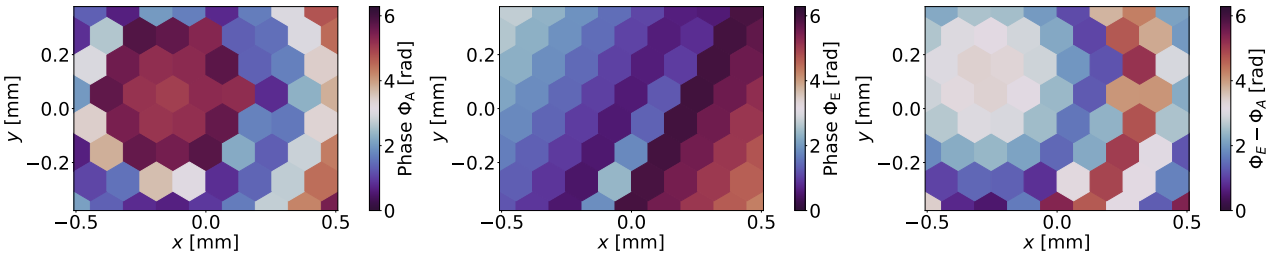

Figure 47: Phase simulations for EOM and AOM beam for and additional lens at $z = (-1.000 \pm 0.003)\,\mathrm{m}$ at the measurement position $z_{\mathrm{cam}} = z_{\mathrm{Piezo}} + 5\,\mathrm{cm}$. Left: Phase of the AOM beam. Middle: Phase of the EOM beam. Right: Phase difference $\Phi_A - \Phi_E + lpo$ with $lpo = 0.806\,\mathrm{rad}$.

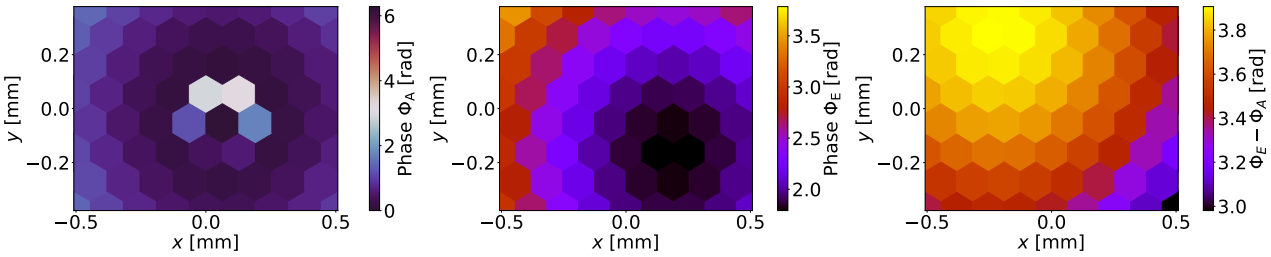

Figure 48: Phase simulations for EOM and AOM beam for and additional lens at $z = (-1.000 \pm 0.003)\,\mathrm{m}$ at the measurement position $z_{\mathrm{cam}} = z_{\mathrm{Piezo}} + 50\,\mathrm{cm}$. Left: Phase of the AOM beam. Middle: Phase of the EOM beam. Right: Phase difference $\Phi_A - \Phi_E + lpo$ with $lpo = 1.826\,\mathrm{rad}$.

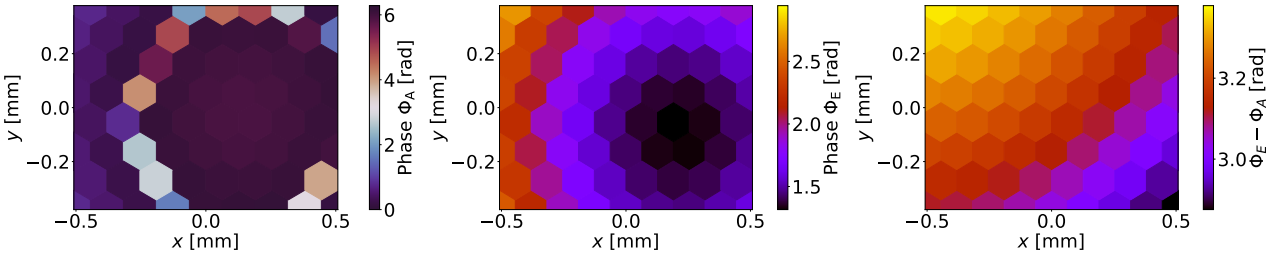

Figure 49: Phase simulations for EOM and AOM beam for and additional lens at $z = (-1.000 \pm 0.003)\,\mathrm{m}$ at the measurement position $z_{\mathrm{cam}} = z_{\mathrm{Piezo}} + 80\,\mathrm{cm}$. Left: Phase of the AOM beam. Middle: Phase of the EOM beam. Right: Phase difference $\Phi_A - \Phi_E + lpo$ with $lpo = 1.414\,\mathrm{rad}$.

As the beam waists in this setup configuration match the example in Figure 30 and Figure 31 with medium and small waist very well, so does the phase difference range in Figure 47, Figure 48, and Figure 49, first displaying a range of 2π, and then continuously decreasing with distance. First to $\approx 0.9\,\mathrm{rad}$, and subsequently to $\approx 0.4\,\mathrm{rad}$.

5.3 Altering the test and reference beam

After measurements for poor mode matching between both beams and the same EOM beam with medium sized waist across all measurements, this Section discusses measurements for good mode matching but different beam sizes. This is accomplished by moving the position of lens 2 as shown in Figure 16. With $z_{\text{lens2}} = (0.250 \pm 0.005)\,\text{m}$ we can create large, well collimated beams ($w_0 \approx 800\,\mu\text{m}$), and for $z_{\text{lens2}} = (0.596 \pm 0.004)\,\text{m}$ the resulting beams have a very small waist ($w_0 \approx 140\,\mu\text{m}$) and a large divergence.

5.3.1 Minimally divergent beams

The setup configuration with lens 2 at $z = (0.250 \pm 0.005)\,\text{m}$ creates large, well collimated laser beams with a flat wavefront close to 0 in front of the camera with the focii $w_{0,EOM} = (800 \pm 40)\,\mu\text{m}$ at $z_{0,\text{EOM}} = (1.46 \pm 0.10)\,\text{m}$ and $w_{0,\text{AOM}} = (810 \pm 50)\,\mu\text{m}$ at $z_{0,\text{EOM}} = (1.35 \pm 0.16)\,\text{m}$. The radial and wavefront evolution of this setup can be seen in Figure 50.

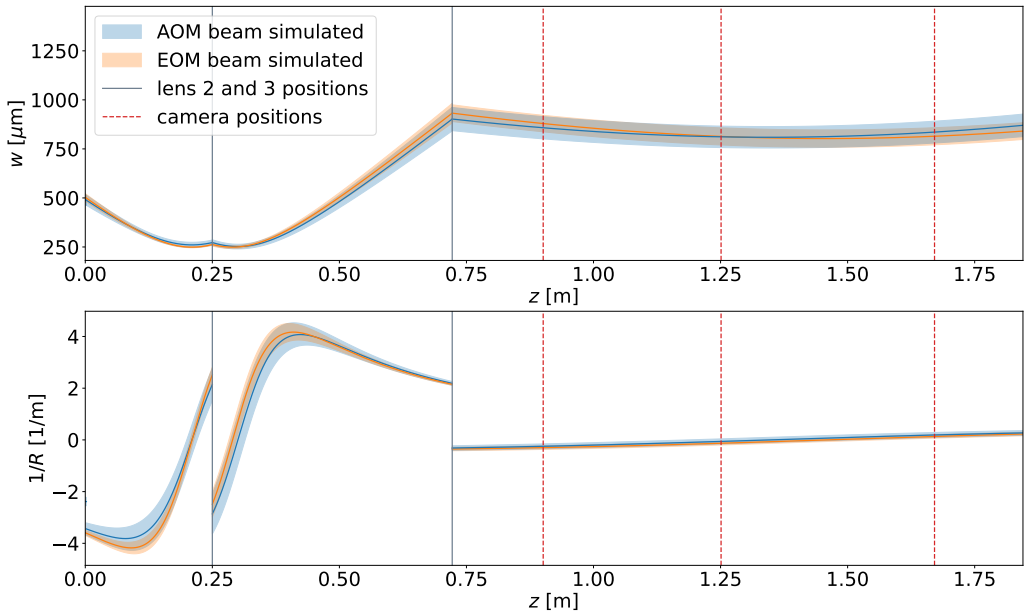

Figure 50: Beam radius $w(z)$ (top) and wavefront $1/R(z)$ (bottom) in the second coordinate system. With $z_{\text{lens2}} = (0.250 \pm 0.005)\,\text{m}$. The red lines indicate camera positions for measurements.

The camera positions marked in Figure **??** are $z = z_{\text{Piezo}} + 5.6\,\text{cm} = (0.901 \pm 0.008)\,\text{m}$ (left), which provides a negative wavefront, the position $z = z_{\text{Piezo}} + 40.6\,\text{cm} = (1.251 \pm 0.008)\,\text{m}$ (middle) is at the focus, and $z = z_{\text{Piezo}} + 82.6\,\text{cm} = (1.671 \pm 0.008)\,\text{m}$ provides a positive wavefront. For this setup, the recorded phase data, corresponding phase simulations, and the difference between both can be seen in Figure 51.

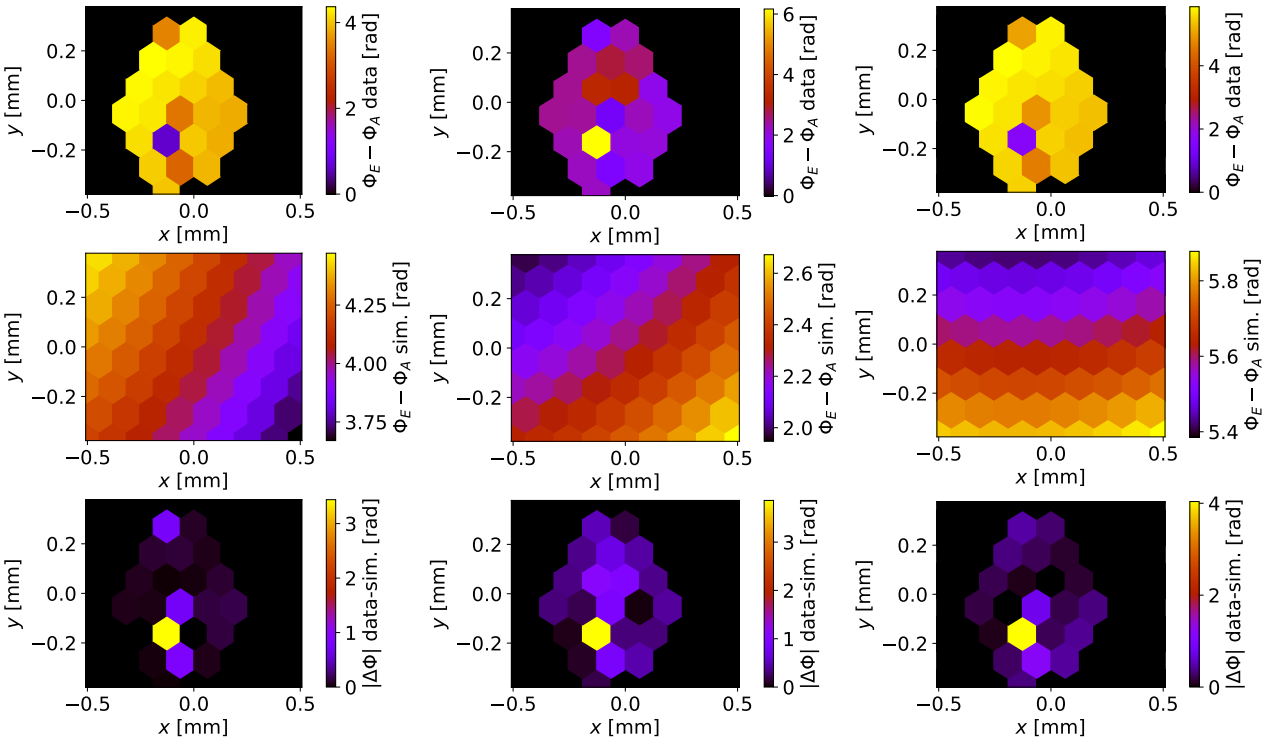

Figure 51: Recorded phase data (top) for $z_{\text{cam}} = z_{\text{Piezo}} + 5.6\,\text{cm}$ (left), $z_{\text{cam}} = z_{\text{Piezo}} + 40.6\,\text{cm}$ (middle), and $z_{\text{cam}} = z_{\text{Piezo}} + 82.6\,\text{cm}$ (right), as well as simulations (middle row), and difference $|\Delta\Phi| = |\delta\Phi_{\text{data}} - \delta\Phi_{\text{sim}}|$ for setup with lens 2 at $z = (0.250 \pm 0.005)\,\text{m}$.

With exception of the broken pixels 11, 26, and 52, and additionally pixel 43, there seems to be good correlation between the measurement on the left in Figure 51. The middle exhibits the worst correlation, which is not surprising because pixel 27 and 28 seem to have malfunctioned and thus the resolution is decreased. The right side however also does not provide good overlap between simulation and data, which is peculiar because radius w and wavefront $1/R$ at the measurement positions on the left and right are basically the same. In total, the differences between phase data and phase simulation from left to right is $(0.3 \pm 0.7)\,\text{rad}$, $(0.6 \pm 0.8)\,\text{rad}$, and $(0.5 \pm 0.8)\,\text{rad}$, $(0.25 \pm 0.8)\,\text{rad}$, $(0.6 \pm 0.8)\,\text{rad}$, and $(0.4 \pm 0.8)\,\text{rad}$ without pixels 11, 36, 52, and $(0.07 \pm 0.05)\,\text{rad}$, $(0.29 \pm 0.16)\,\text{rad}$, and $(0.21 \pm 0.12)\,\text{rad}$ additionally without pixel 43. For the middle, pixels 27 and 28 were also subtracted. The measurements in this part were conducted at the same time as the measurements in Section 5.1, where pixel 43 also doesn't work most likely because it's photodiode's power cable was dislodged. The discrepancy between the recorded data and phase simulation on the right of Figure 51 hints at an error in the acquisition of beam trajectories like positioning errors of the beam profiler during the trajectory measurements shown in Figure 73, or a positioning error of the fiber array when recording phase data for this particular measurement. The former would explain why the phase data recorded the closest to lens 3 and the final mirror on the left side of Figure 51 is the most accurate, because tilt errors have the least amount of impact there. The comparison of recorded data with simulations for a measurement set are done in unison. Usually the best results are obtained by performing comparison for the measurement point with the largest distance to the final mirror first, and the adjusting the best determined parameter values based on the measurement point in the middle, then the one closest to the mirror, and then reexamining the other two. If the fiber array was accidentally placed at a different position for the measurement on the right side of Figure 51 then this would also explain the discrepancy. Figure 52, Figure 53, and Figure 54 show the phase difference between AOM and EOM beam, and Figure 76 shows the measured trajectories of both beams.

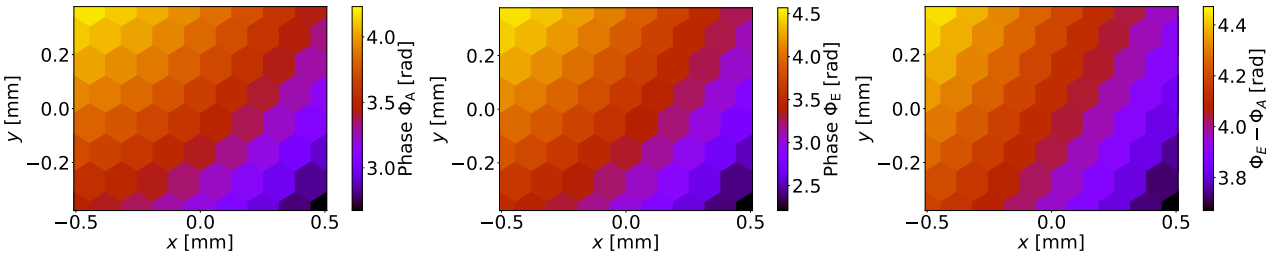

Figure 52: Phase simulations for EOM and AOM beam for lens 2 at $z = (0.250 \pm 0.005)\,\mathrm{m}$ at the measurement position $z_{\mathrm{cam}} = z_{\mathrm{Piezo}} + 5.6\,\mathrm{cm}$. Left: Phase of the AOM beam. Middle: Phase of the EOM beam. Right: Phase difference $\Phi_A - \Phi_E + lpo$ with $lpo = 3.135\,\mathrm{rad}$.

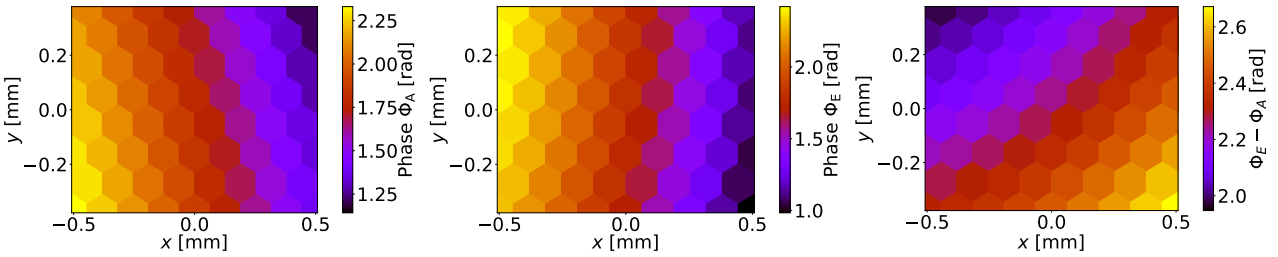

Figure 53: Phase simulations for EOM and AOM beam for lens 2 at $z = (0.250 \pm 0.005)\,\mathrm{m}$ at the measurement position $z_{\mathrm{cam}} = z_{\mathrm{Piezo}} + 40.6\,\mathrm{cm}$. Left: Phase of the AOM beam. Middle: Phase of the EOM beam. Right: Phase difference $\Phi_A - \Phi_E + lpo$ with $lpo = 2.273\,\mathrm{rad}$.

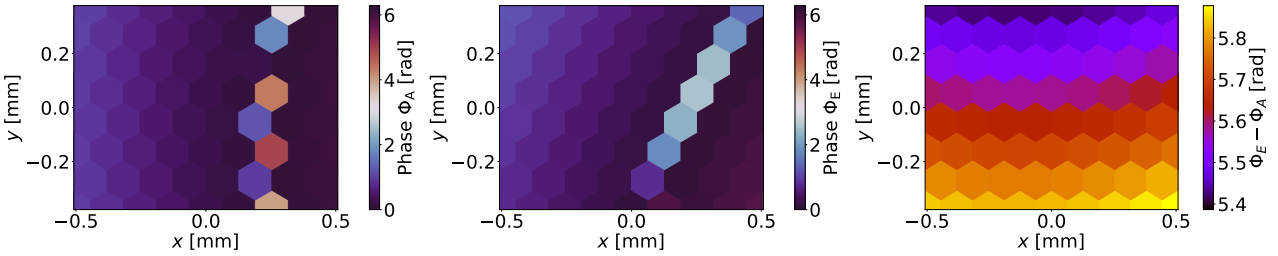

Figure 54: Phase simulations for EOM and AOM beam for lens 2 at $z = (0.250 \pm 0.005)\,\mathrm{m}$ at the measurement position $z_{\mathrm{cam}} = z_{\mathrm{Piezo}} + 82.6\,\mathrm{cm}$. Left: Phase of the AOM beam. Middle: Phase of the EOM beam. Right: Phase difference $\Phi_A - \Phi_E + lpo$ with $lpo = 5.639\,\mathrm{rad}$.

From the example calculations in Section 4.2, we can deduct that two very large, well collimated beams have a $\delta\Phi$ range in the camera surface that is very small and nearly constant over z. In Figure 52, Figure 53, and Figure 54 this range is $\approx 0.6\,\mathrm{rad}$ for all three positions on z. The same applies to the recorded phase data in the upper right plot in Figure 51. The possibility of an error having occurred during the beam trajectory measurement is thus very likely, considering that the data-simulation discrepancy seems to originate predominantly from the difference of shapes of the two phase difference profiles.

5.3.2 Highly divergent beams

The second setup places lens 2 at $z = (0.596 \pm 0.004)\,\mathrm{m}$. This creates a very small focus with $w_{0,\mathrm{EOM}} = (142 \pm 4)\,\mu\mathrm{m}$ at $z_{0,\mathrm{EOM}} = (0.872 \pm 0.004)\,\mathrm{m}$ and $w_{0,\mathrm{AOM}} = (146 \pm 7)\,\mu\mathrm{m}$ at $z_{0,\mathrm{AOM}} = (0.873 \pm 0.004)\,\mathrm{m}$. Radius $w(z)$ and wavefront $1/R(z)$ of this configuration is shown in Figure 55.

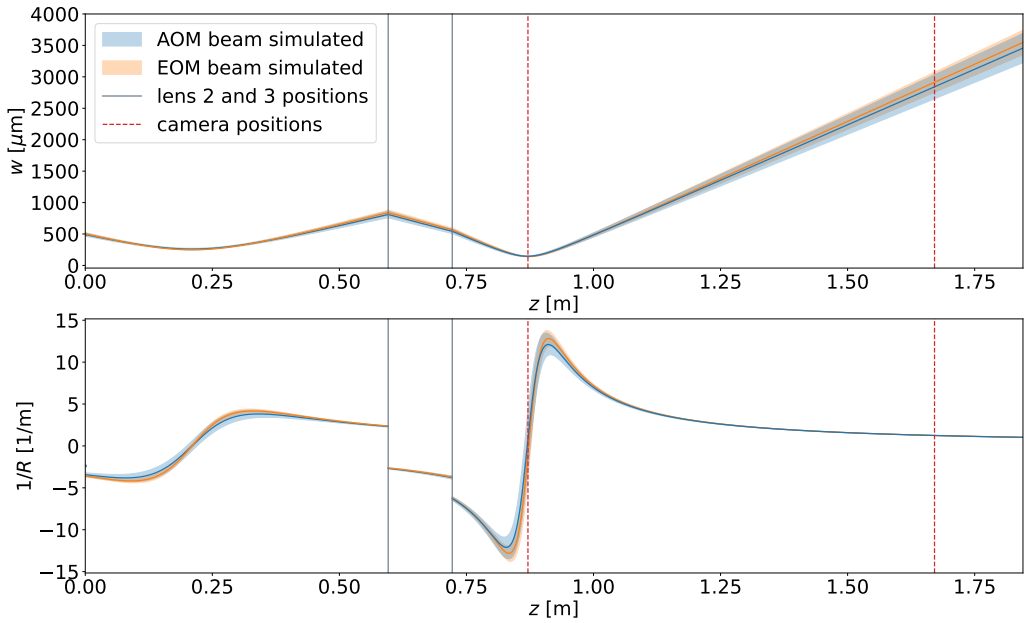

Figure 55: Beam radius $w(z)$ (top) and wavefront $1/R(z)$ (bottom) in the second coordinate system. With $z_{\text{lens2}} = (0.596 \pm 0.004)\,\text{m}$. The red lines indicate camera positions for measurements.

The combined laser beam shown in Figure 55 has a small focus and thus a stark curvature. Two positions were used for recording data. One close to the focus, at $z_{\text{cam}} = z_{\text{Piezo}} + 2.6\,\text{cm}$, and the other at $z_{\text{cam}} = z_{\text{Piezo}} + 82.6\,\text{cm}$, where the beam is very large. The results of these measurements and the comparison of the recorded data with phase simulations can be seen in Figure 56.

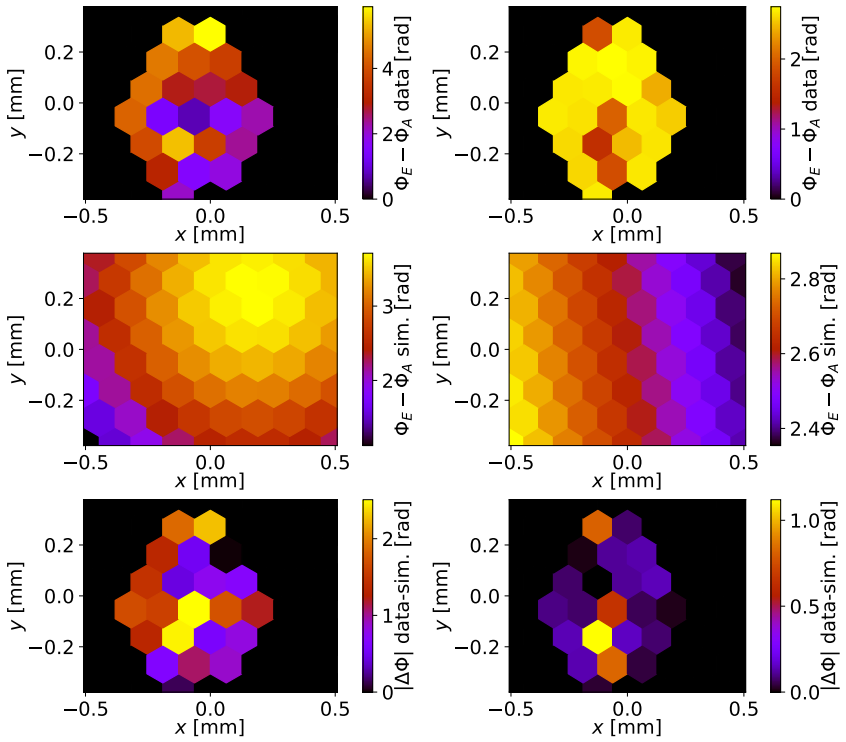

Figure 56: Recorded phase data (top) for $z_{\text{cam}} = z_{\text{Piezo}} + 2.6\,\text{cm}$ (left), and $z_{\text{cam}} = z_{\text{Piezo}} + 82.6\,\text{cm}$ (right), as well as simulations (middle row), and difference $|\Delta\Phi| = |\delta\Phi_{\text{data}} - \delta\Phi_{\text{sim}}|$ for setup with lens 2 at $z = (0.596 \pm 0.004)\,\text{m}$.

The phase measurements in Figure 56 seem to correlate well with simulations only where the beams are large. The difference between data and theory from left to right is $(1.2 \pm 0.7)\,\text{rad}$, and $(0.2 \pm 0.3)\,\text{rad}$ unmodified, $(1.1 \pm 0.7)\,\text{rad}$ and $(0.14 \pm 0.24)\,\text{rad}$ without pixels 11, 36, and 52, and $(1.0 \pm 0.6)\,\text{rad}$ and $(0.09 \pm 0.05)\,\text{rad}$ additionally without pixel 43. While the latter fits with acceptable accuracy, the former does not seem accurate at all. The recorded shape in the top left of Figure 56 seems highly chaotic. While this may be another sign of poor accuracy at beam foci, it could also be the result of a high tilt angle between beam trajectory and camera surface. Even though camera angles α_x and α_y do not affect the shape of the phase difference between two beams in principle, the fiber array exhibits a maximum angle $\approx 10° - 14°$ where light can couple into the fibers. Since the beam for this measurement is very small, it is difficult to locate with the live plotter of the phase camera. This measurement position also carries close proximity to the final mirror, where beam trajectory can be adjusted. It is possible that when trying to align the beam onto the fiber array, a large tilt was created, since at this distance from the mirror, tilts only marginally translate to positional offsets. As before, Figure 52, Figure 57, and Figure 58 show the phase difference between AOM and EOM beam, and Figure 77 the measured trajectories of both beams.

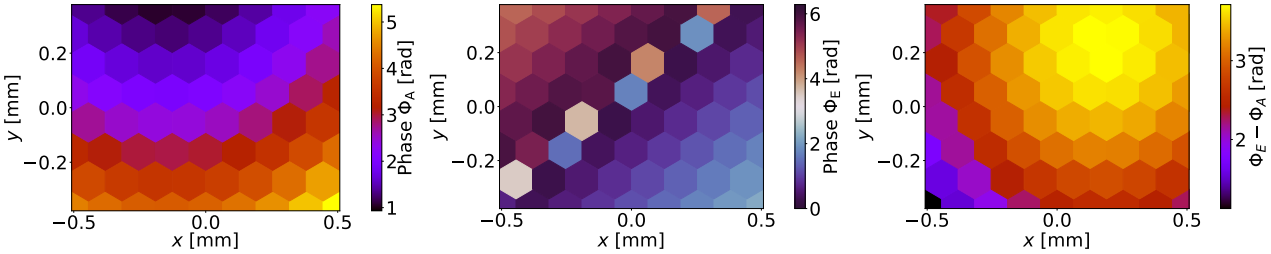

Figure 57: Phase simulations for EOM and AOM beam for lens 2 at $z = (0.596 \pm 0.004)\,\mathrm{m}$ at the measurement position $z_{\mathrm{cam}} = z_{\mathrm{Piezo}} + 2.6\,\mathrm{cm}$. Left: Phase of the AOM beam. Middle: Phase of the EOM beam. Right: Phase difference $\Phi_A - \Phi_E + lpo$ with $lpo = 5.442\,\mathrm{rad}$.

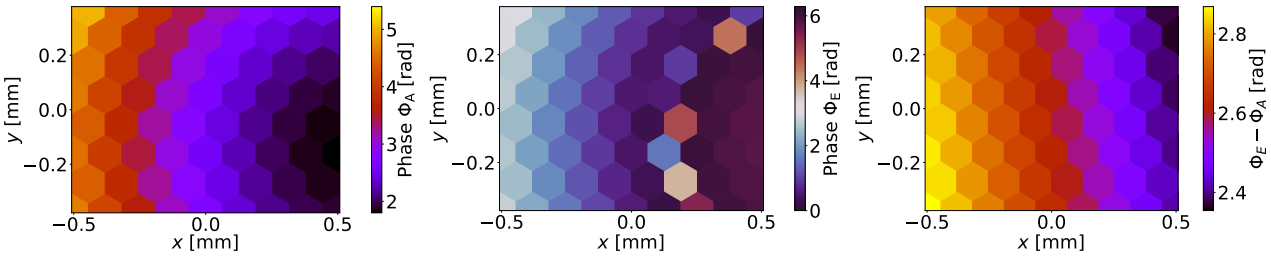

Figure 58: Phase simulations for EOM and AOM beam for lens 2 at $z = (0.596 \pm 0.004)\,\mathrm{m}$ at the measurement position $z_{\mathrm{cam}} = z_{\mathrm{Piezo}} + 82.6\,\mathrm{cm}$. Left: Phase of the AOM beam. Middle: Phase of the EOM beam. Right: Phase difference $\Phi_A - \Phi_E + lpo$ with $lpo = 4.744$.

Phase difference ranges on the camera surface between two small beams are expected to start out large and then diminish with distance z. While this is shown on the right side of Figure 57 and Figure 58 with $\approx 4\,\mathrm{rad}$ and $\approx 0.45\,\mathrm{rad}$, the faulty measurement on the top left in Figure 56 renders confirmation challenging, even though the displayed range is also large ($\approx 5\,\mathrm{rad}$).
Overall it seems that the phase differences for configurations with large beams present are the easiest to resolve, which is expected. In contrast, there are no measurements at beam foci where recorded data and simulations show good overlap. There are hints of accuracy being inversely proportional to difference in wavefront $|R_1^{-1} - R_2^{-1}|$. The perceived accuracy also decreases significantly, the more pixels don't work properly. It is thus crucial to ensure the proper function of all pixels before taking measurements going forward, and to work towards fixing the problem of the three permanently defective pixels.

6 Conclusion

An optical setup that provides the functionality desired for the 2D phase camera was successfully constructed. The laser beam's parameters can be tracked through the entire setup with the methods explained in Section 2.4. Combined with a python script providing a graphical interface for simulations of 2D phase and intensity profiles of two overlapping beams, phase data recorded with the phase camera can be directly compared with expectations according to theory by manually adjusting parameter sliders with ranges of $\pm$ the standard derivation of the parameter in question. Simulations show that the phase camera is able to measure the phase of beam configurations well, that include one or more large beams, but has problems resolving configurations with smaller beams. This matches expectations. At beam foci, no good overlap between phase data and simulations could be found thus far. Additionally, low wavefront difference between the test and reference beams might yield more accurate results, but due to a limited amount of data, this can not be confirmed at this point. Simulations conducted with the graphical interface are limited by certain systematic and statistical errors laid out in Section 3.1 such as inaccurate technical stats of optical components, or inaccurate measurement tools such as the WinCamD-LCM-TEL used for beam profiling, which can only detect the wavelength 1550 nm through a workaround method that introduces inaccuracy at small beam sizes. Additionally it displays an unexpected dependency of the measured beam size w on laser power P. This specific issue in general is a substantial limiting factor for constructing accurate phase simulations because it means that the exact shape of the laser beam can not be determined to verify the correctness of the beam trace calculations that act as a basis for phase simulations. Determining the accuracy of phase measurements is also limited by the low spacial resolution of the phase camera, as there are only 22 of 64 pixels in use at the moment. Additionally the phase camera possesses systematic errors such as three permanently defect pixels, and other pixels that may temporarily seize functionality. The latter sometimes occurs when power cables of photodiodes dislodge due to the presence of incompatible cable ports. This problem can be avoided by simply verifying that there is current running through the photodiodes attached to each pixel or by replacing the cable ports. Sometimes however, pixels malfunction for reasons that are not yet discovered. As a proof of concept however, the phase camera works.

Acronyms

GW gravitational waves

ET Einstein Telescope

CE Cosmic Explorer

NS neutron star

BH black hole

GR general relativity

CW continuous gravitational waves

LIGO Laser Interferometer Gravitational-Wave Observatory

GWB gravitational wave background

BS beamsplitter

HF high frequency

LF low frequency

QRPN quantum radiation pressure noise

SN shot noise

CS coordinate system

AOM acousto-optic modulator

EOM electro-optic modulator

A Appendix

A.1 Technical stats

Table 1: Laser test condition from the test report by Connet.

	Specifications
Power Supply	$100 \sim 240$VAC
Ambient Temperature	25°
Environment Humidity	$< 90\%$
Warm-up Time	< 30 min

Table 2: Results from the Laser test report by Connet.

Parameters	**Unit**	**Specifications**			**Results**
		Min	**Typ.**	**Max**	
Center Wavelength	nm	1549.970	1550.120	1550.270	**1550.141**
Output Power	mW	10	-	200	200
Monitor	mW	-	-	-	0.16
Side Mode Suppression Ratio (SMSR)	db	50	-	-	61.47
Beam Quality M2		-	-	1.1	<1.1
PER	dB	20			21
Peak Frequency of Relaxation Oscillation	kHz	200	-	700	365
RIN Level@peak	dB/Hz	-	-	-105	-111.7
Wavelength Thermal Tunging Range	nm	-	0.3	-	0.3
Operation Temperature	°C	0	-	50	Pass
Storage Temperature	°C	-40	-	85	Pass

Table 3: AeroDIODE 1550-AOM-1 Factory Report.

AOM P/N.:	1550-AOM-1	AOM S/N.:	2624DC
Driver P/N.:	RFAOM-A-80	Driver S/N.:	2483DF

Test Conditions	
Laser	DFB
Laser Wavelength	1550 nm
Laser Power	20 mW
RF Frequency	80 MHz
RF Power	2.5 W
RF Working Voltage	24 V
RF Working Current	320 mA

Test Results	
Insertion Loss	1.7 dB
Extinction Ratio (1st order on/off)	58 dB
Polarization Extinction Ratio	22 dB
Fiber Type	PM1550
Connector	FC/APC
Rise/Fall Time	45 ns
Digital Input	Standard TTL

Table 4: Specs of the PM1550 fiber built into the 1550-AOM-1.

Wavelength (nm)	1550
Mode-field Diameter (µm)	10.5 ± 0.5
Beat Length Range (mm)	3.0-5.0
Maximum Cross Talk at 100 m (dB)	-30
Typical Cross Talk at 4 m (dB)	
Cutoff Wavelength (nm)	1300-1440
Maximum Attenuation (dB/km)	0.5

Table 5: All optical components used in the laser setup (see Section 3).

Component	**type**	**Manufacturer**	**Coating**
ADAFCPMB4	Mating Sleeve	Thorlabs	
P3-1550PM-FC-1 [39]	PM fiber	Thorlabs	
IO-4-1550-VLP [40]	Faraday isolator	Thorlabs	
PM7 – SWIR1_10	EOM	QUBIG	
1550-AOM-1	AOM	AeroDIODE	
RFAOM-A-80	AOM driver	AeroDIODE	
TC12APC-1550 [43]	Triplet Collimator	Thorlabs	AR-C (1050 – 1650 nm)
BB1-E04 [50]	planar mirror	Thorlabs	E04 (1280 – 1600 nm)
BSW29 [45]	beamsplitter	Thorlabs	(600 – 1700 m)
LA1908-C [44]	plano-convex lens	Thorlabs	AR-C (1050 – 1650 nm)
LD1464-C [47]	bi-concave lens	Thorlabs	AR-C (1050 – 1650 nm)
LB1676-C [48]	bi-convex lens	Thorlabs	AR-C (1050 – 1650 nm)
LC1582C [44]	plano-convex lens	Thorlabs	AR-C (1050 – 1650 nm)
KPX119AR.18 [49]	plano-convex lens	Newport	AR.18 (1000 – 1550 nm)
LA1708-C [44]	plano-convex lens	Thorlabs	AR-C (1050 – 1650 nm)
LA1172-C [44]	plano-convex lens	Thorlabs	AR-C (1050 – 1650 nm)

A.2 Laser power across the optical setup

The evolution of the laser power P in in CS 1 and CS 2 is shown in Figure 59 and Figure 60. Jumps mark locations of optical elements. The values were obtained through successive measurements with a power meter.

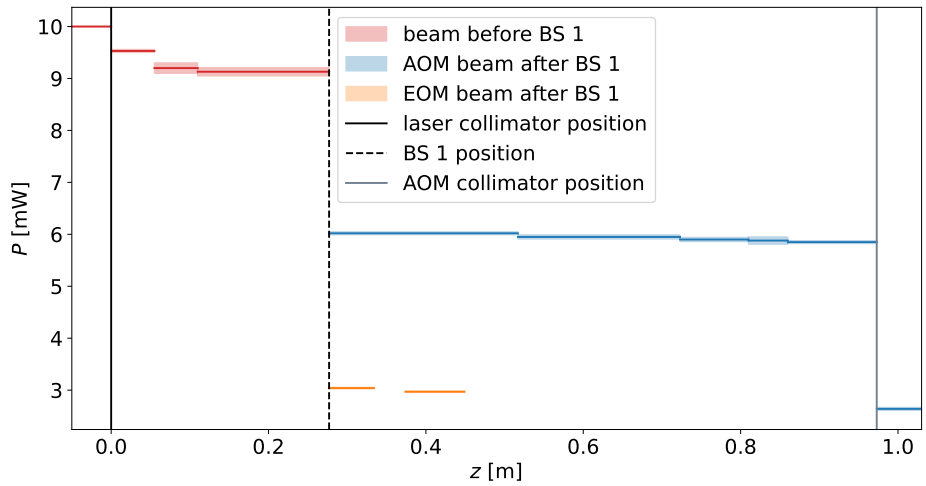

Figure 59: Power evolution of the laser beam and it's different paths through CS 1 set around the position of the laser output collimator at $z = 0$. The gap in the EOM path represents the 4 cm within the EOM. The EOM path in this plot ends at the location of BS 2 in CS 1 coordiantes. The location of the AOM beam behind the AOM collimator is arbitrary since it is behind the fiber and is the power that reaches the AOM.

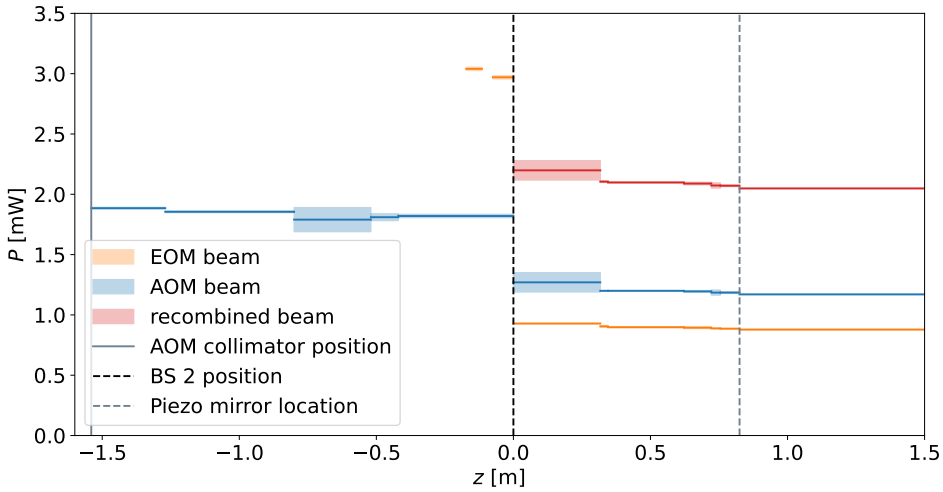

Figure 60: Power evolution of the laser beam and it's different paths through CS 2 set around the position of BS 2 at $z = (0.000 \pm 0.005)$ m. The gap in the EOM path represents the 4 cm within the EOM. The EOM path in this plot starts at the location of BS 1 in CS 2 coordinates. Shown post BS 2 are both the power of the total recombined beam as well as the power of the EOM and AOM beam sections.

A.3 Erroneous laser setup plots

This Section compiles the plots that describe the initial design of the optical setup before the issues discussed in Section 3.1 were discovered.

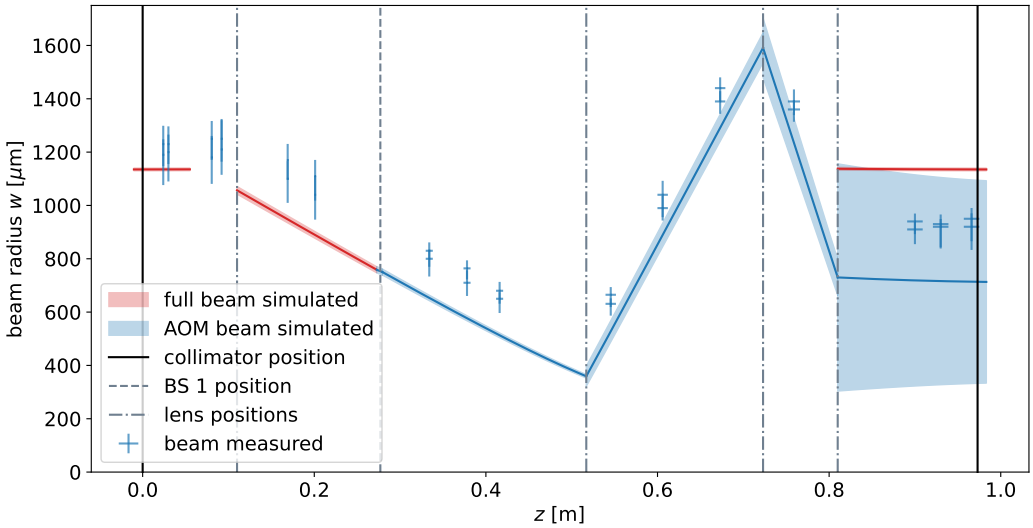

Figure 61: Beam radius $w(z)$ in the first coordinate system. The simulations are based on the initial design and are faulty, which is part of the reason why there is a discrepancy with the measured values. The measured values contain the mean and range (lowest to highest measured value) of both major and minor beam axes because of the unresolved systematic error with the beam profiler (see Section 3.1.2). This plot does not contain the EOM beam, which past the BS has the same shape as the AOM beam. The gap on the left side in the full beam simulation represents the space between the O-4-1550-VLP - Free-Space Isolator and the first lens, where the radius can't be simulated. The shape of the section between this lens and the BS is based on measurements of this beam section's waist. The red section on the right represents the shape that the beam would need to have for perfect mode matching, which is the exact same shape as produced by the output collimator on the right.

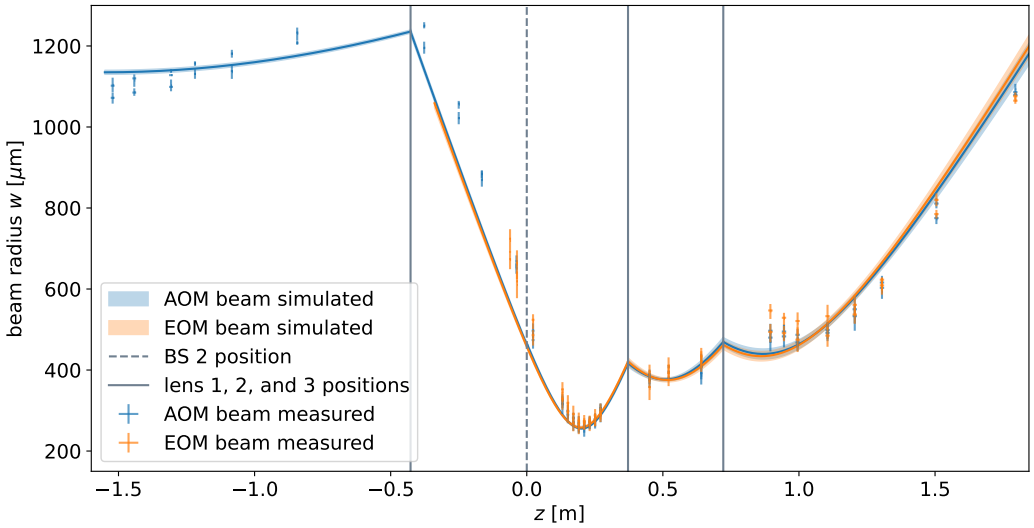

Figure 62: Beam radius $w(z)$ in the second coordinate system with $z_{\text{lens2}} = (0.372 \pm 0.004)\,\text{m}$. The simulations are based on the initial design and are faulty, which is part of the reason why there is a discrepancy with the measured values. The measured values contain the mean and range (lowest to highest measured value) of both major and minor beam axes because of the unresolved systematic error with the beam profiler (see Section 3.1.2).

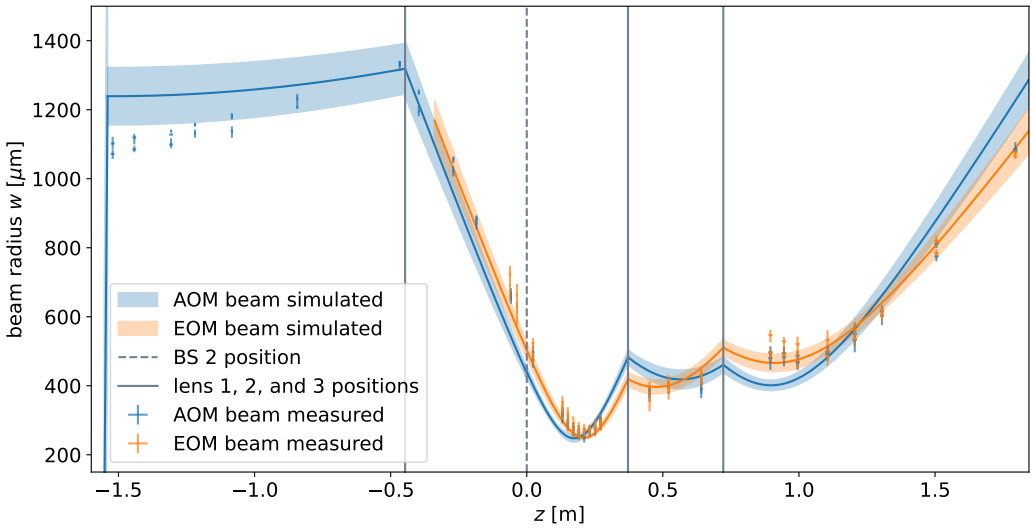

Figure 63: Beam radius $w(z)$ in the second coordinate system after adjusting for statistical errors, with $z_{\text{lens2}} = (0.372 \pm 0.004)\,\text{m}$. The measured values contain the mean and range (lowest to highest measured value) of both major and minor beam axes because of the unresolved systematic error with the beam profiler (see Section 3.1.2). As seen, calculations and measurements still don't correlate well.

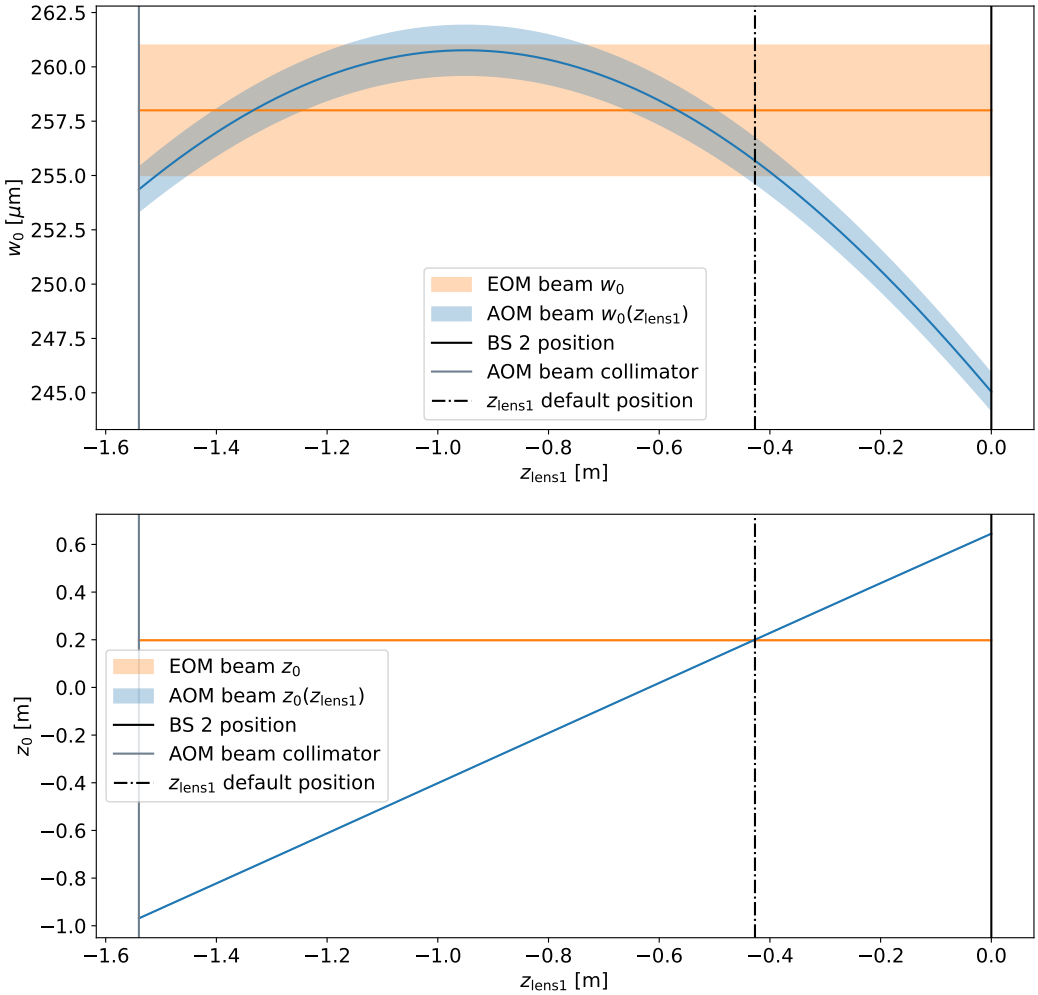

Figure 64: Waist w_0 (top) and waist position z_0 (bottom) of the AOM beam created by lens 1 depending on its position on the optical axis z. The simulations are based on the initial design and are faulty. The best position indicates where EOM and AOM beam perfectly overlap in both plots. The EOM beam parameters in these plots are static, as lens 1 is located in the AOM beam path.

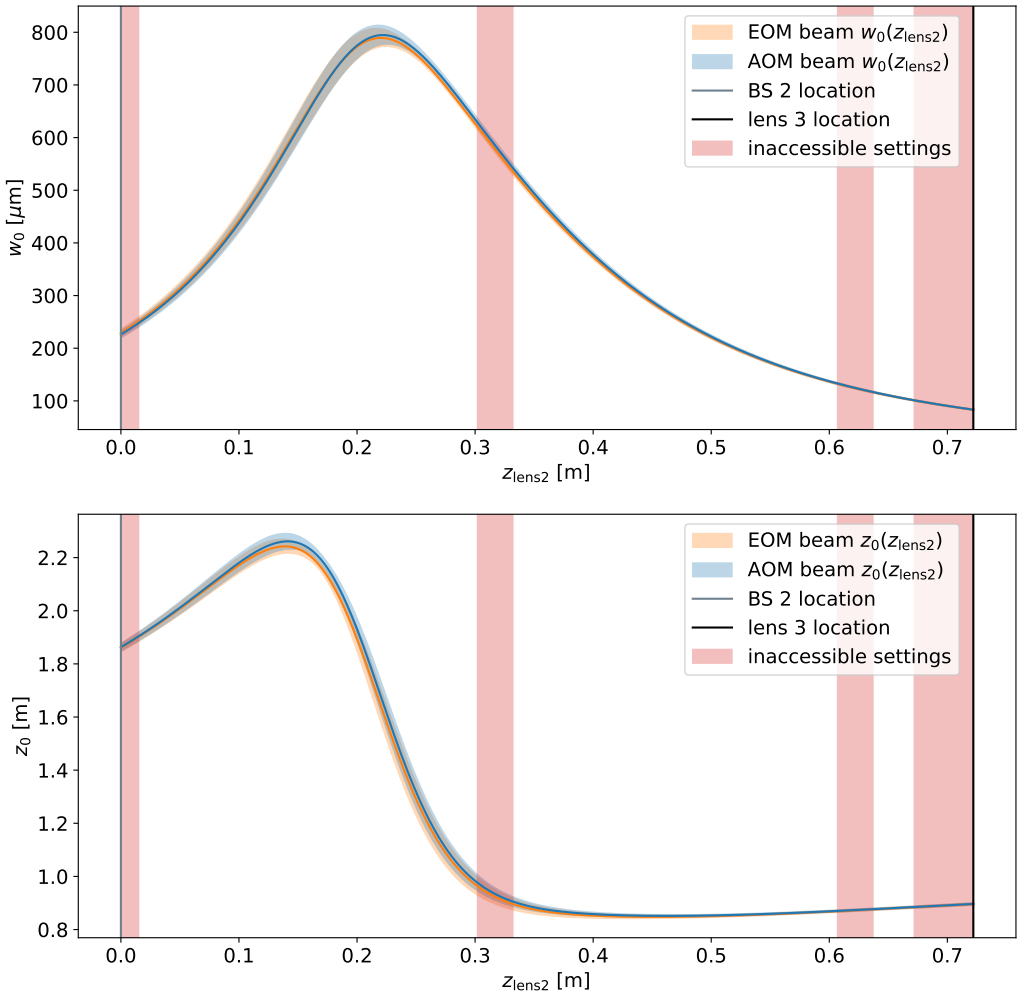

Figure 65: Achievable waist sizes w_0 dependent on the position of lens 2 on the optical axis. Top: Waist sizes w_0. Cottom: related waist positions z_0. These are $z_{\text{BS2}} \pm 1.5\,\text{cm}$, $z_{\text{mirror1}} \pm 1.5\,\text{cm}$, $z_{\text{mirror1}} \pm 1.5\,\text{cm}$, and $z_{\text{lens3}} - 5\,\text{cm}$. The simulations are based on the initial design and are faulty.

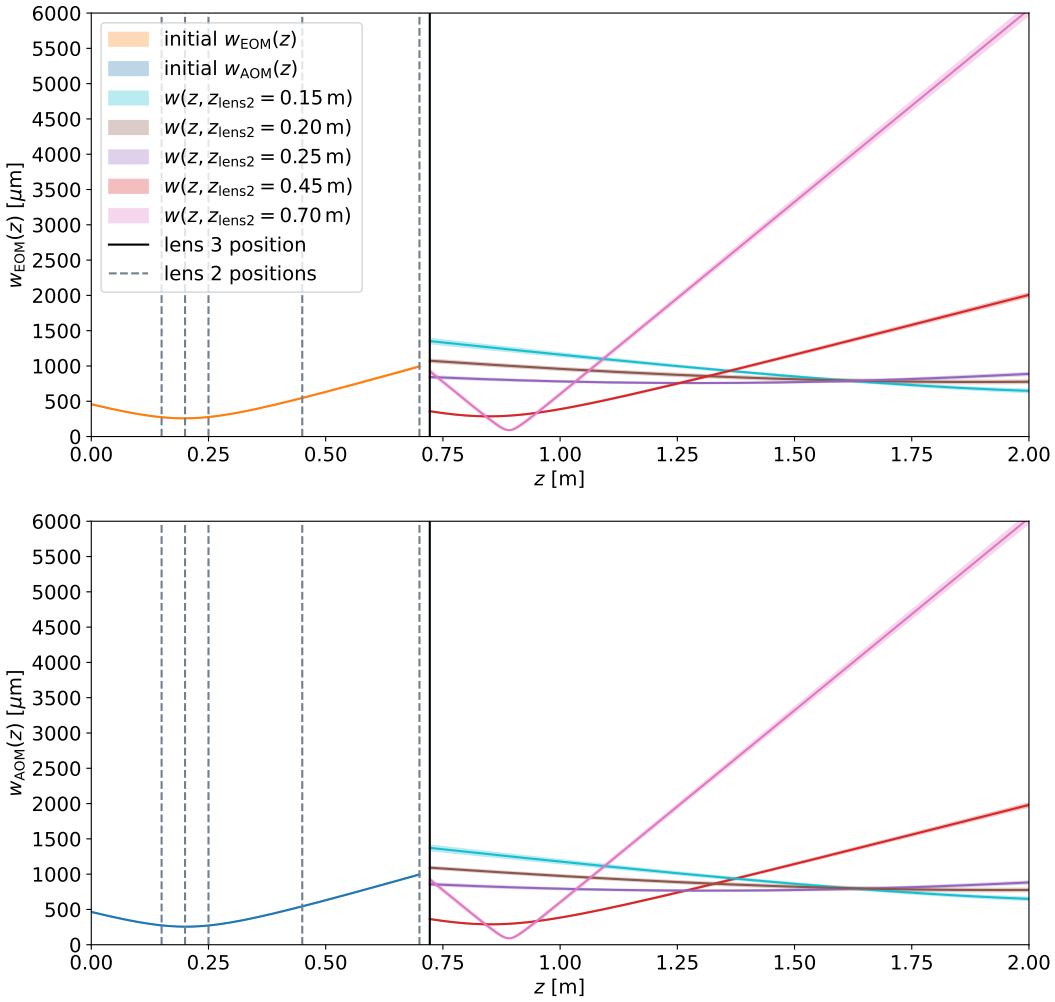

Figure 66: Beam radii in the camera range for five different positions of lens 2. Top: EOM beam. Bottom: AOM beam. The simulations are based on the initial design and are faulty.

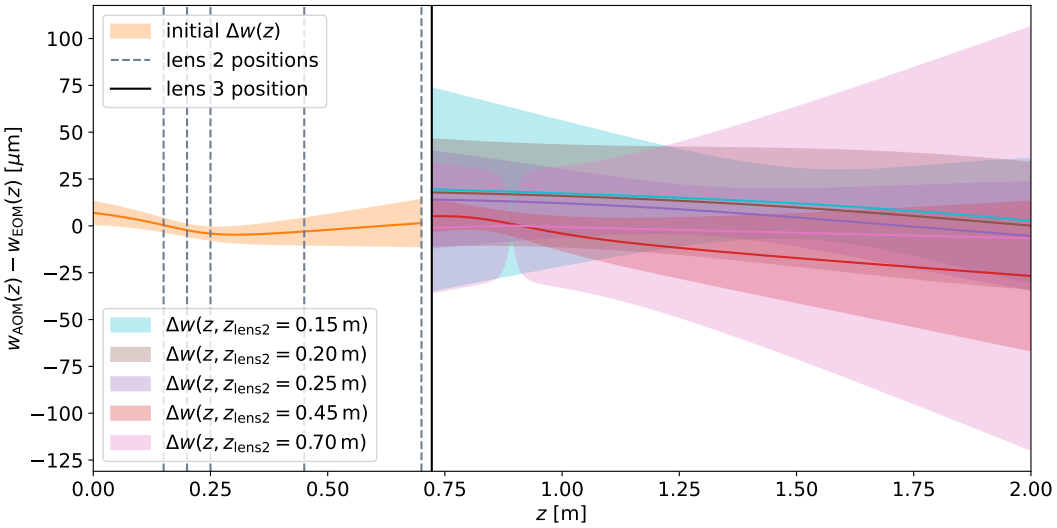

Figure 67: Radial difference between the beam radius of the AOM and EOM beam in the settings shown in Figure 66. The simulations are based on the initial design and are faulty.

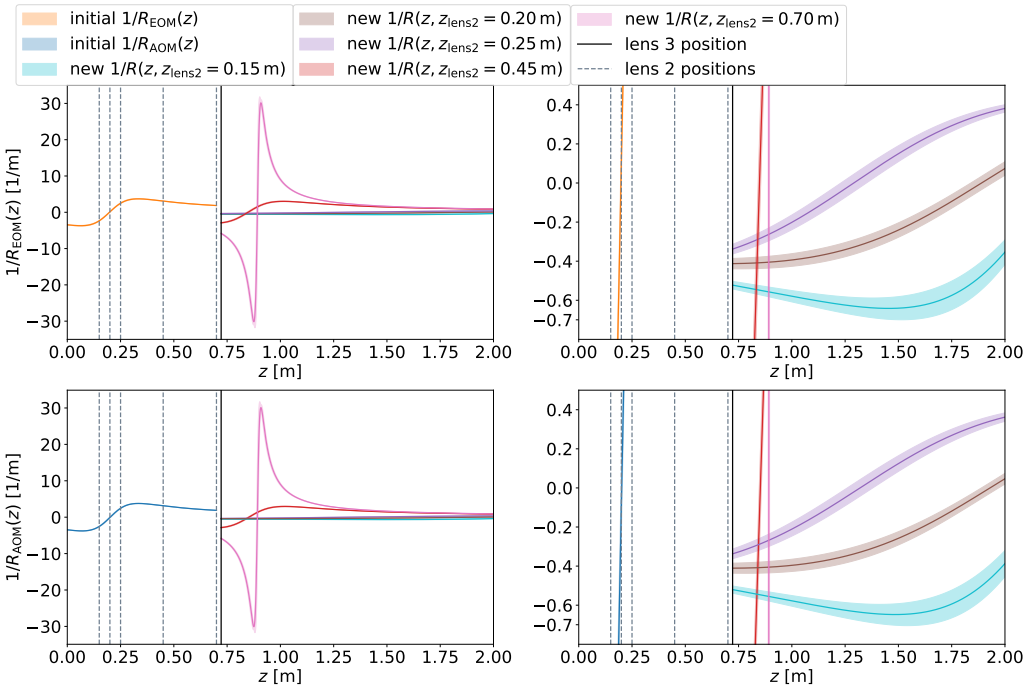

Figure 68: Wavefronts $1/R(z)$ in the camera range for five different positions of lens 2. Top: EOM beam. Bottom: AOM beam. The simulations are based on the initial design and are faulty. The plots on the right are the same as on the left but zoomed in.

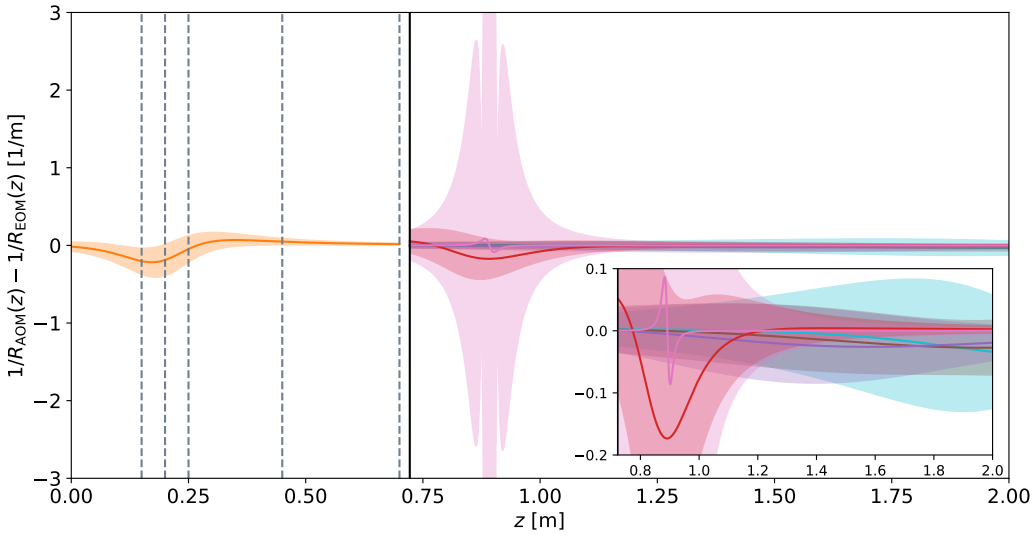

Figure 69: Wavefront difference between the beam radius of the AOM and EOM beam in the settings shown in Figure 68. The pink std band in the top plot extends to $\pm 20\,\mathrm{m}^{-}1$. The simulations are based on the initial design and are faulty.

A.4 Graphical interface

The plots on the top of Figure 70 show intensity profiles of both beams (left AOM, middle EOM) and the beam that is created by overlapping them (right). The middle row plots display the intensity from above but only in 1D. The grey positional sliders can be used to move to different positions on the camera plane for this. The plots at the bottom of Figure 70 show the phase profiles of the two beams on the left and middle, and the difference $\Phi_A - \Phi_E$ between both on the right. The beam parameter sliders (blue for AOM beam and orange for EOM beam) can then be adjusted between the upper and lower end of a parameter's standard derivation. The black sliders are there to adjust position z, tilts α_x and α_y, and offsets d_{Cx}, d_{Cy} (see Section 2.4.7) of the camera chip in $x-$ and $y-$direction, and the two grey sliders "x" and "y" for adjusting the position of the vertical and horizontal lines in the top plots, that act as axes for the plots in the middle. Pressing the Center buttons moves both to the center of one of the beams. An additional slider applies a linear phase offset (lpo) to the phase difference between both beams. This is done because the linear phase term changes drastically dependent on exact position on z, as illustrated in Figure 23. Hence it is practically impossible to match the absolute phase value of simulations with measurements. This is irrelevant for the 2D shape of the phase profile however, thus the *lpo* value can simply be increased/decreased to bridge the gap between recorded phase data and phase simulations.

In order to match phase data and phase simulations, the interface includes the compare function. By pressing the compare button, a separate window opens which is shown in Figure 71, that displays plots of the recorded intensity (left) and phase data (right) in the top row, corresponding simulations in the middle, and the differences $|I_{\mathrm{data}} - I_{\mathrm{sim}}|$ and $|\Phi_{\mathrm{data}} - \Phi_{\mathrm{sim}}|$ at the bottom. By adjusting the sliders, the best overlap between data and simulations can then be found manually. There was an attempt to create a feature that fits simulation parameters to data sets in order to automate this process. Due to the large amount of different parameters and the multidimensionality in how parameter changes affect resulting intensity and phase shapes, the fit feature, that is initiated when pressing the fit button in shown Figure 70, didn't yield any useful result and was abandoned due to time constraints.

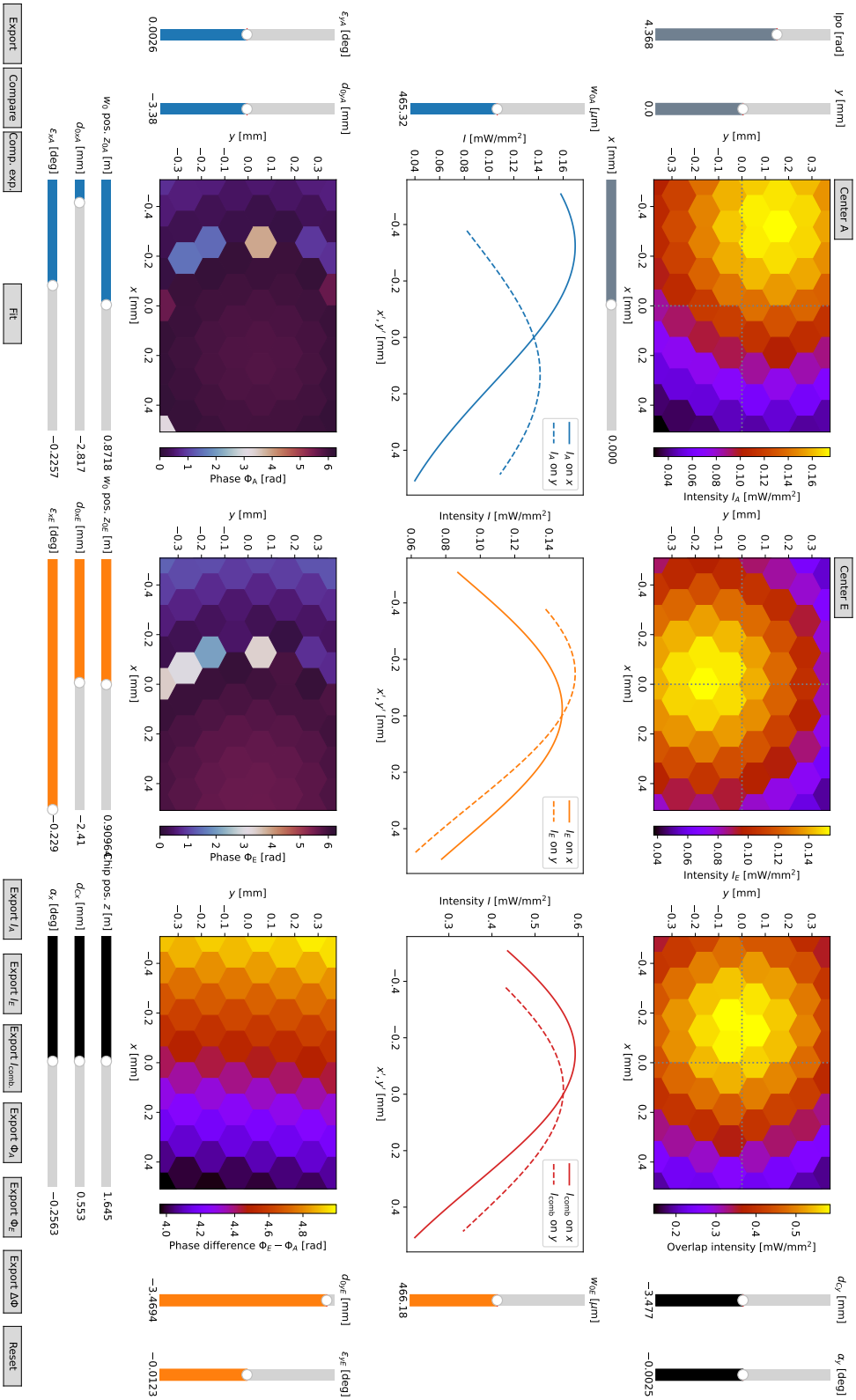

Figure 70: Graphical interface for phase simulations (Figure rotated by 90° to the right). Top: 2D intensity of AOM beam (left), EOM beam (middle) and of combined beam (right). Middle: Same as on top but 1D. Bottom: 2D simulated phase of AOM beam (left), EOM beam (middle) and phase difference (right). Color coded sliders are for parameter adjustments (blue: AOM beam, orange: EOM beam, black: camera).

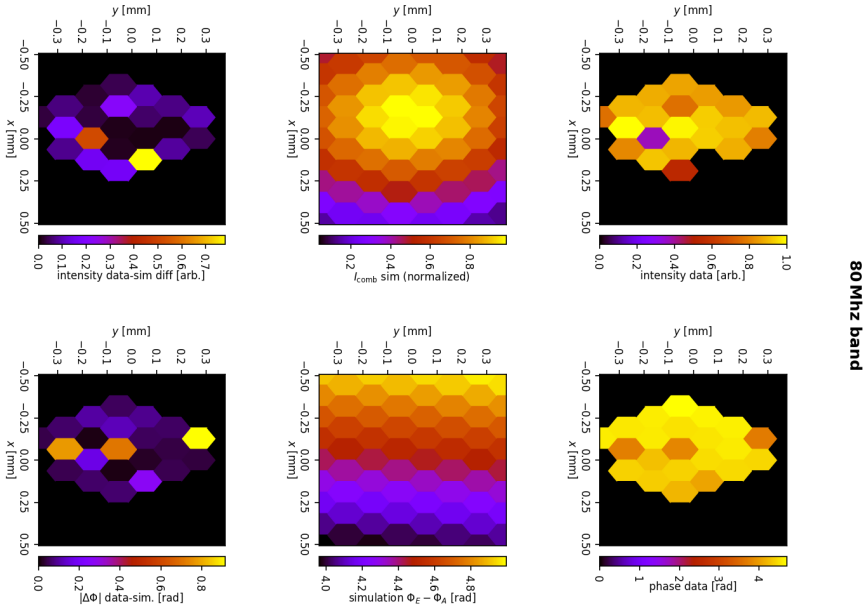

Figure 71: Compare function of the graphical interface (Figure rotated by 90° to the right). Top: Recorded intensity (left) and phase data (right). Middle: Corresponding simulations. Bottom: Difference between data and simulation.

After matching simulation to recorded phase and intensity data as best as possible, the Export buttons can be used to individually export the displayed intensity and phase plots. This will not only export the hexbin plots with 64-pixel resolution, but also high resolution plots (with $10^2 \times 10^2$ pixels). The data-simulation comparison can also be exported by pressing the Compare export button. Figure 72 shows an example of an exported high and low resolution intensity and phase profile.

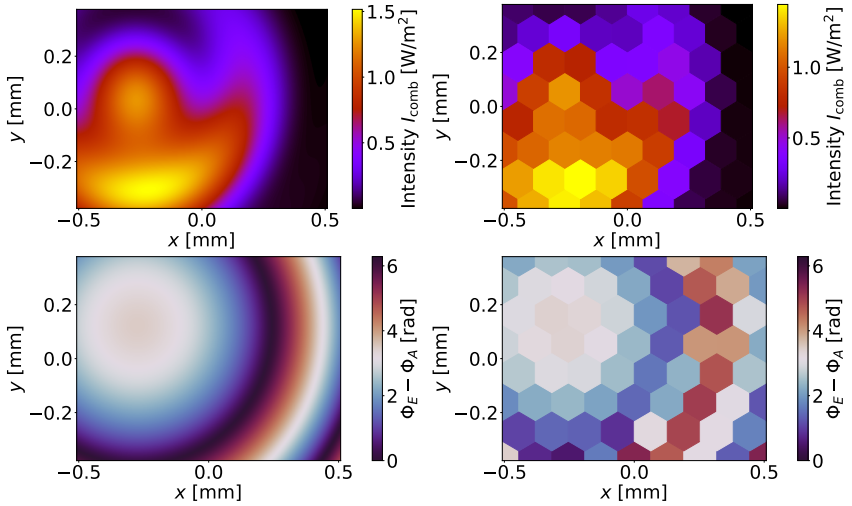

Figure 72: Top: Intensity. Bottom: Phase difference $\Phi_E - \Phi_A$. Left: High resolution. Right: Low (64 pixel) resolution. This example shows one of the beams measured in Section 5.2.3.

A.5 Beam trajectory measurements

This section compiles the results of the measurements for beam trajectories on the camera range that are used for phase measurements in Section 5. The acquired angles and offsets have high errors because the beam profiler is manually moved on a rail. While uncertainties in beam profiler positions on z are negligible, errors in $x-$ and $y-$direction can be large as the profiler has to be fixed with a screw by hand. As a consequence, minimal deviations in applied force can lead offsets of up to 100 µm. Hence the large std range and occasional symmetrical position jumps in Figure 73, Figure 74, Figure 75, Figure 76, and Figure 77 below.

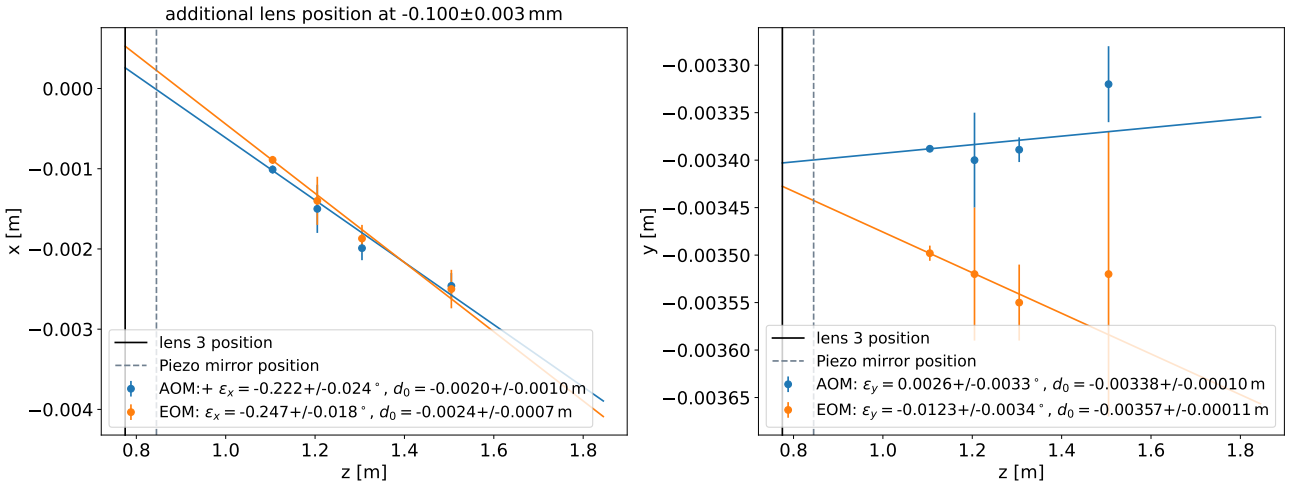

Figure 73: Measured beam trajectories for the phase measurements in Section 5.2.2.

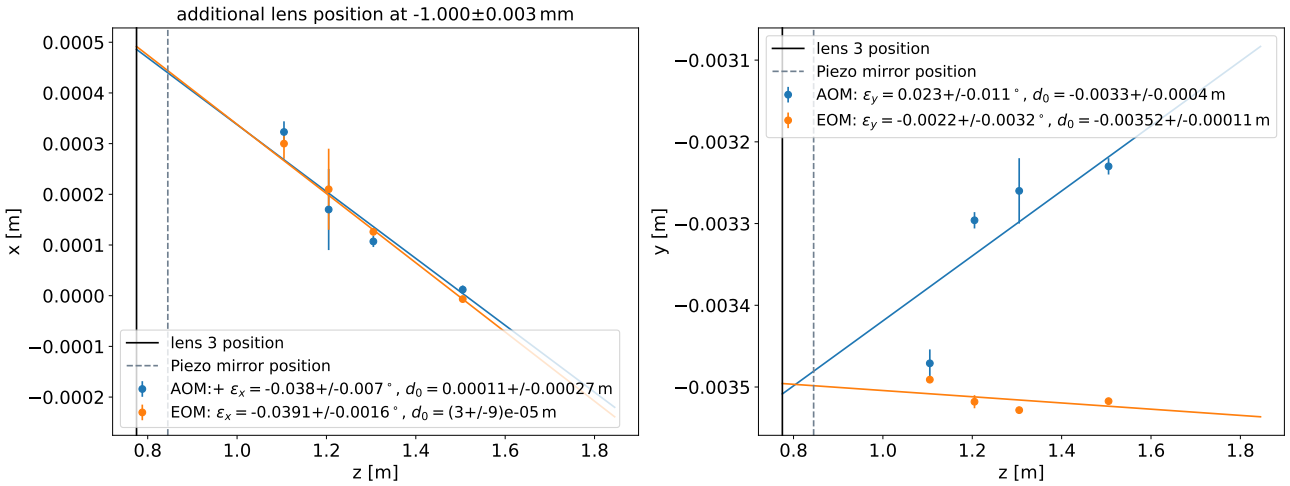

Figure 74: Measured beam trajectories for the phase measurements in Section 5.2.3.

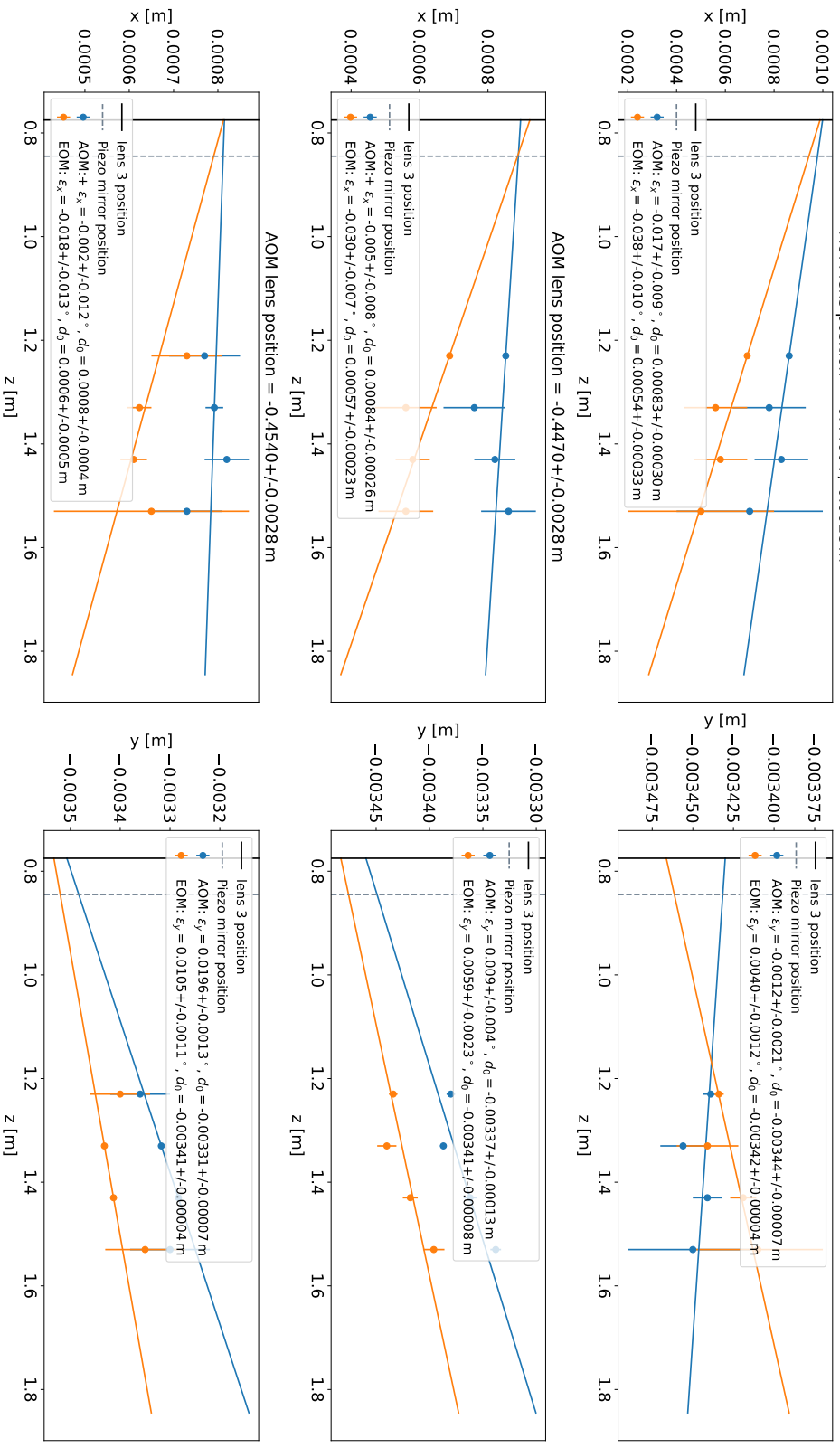

Figure 75: Measured beam trajectories for the phase measurements in Section 5.2.1.

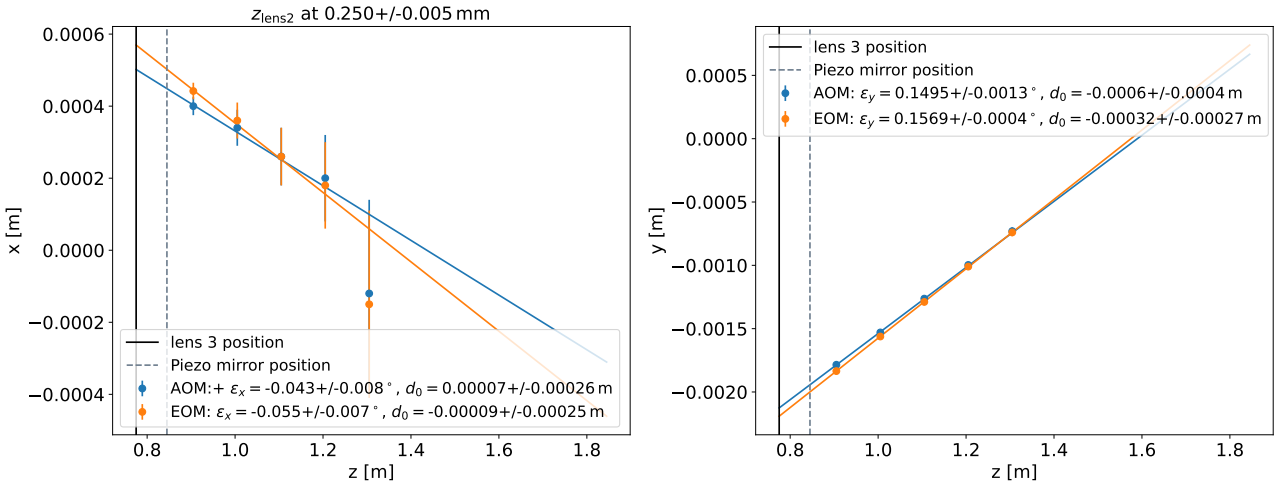

Figure 76: Measured beam trajectories for the phase measurements in Section 5.3.1.

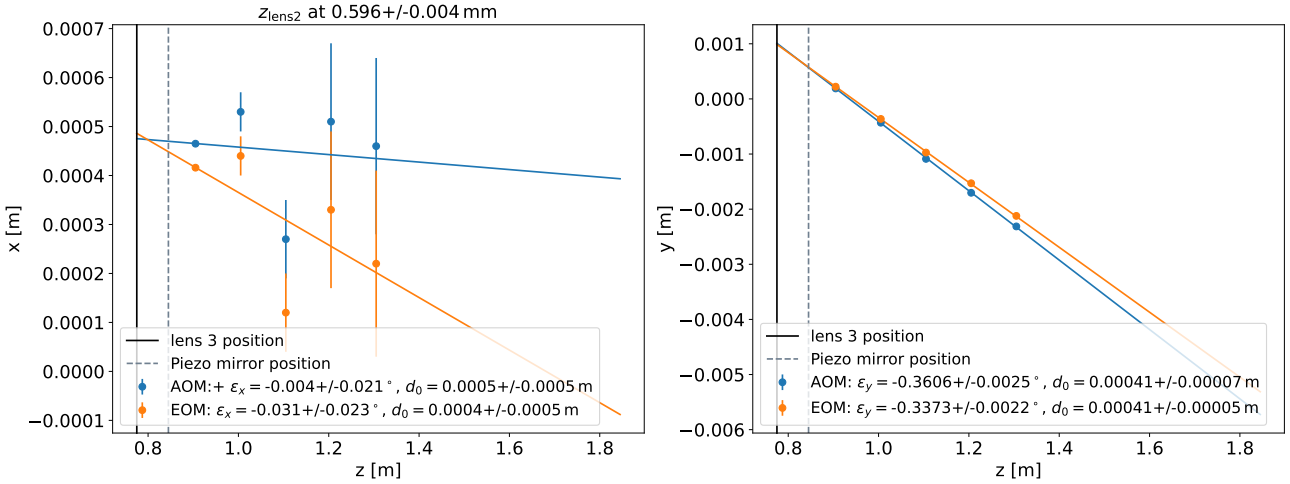

Figure 77: Measured beam trajectories for the phase measurements in Section 5.3.2.

Bibliography

[1] P. Manjuleshwar, C. Yogesh. *Unveiling The Mysteries Of The Cosmos: An Overview Of Radio Astronomy And Its Profound Insights*. 2023. arXiv: 2308.09415 [astro-ph.GA].

[2] C. Li, B. Ma. "LHAASO discovery of highest-energy photons towards new physics". In: *Science Bulletin* 66.22 (Nov. 2021), pp. 2254–2256. ISSN: 2095-9273. DOI: 10.1016/j.scib.2021.07.030.

[3] A. Neronov. "Introduction to multi-messenger astronomy". In: *Journal of Physics: Conference Series* 1263.1 (June 2019), p. 012001. ISSN: 1742-6596. DOI: 10.1088/1742-6596/1263/1/012001.

[4] S. Ray et al. *Gravitational wave: generation and detection techniques*. 2023. arXiv: 2312.17291 [gr-qc].

[5] B. P. Abbott et al. "Observation of Gravitational Waves from a Binary Black Hole Merger". In: *Phys. Rev. Lett.* 116 (6 Feb. 2016), p. 061102. DOI: 10.1103/PhysRevLett.116.061102.

[6] M. Maggiore et al. "Science case for the Einstein telescope". In: *Journal of Cosmology and Astroparticle Physics* 2020.03 (Mar. 2020), pp. 050–050. ISSN: 1475-7516. DOI: 10.1088/1475-7516/2020/03/050.

[7] *Design Report Update 2020 for the Einstein Telescope*. ET-0007C-20. ET Steering Committee Editorial Team, Sept. 2020.

[8] K. Agatsuma et al. "High-performance phase camera as a frequency selective laser wavefront sensor for gravitational wave detectors". In: *Opt. Express* 27.13 (June 2019), pp. 18533–18548. DOI: 10.1364/OE.27.018533.

[9] S. Ronchini et al. "Perspectives for multimessenger astronomy with the next generation of gravitational-wave detectors and high-energy satellites". In: *Astronomy & Astrophysics* 665 (Sept. 2022), A97. ISSN: 1432-0746. DOI: 10.1051/0004-6361/202243705.

[10] O. J. Piccinni. "Status and Perspectives of Continuous Gravitational Wave Searches". In: *Galaxies* 10.3 (2022). ISSN: 2075-4434. DOI: 10.3390/galaxies10030072.

[11] A. Masaki et al. "Analysis for burst gravitational waves with TAMA300 data". In: *Classical and Quantum Gravity* 21.5 (Feb. 2004), S735. DOI: 10.1088/0264-9381/21/5/051.

[12] M. Branchesi et al. "Science with the Einstein Telescope: a comparison of different designs". In: *Journal of Cosmology and Astroparticle Physics* 2023.07 (July 2023), p. 068. ISSN: 1475-7516. DOI: 10.1088/1475-7516/2023/07/068.

[13] M. Pitkin et al. "Gravitational Wave Detection by Interferometry (Ground and Space)". In: *Living Reviews in Relativity* 14.1 (July 2011). ISSN: 1433-8351. DOI: 10.12942/lrr-2011-5.

[14] B. S. Sathyaprakash et al. *Cosmology and the Early Universe*. 2019. arXiv: 1903.09260 [astro-ph.HE].

[15] A. Sider et al. *E-TEST prototype design report*. Dec. 2022. DOI: 10.48550/arXiv.2212.10083.

[16] T. Zhang, S. Danilishin. "Conceptual Design and Noise Budget of Einstein Telescope". In: *Proceedings of the XIII Einstein Telescope Symposium*. Einstein Telescope Collaboration. 2023.

[17] J. Pitman, M. Yor. *A guide to Brownian motion and related stochastic processes*. 2018. arXiv: 1802.09679 [math.PR].

[18] R. Paschotta. *Thermal Lensing*. RP Photonics Encyclopedia. DOI: 10.61835/v71. (Visited on 10/09/2024).

[19] *Detektor für Gravitationswellen*. Schlussbericht. Verbund: (Gravitationswellen-Teleskop der dritten Generation). Friedrich-Alexander-Universität Erlangen-Nürnberg.

[20] R. Paschotta. *Optical Heterodyne Detection*. RP Photonics Encyclopedia. DOI: 10.61835/79k. (Visited on 10/09/2024).

[21] R. Paschotta. *Acousto-optic Modulators*. RP Photonics Encyclopedia. DOI: 10.61835/az1. (Visited on 10/09/2024).

[22] R. Paschotta. *Acousto-optic Frequency Shifters*. RP Photonics Encyclopedia. DOI: 10.61835/j5u. (Visited on 10/09/2024).

[23] R. Paschotta. *Electro-optic Modulators*. RP Photonics Encyclopedia. DOI: 10.61835/7rv. (Visited on 10/13/2024).

[24] K. AGATSUMA et al. "Phase camera development for gravitational wave detectors". In: *PoS* TIPP2014 (2015), p. 228. DOI: 10.22323/1.213.0228.

[25] A. Franzen. *ComponentLibrary*. GW Optics. Licensed under Creative Commons Attribution-NonCommercial 3.0 Unported License.
Available online: https://www.gwoptics.org/ComponentLibrary/. (Visited on 10/21/2024).

[26] O. Svelto. *Principles of Lasers*. 5th. New York: Springer, 2010, pp. 153, 154. ISBN: 978-1-4419-1301-2.

[27] A. A. Tovar, L. W. Casperson. "Generalized beam matrices: Gaussian beam propagation in misaligned complex optical systems". In: *J. Opt. Soc. Am. A* 12.7 (July 1995), pp. 1522–1533. DOI: 10.1364/JOSAA.12.001522.

[28] A. A. Tovar, L. W. Casperson. "Generalized beam matrices. III. Application to diffraction analysis". In: *J. Opt. Soc. Am. A* 13.11 (Nov. 1996), pp. 2239–2246. DOI: 10.1364/JOSAA.13.002239.

[29] O. Svelto. *Principles of Lasers*. 5th. New York: Springer, 2010, p. 475. ISBN: 978-1-4419-1301-2.

[30] I. Kardosh. "Beam Properties and Quality Factor of VCSELs". In: 2004. URL: https://api.semanticscholar.org/CorpusID:43413156 (visited on 08/20/2024).

[31] Connet Laser Technology Co.,Ltd. *CoSF-D-ER-B-LP Narrow Linewidth Single Frequency Fiber Laser*. http://en.connet-laser.com/3f102361-c754-f77d-e5bf-0f4747cb1702/8b4a56d2-d576-3397-544c-34260f9bc3ee.shtml. (Visited on 12/19/2023).

[32] R. Paschotta. *Fiber Collimators*. RP Photonics Encyclopedia. DOI: 10.61835/ked. (Visited on 08/20/2024).

[33] Schäfter+Kirchhoff GmbH. *Collimated beam diameter of a singlemode fiber*. https://www.sukhamburg.com/support/technotes/fiberoptics/coupling/collimatingsm/diameter.html. (Visited on 09/11/2024).

[34] Thorlabs. *Does NA provide a good estimate of beam divergence from a single mode fiber?* https://www.thorlabs.com/newgrouppage9.cfm?objectgroup_id=14204. (Visited on 09/11/2024).

[35] S. Kim, M. Kim. "Rotation Representations and Their Conversions". In: *IEEE Access* PP (Jan. 2023), pp. 1–1. DOI: 10.1109/ACCESS.2023.3237864.

[36] "White Paper Principles of lock-in detection and the state of the art Zurich Instruments Release". In: 2016. URL: https://api.semanticscholar.org/CorpusID:202682418.

[37] *1.5um CosF-D Narrow Linewidth Single Frequency Fiber Laser User Manual (V1.2)*. Tech. rep. 3/F, Building 322 No. 953 Jianchuan Road, Minhang, Shanghai: Connet Laser Technology Co.Ltd.

[38] *Test Report*. Tech. rep. 3/F, Building 322 No. 953 Jianchuan Road, Minhang, Shanghai: Connet Laser Technology Co.Ltd, Apr. 2023.

[39] Thorlabs. *Polarization-Maintaining FC/APC Fiber Optic Patch Cables*. https://www.thorlabs.com/newgrouppage9.cfm?objectgroup_id=3345&pn=P3-1550PM-FC-1. (Visited on 09/11/2024).

[40] Newport Corporation. *IR Free-Space Isolators (1110 - 2100 nm)*. https://www.thorlabs.com/newgrouppage9.cfm?objectgroup_id=4916&pn=IO-4-1550-VLP. (Visited on 10/21/2024).

[41] *IO-4-1550-VLP Free-Space Isolator User Guide*. Tech. rep. Thorlabs, Sept. 2018.

[42] *WinCamD User Manual*. Tech. rep. 31 Upper Ragsdale Drive, Suite 1 Monterey, CA 93940: DataRay Inc.

[43] Thorlabs. *Triplet Fiber Optic Collimators/Couplers*. https://www.thorlabs.com/newgrouppage9.cfm?objectgroup_id=5124&pn=TC12APC-1550. (Visited on 10/21/2024).

[44] Thorlabs. *N-BK7 Plano-Convex Lenses (AR Coating: 1050 - 1700 nm)*. https://www.thorlabs.com/newgrouppage9.cfm?objectgroup_id=3281&pn=LA1908-C. (Visited on 01/09/2024).

[45] Thorlabs. *UV Fused Silica Broadband Plate Beamsplitters (Coating: 600 - 1700 nm)*. https://www.thorlabs.com/newgrouppage9.cfm?objectgroup_id=6044&pn=BSW29. (Visited on 08/13/2024).

[46] R. Paschotta. *Mode Matching*. RP Photonics Encyclopedia. DOI: 10.61835/x1d. (Visited on 08/19/2024).

[47] Thorlabs. *N-BK7 and N-SF11 Bi-Concave Lenses, AR Coating 1050 - 1700 nm*. https://www.thorlabs.com/newgrouppage9.cfm?objectgroup_id=9735&pn=LD1464-C. (Visited on 10/21/2024).

[48] Thorlabs. *N-BK7 Bi-Convex Lenses (AR Coating: 1050 - 1700 nm)*. https://www.thorlabs.com/newgrouppage9.cfm?objectgroup_id=4850&pn=LB1676-C. (Visited on 10/21/2024).

[49] Newport Corporation. *Plano-Convex Lens, N-BK7, 25.4 mm Diameter, 600 mm EFL, 1000-1550 nm*. https://www.newport.com/p/KPX119AR.18. (Visited on 08/19/2024).

[50] Thorlabs. *Fused Silica Broadband Dielectric Mirrors*. https://www.thorlabs.com/newgrouppage9.cfm?objectgroup_id=139&pn=BB1-E04. (Visited on 10/21/2024).

Acknowledgements

First I want to thank Prof. Dr. Stefan Funk for providing me with this interesting topic where my interest in laser physics could be combined with gravitational waves.

I want to thank my supervisor Benjamin Schwab for taking his time to guide me throughout this work and proofreading my thesis multiple times.

Thanks to Johannes Schäfer for always being helpful an for alwys being a source of cheerfulness at the coffee break.

Thanks to my girlfriend Hetali Tambe for always emotionally supporting me.

Thanks to Phillip Laub for being a good office mate until his MA was finished.

Thanks to the democratically elected leader of The Democratic People's Republic of the East Astro Office Caroline Collischon for having a stash of drinks in the office that I could access when working late hours.

Also thanks to everybody that regularly attended the coffee break and/or took part in table tennis.

Thanks to Karen Terveer for DOG.

Thanks to Ria for being DOG.

Special thanks to Mario Engelmann for always reminding me that the One Piece is real.

And thanks to every other person from the at ECAP in general for providing a nice work environment.

Eigenständigkeitserklärung

Hiermit versichere ich, Timo Neeser (22281431), die vorgelegte Arbeit selbstständig und ohne unzulässige Hilfe Dritter sowie ohne die Hinzuziehung nicht offengelegter und insbesondere nicht zugelassener Hilfsmittel angefertigt zu haben. Die Arbeit hat in gleicher oder ähnlicher Form noch keiner anderen Prüfungsbehörde vorgelegen und wurde auch von keiner anderen Prüfungsbehörde bereits als Teil einer Prufung angenommen.

Die Stellen der Arbeit, die anderen Quellen im Wortlaut oder dem Sinn nach entnommen wurden, sind durch Angaben der Herkunft kenntlich gemacht. Dies gilt auch für Zeichnungen, Skizzen, bildliche Darstellungen sowie für Quellen aus dem Internet.

Mir ist insbesondere bewusst, dass die Nutzung kunstlicher Intelligenz verboten ist, sofern diese nicht ausdrucklich als Hilfsmittel von dem Prüfungsleiter bzw. der Prüfungsleiterin zugelassen wurde. Dies gilt insbesondere für Chatbots (insbesondere ChatGPT) bzw. allgemein solche Programme, die anstelle meiner Person die Aufgabenstellung der Prüfung bzw. Teile derselben bearbeiten könnten.

Ort, Datum	Unterschrift